Università degli Studi di Padova
Dipartimento di Biologia
Corso di Laurea Magistrale in Biotecnologie Industriali

Microalgae-mediated biogenic synthesis of metallic silver and zinc oxide particles and their functionalization with poly(2-methyl-2-oxazoline)

Relatore: Prof. Silvia Gross
Dipartimento di Scienze Chimiche (DiSC)

Correlatore: Prof. Edmondo Maria Benetti
Dipartimento di Scienze Chimiche (DiSC)

Controrelatore: Prof. Sabrina Antonello
Dipartimento di Scienze Chimiche (DiSC)

Laureando: Nadir Vincenzo Guir

Anno Accademico 2022/2023

“I don’t stop when I’m tired. I stop when I’m done”
-David Goggins

“Through hard work, perseverance and faith in God,
you can live your dreams”
-Ben Carson

INDEX

LIST OF ACRONYMS

ACN = Acetonitrile

Ag = Silver

AgNPs or Ag^0NPs = metallic silver nanoparticles

Ar = Argon

ATR = Attenuated Total Reflectance

AuNPs or Au^0NPs = metallic gold nanoparticles

COMU = (1-Cyano-2-ethoxy-2-Oxoethylidenaminooxy)dimethylamino-Morpholino-carbenium hexafluorophosphate

CROP = Cationic Ring Opening Polymerisation

DCC = N,N′-DiCyclohexylCarbodiimide

DCU = N,N-DiCyclohexylUrea

DIPEA = N,N-DiIsoPropylEthylAmine

DLS = Dynamic Light Scattering

DMF = N,N-Dimethylformamide

DOPA = L-3,4-DihydrOxyPhenylAlanine

DP = Degree of Polymerisation

EPA = EicosaPentaenoic Acid

ESI-MS = ElectroSpray Ionisation-Mass Spectrometry

FCC = Face-Centered Cubic

FDA = Food and Drug Administration

FWHM = Full Width at Half Maximum

GPC = Gel Permeation Chromatography

GRAS = Generally Recognised As Safe

HBTU = N,N,N′,N′-Tetramethyl-O-(1H-benzotriazol-1-yl)uronium hexafluorophosphate

HPLC-MS = High Performance Liquid Chromatography-Mass Spectrometry

IR = Infra Red

IR-ATR = Attenuated Total Reflectance Infrared Spectroscopy

LSPR = Localised Surface Plasmon Resonance

Mfps = Mussel Foot ProteinS

MOXA = 2-methyl-2-oxazoline

MS = Mass Spectrometry

NADH = Nicotinamide Adenine Dinucleotide

NADPH = Nicotinamide Adenine Dinucleotide Phosphate

ND = NitroDopamine

NHS = N-HydroxySucinimide

NMR = Nuclear Magnetic Resonance

NPs = NanoParticles

Oxyma = ethyl 2-hydrOXimMno-2-cyanoAcetate

PDI = PolyDispersity Index

PEG = Poly(Ethylene Glycol))

PMOXA = Poly(2-methyl-2-oxazoline)

PMOXA@Ag = PMOXA covered silver particle

PMOXA@ZnO = PMOXA covered zinc oxide particle

PMOXA-100-COOEt = Poly(2-methyl-2-oxazoline) with 100 repeating units terminated with an ethyl group

PMOXA-100-COOH = Poly(2-methyl-2-oxazoline) with 100 repeating units terminated with a carboxyl group

PMOXA-100-ND = Poly(2-methyl-2-oxazoline) with 100 repeating units terminated with the nitrodopamine group

PMOXA-100-NH_2 = Poly(2-methyl-2-oxazoline) with 100 repeating units terminated with an aminic group

PMOXA-100-S-S = Poly(2-methyl-2-oxazoline) with 100 repeating units terminating with a disulphide group

PMOXA-50-COOEt = Poly(2-methyl-2-oxazoline) with 50 repeating units terminated with an ethyl group

PMOXA-50-COOH = Poly(2-methyl-2-oxazoline) with 50 repeating units terminated with a carboxyl group

PMOXA-50-ND = Poly(2-methyl-2-oxazoline) with 100 repeating units terminated with the nitrodopamine group

PMOXA-NHS = Poly(2-methyl-2-oxazoline) with a N-HydroxySucinimide terminating group

POx = PolyOxazolines

QD = Quantum Dots

ROS = Reactive Oxygen Species

RT = Room Temperature

SAM = Self Assembled Monolayer

SEM = Scanning Electron Microscopy

TEA = TriEthylAmine

TEM = Transmission Electron Microscopy

TENOH = TetraEthylammonium hydroxide

TGA = ThermoGravimetric Analysis

UV-Vis light = Ultra Violet – Visible light

XAS = X-ray Absorption Spectroscopy

XRD = X-Ray Diffraction

Zn = Zinc

ZnO = Zinc Oxide

ABSTRACT

The objective of this thesis is to obtain stable suspensions, of biogenically synthetised zinc oxide (ZnO) and metallic silver (Ag) particles, through functionalisation with polyoxazolines ligands

Both ZnO and Ag nanoparticles have interesting technological properties, especially in the field of biomedicine. Colloidal silver, displaying antimicrobial properties, has been used to prevent infection and to treat wounds and doped zinc oxide particles can be used as a probe in optical bioimaging.

The biogenic route is a sustainable and cost-effective synthesis method, which exploits a biological agent. In this work, the microalga *Nannochloropsis gaditana* was used. Additionally, classical wet chemistry approaches (including hydrothermal route) were also used and considered as benchmarks.

To sterically stabilise the obtained nanoparticles, poly(2-alkyl-2-oxazoline)s (PMOXAs) were used as ligands. Polyoxazolines are a class of water-soluble organic polymers enabling a wide range of functionalities. PMOXA was synthetised with a degree of polymerisation (DP) of 50 ad 100, and modified with different anchor groups, to produce suitable and water-soluble ligands for the particles. These procedures were aimed to obtain stable suspensions in water to be used as pharmaceutical formulations.

All the particles were characterised with various analytical techniques (XRD, DLS, UV-Vis Spectroscopy, TEM, SEM, ATR-IR) and the synthesis protocols were optimised. The polymers and their functionalities were characterised as well using multiple techniques (NMR, ESI-MS). Finally, particle functionalisation was confirmed with DLS and ATR-IR and the colloidal stability was monitored through time.

1. INTRODUCTION AND AIM OF THE THESIS

Nowadays, one of the major issues for the current socio-economic system is environmental sustainability.

The classical approach to goods production and industry is considered to follow "a linear model" which can be summarised as "take-make-dispose". This means that raw materials are extracted, transformed into products, and discarded as waste after the usage. In this context, the only priority is to capitalise onto the selling without considering the environmental damage caused neither by disposal nor by manufacturing [1].

A more modern and environmentally friendly paradigm would be the one of "circular economy". In this case, products are designed taking into account their environmental impact and recycling of their components at the end of life [2]. In this context, "Green Chemistry" was conceived in 1998 [3], with the purpose of avoiding the use of hazardous substances during the chemical syntheses and minimising waste production. In particular, this new field of study follows twelve rules elaborated by Paul T. Anastas and John Warner in 1998 [3], some of which state to perform reactions at low temperatures and pressure. Many of these criteria are met by the "wet chemistry" approaches. These methodologies imply the use of a liquid phase for the syntheses, which in turn limits the array of high reaction temperatures due to its boiling point [4].

This thesis is focused on the synthesis of nano and microparticles zinc oxide (ZnO) and metallic silver (Ag^0), drawing technological application in several fields.

The wet chemical approaches for these two systems are quite similar. Both syntheses rely on an aqueous medium, a metal precursor (a zinc or silver salt), heat and a second reagent (NaOH or an organic reducing agent, classically sodium citrate, respectively). In the case of ZnO, the basic environment determined by the presence of NaOH triggers complex equilibria leading to ZnO precipitation [5]. On the other hand, for the Ag nanosystems, the second reagent reduces the Ag^+ cations to their metallic state and also acts as a stabilising ligand for particle formation [6,7].

Moreover, syntheses of zinc oxide were also carried out through a hydrothermal route. This procedure exploits a closed reaction system which enables to reach a pressure above 1 atm and a temperature above water boiling point. This approach, under subcritical conditions, results in dramatic changes regarding solvent characteristics (e.g. viscosity and dielectric constant) determining differences in crystallisation pathway and the reaction products compared to classical batch synthesis (i.e. different morphologies and particle size) [8].

To further enhance sustainability, a promising wet chemical approach is the biogenic synthesis. This relatively recent approach is based on the use of biological extracts both as scaffolds and/or as reducing agents, diminishing the cost and the environmental impact related to the production of reactants themselves [9]. These extracts can be derived from plants, bacteria culture, or any other biological sample containing complex organic molecules. In particular, cultivation of microorganisms can be a promising constant source of "bio-reactant" as it is continuously produced as the culture grows. For that reason, and others discussed later, this work will deal with microalgae. These are unicellular photosynthetic organisms which only need a light source, micronutrients and atmospheric CO_2 to grow in an aqueous medium (also helping to deal with global warming due to the greenhouse effect) [10,11]. These basic growth requirements and outstanding eco-friendly features confer significant advantages over other biological systems, like bacteria or cultured mammalian cell. The biomolecules inside these photosynthetic microorganisms may act as reducing and scaffolding agents for nanoparticle synthesis [12].

Both zinc oxide e metallic silver particles may be used as antimicrobial wound treatment or antiseptic agent for food packaging [13,14] by exploiting several mechanisms, discussed later. Moreover, doped ZnO can be used as optical bioimaging probe [15]. However, in order to be used as such, these systems need to be dispersible in water [16]. Ag nanoparticles made by using the classical wet synthesis (with sodium citrate) remained dispersed in suspension, as expected, being stabilised by citrate. On the other hand, the same cannot be said for zinc oxide which forms a precipitate due to its low solubility in water [17]. Moreover, also Ag nanoparticles, synthetised by the biogenic route, precipitated as well.

For the above discussed reasons, the obtained systems need to be stabilised by some organic soluble ligand in order to remain suspended in water. Polyoxazolines were chosen in this work as organic polymers to stabilise the particles. They are a promising alternative to poly(ethylene glycol) (PEG) as suitable coating agents in pharmaceutical formulations due to their simple modulation in term of functional groups [18,19]. In order to be adsorbed to the inorganic material, the polymers were functionalised alternatively with the disulphide and catechol group, which are demonstrated to tightly bind, respectively, metallic silver and zinc oxide [20,21].

The final aim of this thesis was the production and characterisation of biogenically synthetised Ag and ZnO particles using microalgae and their suspension into water by exploiting organic ligands.

This thesis consists of 8 chapters. In this chapter (#1), the introduction and the aim of the thesis are described. In the following chapter (#2) properties and application of zinc oxide and silver are discussed. In the following chapter (#3), wet chemical synthesis approaches toward the nanoparticles of interest are described. Chapter 4 describes the polymers used as ligands for the inorganic materials. In chapter 5 experimental data are reported and discussed. In chapter 6, the analytical techniques

used to characterise both the polymeric ligands as well as the inorganic nanoparticles are described. In chapter 7, the materials and the methodologies used are reported and explained. In chapter 8, the conclusions drawn from this work and the outlooks for future developments are evaluated. Finally, acknowledgements and the list of bibliographical references are reported.

2. ZINC OXIDE AND SILVER

In this chapter, zinc oxide and silver are described with their properties and applications.

2.1. Chemical-physical and structural properties of nanostructured zinc oxide

ZnO is a low cost compound [22] and it is present in nature in three different crystalline structures: rocksalt, zinc blende and wurtzite (hexagonal lattice), shown in the following **Figure 2.1 I**. The latter polymorph is the most thermodynamically stable and abundant under standard conditions (0 °C, 1 bar [23]). It lacks an inversion centre and has every zinc atom in the centre of a tetrahedron where at the vertices there are 4 oxygen atoms. Moreover, every crystal structure shows semiconductive properties with a wide direct band gap of ~3.3 eV, making the material feasible for optoelectronics applications [24].

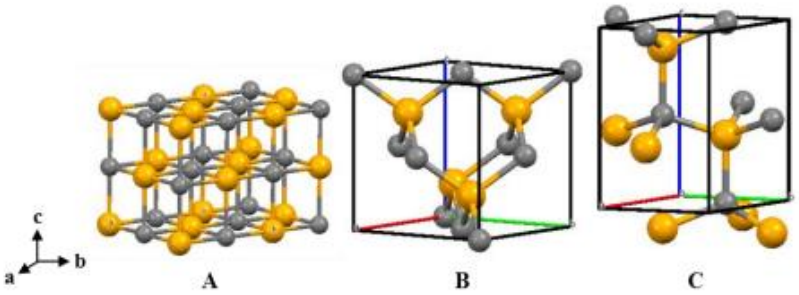

Figure 2.1 I *ZnO polymorphs: a) rocksalt, b) zinc blende, c) wurtzite. Zinc and oxygen are respectively coloured in grey and yellow [25]*

In the case of wurtzite (C in the Figure above), zinc (Zn^{2+}) and oxygen (O^{2-}) atoms are positioned on alternated planes across the structure. This arrangement determines a polarity in the crystal which influences electrostatic attraction, piezoelectric properties and directs epitaxial crystal growth. Even if the hexagonal prism have 6 faces neutrally charged, 2 of them are polarised (respectively the 0001 for zinc (positive charge) and 000-1 for oxygen (negative charge)) [26], as illustrated in the following **Figure 2.1 II**.

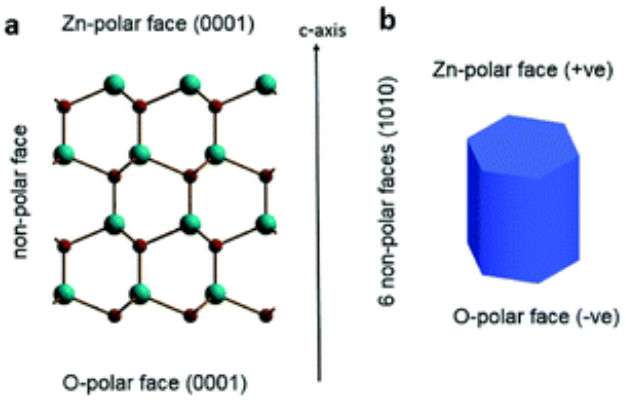

Figure 2.1 II *Wurtzite ZnO crystal from a polarity perspective: a) the faces 0001 and 000-1 are positioned respectively at the top and the bottom of the image, perpendicularly towards the plane of the observer b) the overall crystal is shown highlighting the polar planes on top and at the bottom of the structure* [26]

Nanostructured ZnO can be synthesised in various morphologies and dimensions. Tuning reaction conditions, nanorods [27], nanowires [28], nanospheres [29] and other morphologies were obtained. All these different shapes can be exploited to modulate its optical properties [30].

Zinc oxide appears as a white powder, making it useful for orthodontal applications (also thanks to its inherit resistance to deformation) [31]. However, being a d^{10} metal, its colour is only due to several lattice defects ad not to $d \rightarrow d$ transitions [32–34]. Finally, the compound also turns yellow upon heating [32]. It is one of the five zinc compounds considered as GRAS (Generally Recognised As Safe) material by the american FDA (Food and Drug administration) [24], which means it has negligible toxicity and it is eligible to be classified as food additive [35].

As a semiconductor (class II-VI), it has a band gap that permits light emission after photon absorption. Moreover, the valence band maximum corresponds to the conduction band minimum, hence this feature causes a radiative recombination [36] (with fluorescence emission) without the need of a quantised, lattice, mechanical vibration (a phonon [37]) conferring the status of direct semiconductor to the material [24].

2.2. Chemical-physical and structural properties of nanostructured silver

Silver is another d-block metal, classified as noble metal thanks to its exceptional resistance to corrosion. Used since ancient times to fabricate jewels and coins [38], silver is the metal with the highest thermal and electrical conductivity (followed

by copper) as well as the most malleable and ductile [32,39]. Differently from the ZnO, the only crystalline structure for Ag is a face-centered cubic (FFC) lattice, being an elemental metal [40]. Nonetheless, it was possible to obtain nanometric Ag (as well as Au) with a hexagonal 4H structure [41,42]. In **Figure 2.2 I** the silver crystal structure (FCC) is reported [43] where silver atoms are positioned at the centre of every cube face as well as at every vertex.

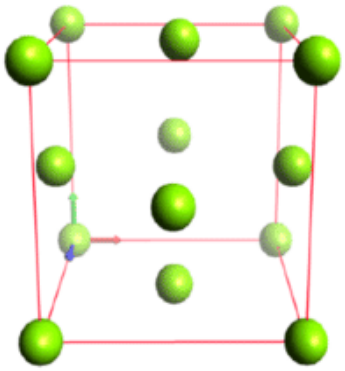

Figure 2.2 I *Silver face-centered unit cell [43]*

Since the silver salts are photosensitive, it is employed in analogical photo-development [34]. Furthermore, from that application, the metal may be also recycled [44]. Even if it may be used as a bulk catalyst for oxidation reaction [45], most of the recent literature is focused on its use as nanostructured compound. Even if it not considered GRAS (like ZnO) nanosized silver is approved by FDA in various products [46]. Whilst, its bulk counterpart shows its peculiar shiny aspect (due to reflectance of visible light rather than the distant 4d→5s transition, which falls in the ultraviolet spectrum [47]), silver nanoparticles appear to be yellow due to plasmon resonance [48]. This feature was already exploited during ancient times since it is reported that Egyptians used colloidal Au as ink. However the best known example of ancient colloidal usage is the Lycurgus Cup [49] shown in **Figure 2.2 II**.

Figure 2.2 II *Lycurgus Cup, drinking Cup, late roman, 4th century, British Museum (London, UK), [49,50]*

The glass cup implemented a dispersion of colloidal silver-gold alloy which appears as green if the light is reflected but becomes red if it is focused. The cause of the red colouring is probably the gold nanoparticles absorption whereas the green is likely caused by both nanoparticles scattering [50,51].

The red colour of gold nanoparticles as well as the yellow of silver NPs, is due to the plasmon resonance. The latter is the collective and coherent oscillation of the conduction band electrons of a metal in response to an electromagnetic wave [52]. The phenomenon is shown in **Figure 2.2 III**.

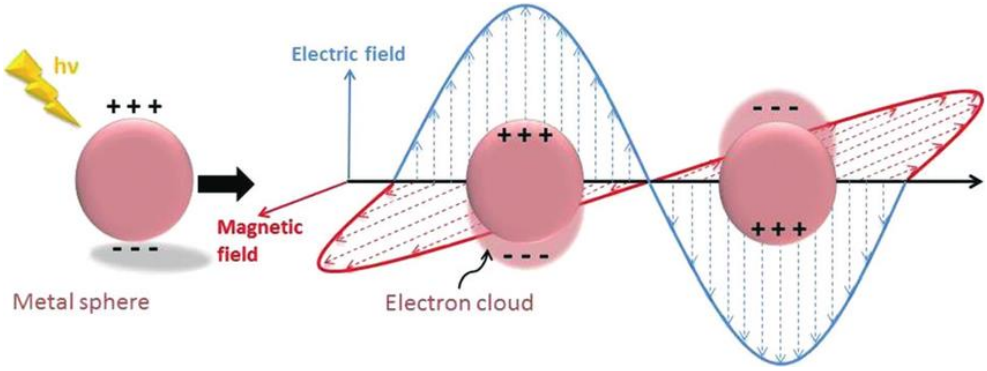

Figure 2.2 III *Localised surface plasmon resonance. In this figure the movement of the electron cloud in response to the electromagnetic impulse is highlighted [53]*

Since noble metal particles are demonstrated to have a plasmon absorption depending on their dimension, the spectra obtained are different. If the incident light on a metal NP, smaller than its wavelength, the phenomenon is called "localised surface plasmon resonance" (LSPR). In this case, conduction electrons are spatially confined (quantum confinement) by the positive nuclei associated to them in the "plasmonic Ag particles". Depending on particle size, this reduction of liberty degree favours the blue shift in absorption spectrum [53,54]. Moreover, bigger particles have a red-shifted spectrum with the contribution of light scattering according to the Mie theory [55].

AgNPs are stable as colloidal dispersion if an appropriate ligand is added to the suspension. Hence, the use of ligands and surfactants adsorbed onto their surfaces is encouraged to prevent coagulation [56]. Furthermore, smaller particles are proven to be more stable compared to their bigger counterparts [57]. Moreover, the surface area to volume ratio is greater for smaller objects, making NPs more reactive and more usable in photocatalysis [53].

The catalytic usage of AgNPs, derive directly from the plasmon absorbance band. This feature, in particular may be tuned not only by changing particle size but also the shape as well as the dispersion media polarity [53,58]. For these reasons, like for ZnO, many different AgNPs shapes were produced in literature (beside classical spheres) such as nanorods [58], nanowires [59], nanocubes [60] and triangular nanoplates [61].

2.3. Applications

Both ZnO and AgNPs have various applications in many fields, such as catalysis, theragnostic, electronics and as sanitising agents [13,15,62–64].

Being a direct semiconductor, ZnO is exploited in photovoltaic cells for its low cost, high conductivity and possibility of band gap tuning through quantum confinement [65]. When the particle size becomes similar to electronic wave function, electrons start experiencing geometrical constraints. As a consequence, electron readjust their energy levels in a way similar to single atoms (rather than a bulk material resulting in a higher separation between the valence and the conduction bands [66]. In **Figure 2.3 I**, a graphical explanation of the concept is provided.

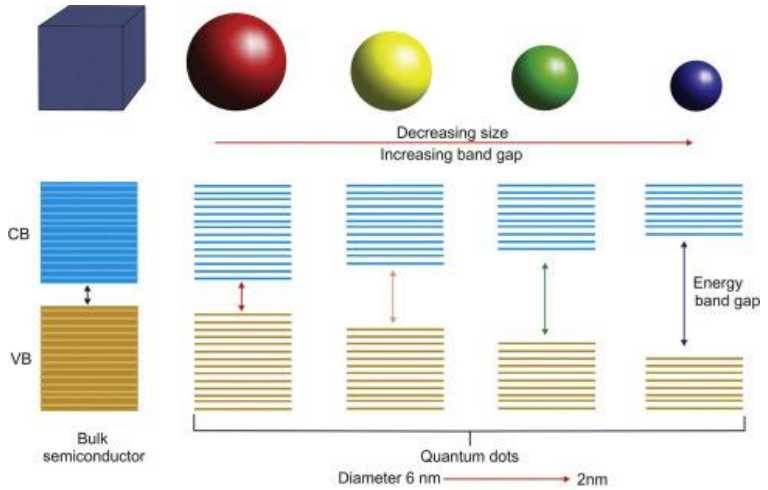

Figure 2.3 I *Quantum confinement effect (in this case applied onto quantum dots nanoparticles). As the object size reduces, the band gap of the semiconductor increases.*

The energy levels-size dependency starts at a diameter near the Bohr radius [66]. In case of bulk ZnO, this value is 2.34 nm, meaning that by producing particles about this size, the band gap can be tuned easily. This feature is desirable in photovoltaic applications since it enables light absorption and the channelling through the electrical circuit [65]. For the same reason, ZnO were are also used in quantum dots-light emitting diodes technology [67].

Beside tuning the band gap of a semiconductor for electronics, the same concept was applied for the LSPR of AgNPs, enhancing the light harvesting properties of solar cells [68]. Moreover, the reduction of nanoparticles size causes a decrease in the superficial to core atom ratio within the particles. Since the external atoms are generally more reactive (not being surrounded by other nuclei of the same element/compound), smaller particles are excellent for catalysis. For this reason, AgNPs are actually studied as photocatalyst [53,69].

Regarding biomedicine, both ZnO and Ag nanoparticles present applications. Semiconductor nanocrystals possess better photoluminescent properties compared to their bulk counterparts (due to the quantum confinement effect) such as wide absorbance and tight emission bands. However, conventional quantum dots (i.e.

CdTe and CdCs) are highly toxic to biological organisms, consequently, they cannot be used as bioimaging probes. Along with its cheap production cost, ZnO is proposed to be a substitute for quantum dots in bioimaging [15]. However, since the band gap of ZnO falls in the UV region, the nanoparticles are frequently doped with other metals. In particular, main group and rare earth elements were reported as enhancing luminescence [15].

Through doping it was possible to obtain ZnO particles suitable for bioimaging, especially with lanthanide ions [70]. The reason behind the ions choice is ascribed to the upconversion luminescence mechanism of these particular elements. It is known that, combining 2 near-infrared photons they can emit one in the blue range of visible light spectrum [71]. Exiting particles in the near-infrared region represent a technological advantage, since for these wavelengths, scattering, absorption, and auto-fluorescence from tissues is greatly reduced allowing to deeper tissue penetration [36]. Combining this property with the band gap of ZnO, as well as its inherit biocompatibility [24], it is possible to obtain new materials which overcome the limitation of both ZnO and lanthanides. Beside doping, ZnO was also used a shell layer in core@shell QD NPs exploiting both the optical properties of conventional QD and the biocompatibility of ZnO [72]. However, considering the tendency of ZnO to precipitate, polymeric ligation is needed to obtain injectable bioimaging probes [73].

On the other hand, Ag nanoparticles are widely used in diagnostic field. Nonetheless, due to the intrinsic lower spectral shift upon aggregation, Ag NPs are mostly overshadowed by Au NPs for colorimetric essays [74]. However, the main application for Ag NPs is disinfection [62,63]. It is very used in both domestic and clinical dentistry being a common antibacterial additive in toothbrushes [75], in clothing [76] and it is also widely used in combination with hyaluronic acid for wound dressing and other therapies [77]. Furthermore, it is effective against antibiotic resistant bacteria [75]. The reason behind this property is still unknown, although several mechanisms were proposed, and they are summarised in **Figure 2.3 III**.

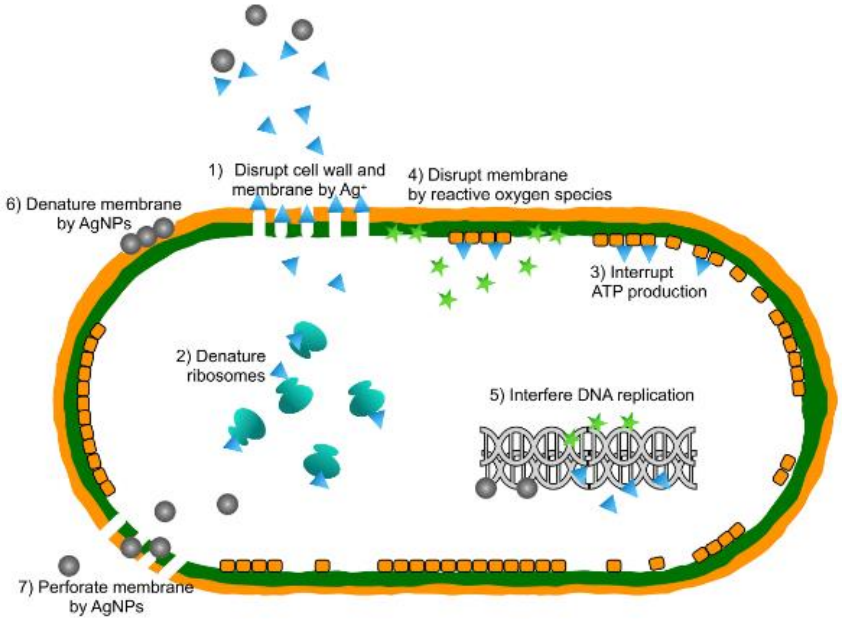

Figure 2.3 III *Proposed antibacterial mechanisms for Ag-NPs [78]*

As it is evinced from the picture, both Ag^+ cations and AgNPs themselves may be responsible for killing bacteria. Metallic silver, through a slow corrosion process, is believed to continuously release to Ag^+ ions proportionately to the surface area, especially for particles smaller than 20 nm [39]. The ions may adhere to the cell wall (thanks to the affinity of sulphur proteins), enhance the permeability and lead to envelope disruption. Moreover, once inside, they may interfere with the ribosomes and cause their denaturation, thereby stopping protein synthesis. Furthermore, Ag^+ ions may interact with the respiratory chain components reducing the ATP supply and generating reactive oxygen species (ROS, such as H_2O_2, O_2^- and $^{\bullet}OH$ [79]) which in turn create DNA and plasmatic membrane damage. Finally, AgNPs may accumulate onto the cell wall, disrupting its structure (thanks to their nanometric size) and perforate it causing the bacterium lysis [78].

Interestingly, even if less used, also ZnO present antimicrobial activity and the mechanism proposed for this feature are similar to those of Ag, being ROS production, Zn^+ release and cell wall integrity alteration from direct ZnO NPs contact [13]. For that reason, ZnO is used as conservating agent in food packaging [24].

3. WET CHEMISTRY SYNTHESIS ROUTES

Nanoparticle production can follow two main routes: physical and chemical processes. The first one comprises the "top-down approach", which consists in the mechanical fragmentation of a bulk material obtaining nano objects, while the second one entails the "bottom-up approach", which exploits chemical species to build nanoparticles from scratch [80]. These approaches are schematically represented in **Figure 3 I**.

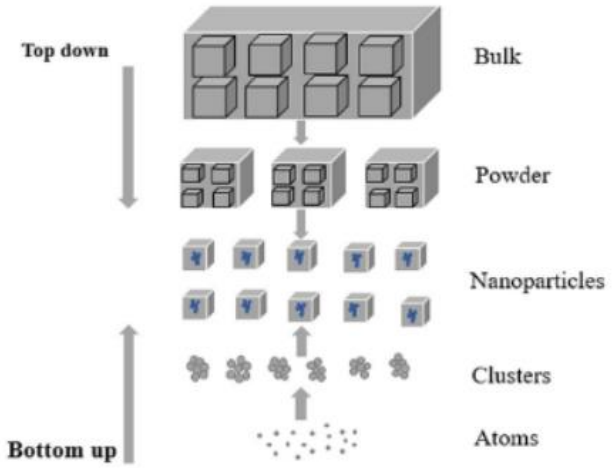

Figure 3 I *Comparison between "Top-down" and "bottom-up" approaches [80]*

The most used physical production technologies are laser ablation, sputtering and ball milling. However, these methods do not ensure a small size distribution of particles and are not feasible for the industrial scale due to the consistent machinery cost [80]. For these reasons, chemical bottom-up approach is still considered the best method for monodisperse nanoparticle production. In this context, wet chemical syntheses are the election methods for metal/metal oxide nanoparticles production. These types of fabrication methods are cheap (not involving particular equipment) and are performed in liquid phase which allows to easily control experimental conditions and thereby particles properties [81,82].

In this thesis, only wet chemistry syntheses were performed and, depending on the material (Ag or ZnO), different methods were exploited.

3.1. Zinc oxide precipitation from solution

This method exploits a zinc salt along with a precipitating agent in water, namely an inorganic base such as NaOH or KOH. In this work, a modified method of the original Bahnemann et al. protocol was exploited [5]. Temperature, reaction time and pH are considered the main variables controlling the precipitation of ZnO NPs. In section **5.1** the theoretical details about the synthesis are discussed whereas in section **7.2.1** the protocol used is reported. As explained in detail in section **5.2**,

syntheses of metal particles from solution can be rationalised with the La Mer-Sugimoto growth model. This implies that once reached supersaturation, the particle formation begins [83,84]. In order to have more variability in terms of shape and size, the use of lesser soluble precursors or different reaction conditions may be needed. For these reasons, the hydrothermal synthesis was also a technique exploited in this work.

3.1.1. Hydrothermal synthesis

The hydrothermal synthesis is a process that takes place in water at a temperature above the boiling point in a sealed vessel. The autogenous pressure within the vessel is above the atmospheric one [85], so, the combination of temperature and pressure causes a change in the water properties. In particular, the viscosity, ionic product, density and dielectric constant change as function of temperature and pressure. In the following **Figure 3.1.1 I**, graphs describing the variation of water properties as function of these two variables, during hydrothermal processes, are reported.

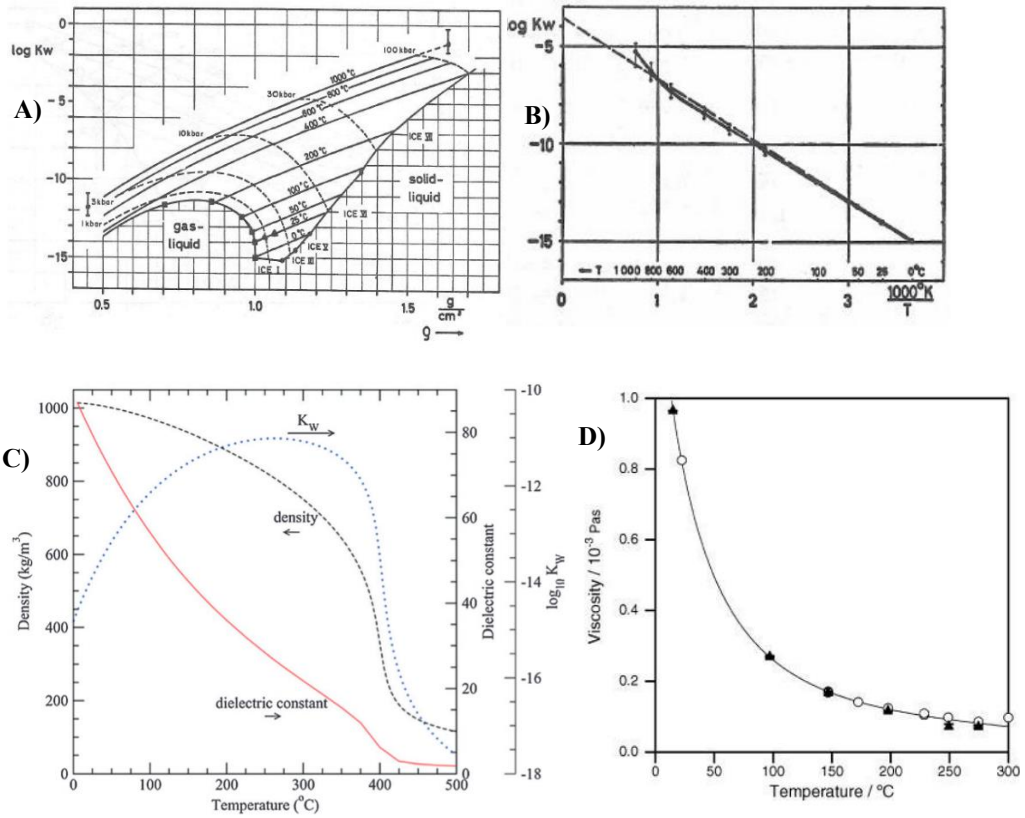

Figure 3.1.1 I *Water properties dependency as function of pressure and temperature. In particular: A) ionic product as function of pressure, B) ionic product as function of temperature, C) dielectric constant as function of temperature (at 30 Mpa) D) viscosity as function of temperature [85–88]*

As can be highlighted from the graphs, ionic product increases both with the increase of pressure and temperature. On the other hand, the dielectric constant decreases if temperature rises, like viscosity. At the critical point, the densities of the two phases become equivalent, and the distinction between the liquid and gas

phases ceases to exist. Beyond the critical point, which occurs at a temperature of 374°C and a pressure of 218 atm, only a supercritical fluid state exists (see water phase diagram in **Figure 3.1.1 II**).

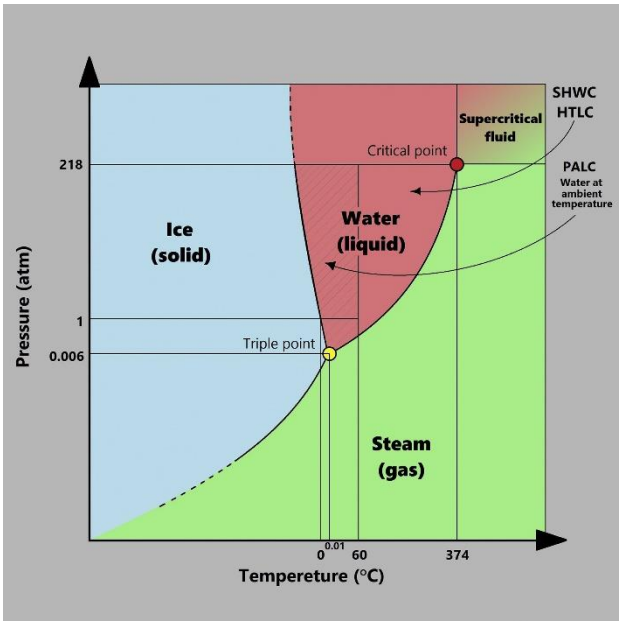

Figure 3.1.1 II *Water phase diagram [89]*

As depicted in **Figure 3.1.1 III**, hydrothermal syntheses are carried out in a closed Teflon® liner, locked in a stainless steel vessel. The autogenous pressure strongly depends on the filling ratio of the liner. As it is shown in the following picture, even small increases in this value can easily result in big variation of pression (at a certain temperature).

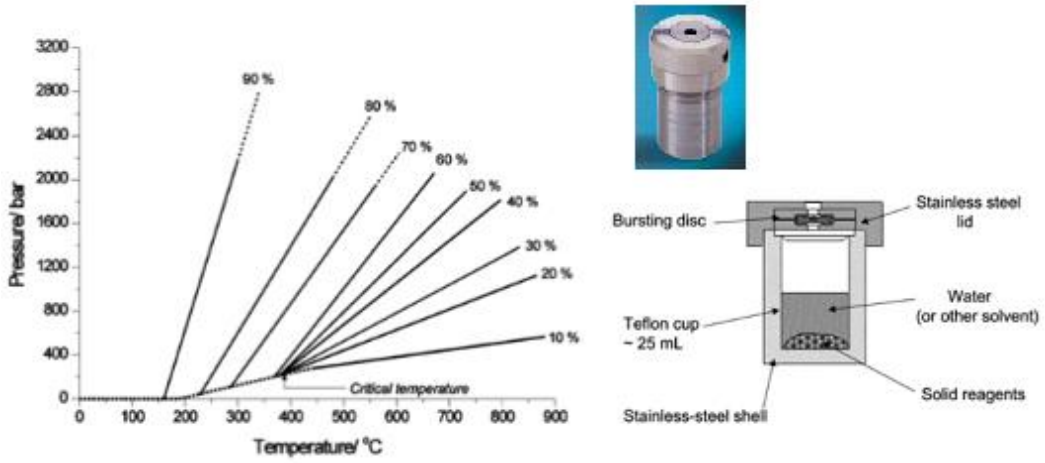

Figure 3.1.1 III *Pressure–temperature dependence of water for different degrees of percentage filling ratio (left) alongside a picture and a schematic representation of an hydrothermal vessel (right) [85]*

Regardless, in most hydrothermal syntheses, temperature and pressure are kept below the critical point. These syntheses are carried out under mild conditions, also known as sub-critical, where the greater reactivity and solubility of precursors are

exploited without reaching the supercritical state. Since conventional hydrothermal synthesis are not performed in stirring conditions, the most probable mechanism for nucleation and growth is the dissolution-reprecipitation process. This mechanism involves the dissolution of precursors, their diffusion and the precipitation of the desired compound [85].

3.2. Turkevich method for colloidal silver synthesis

AgNPs are mostly prepared with three possible methods: pulsed laser ablation in liquid medium, electrochemical synthesis and chemical reduction. However, the last method remains the most cost effective and used [49]. For this reason, it was the one chosen to be used in this thesis. In particular the Turkevich method is the one most used [6,7,90,91]. In particular this protocol is designed for Au NPs, however, it was adapted for Ag NPs as well.

The synthesis exploits a soluble Ag salt (namely, $AgNO_3$) and a reducing agent (such as citrate). The second component reduces the Ag^+ cations to their metallic form, while remaining adsorbed on the nanoparticles preventing aggregation (by displaying the negative charges for citrate, thanks to its carboxylic moieties). This method can be applied also to other metallic NPs (such as titanium and platinum) using the appropriate precursor, as reported in **Figure 3.2 I**.

Figure 3.2 I *Sol dispersion of metal nanoparticles. From left to right: silver, titanium, platinum and gold nanoparticles [49]*

The mechanism behind the nanoparticles formation can be described following the La Mer-Sugimoto model [83,84]. Besides being considerate as highly reproducible, the synthesis product is easily affected by small experimental setting changes [92]. The discussion about this topic is dealt in section **5.2**.

3.3. Biogenic synthesis

The biogenic synthesis was the major focus exploited in this thesis. For both metal and metal oxide particles (as well as for other inorganic particles) the synthesis exploits a biological agent (alive or not) such as fungi, microalgae, bacteria or plant leaves to shape and produce the desired materials [9].

This type of synthesis was born to answer the needs of cheap nanoparticles production and the use of green approaches [3,63]. The mechanisms behind biogenic synthesis are still not clear (for both binary and single metal particles), however it was shown that it is possible both in intracellular and extracellular settings [93]. Using enzymes, plant extracts and living beings, the identification of involved biomolecules is a challenging task. Nonetheless, flavoproteins, NAPDH, nitrate reductases, as well as flavonoids and polysaccharides, are proposed to be part of the reduction mechanisms [94–98]. Regarding metal oxides, however, the same cellular components are proposed to be involved, even if the presence of a reductive reaction step is debatable [94,99,100]. An example of biogenic synthesis is shown in the following **Figure 3.3 I**.

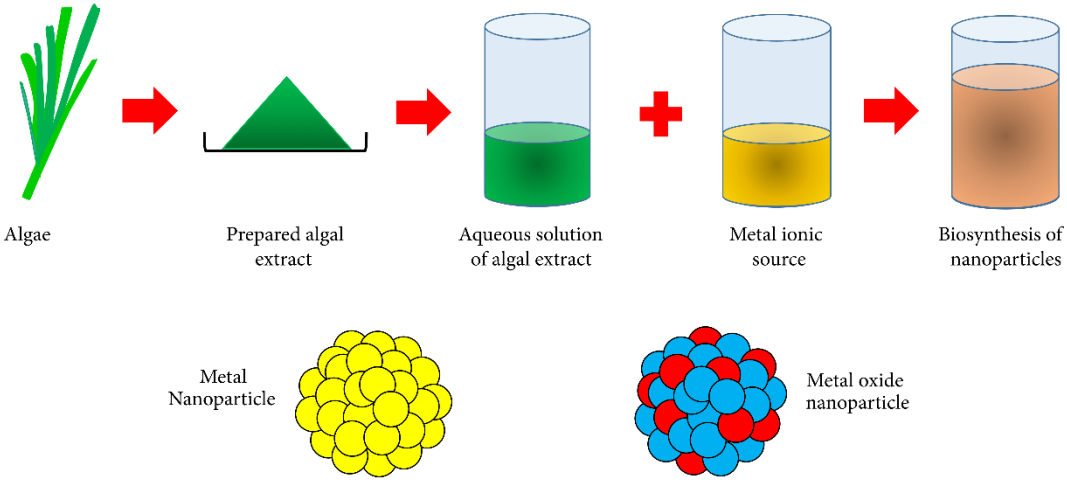

Figure 3.3 I *General synthetic protocol for biogenic synthesis of metal and metal oxide nanoparticles [101]*

As can be seen, the main method for biogenic nanoparticle obtainment is the production of an extract by boiling the biomass (of algae, bacteria, fungi etc), filter and mix it with the desired metal precursor [102].

Considering the wide array of potential biogenic agent (biochar comprised [103]) the choice of biogenic agent for this thesis was dictated by ecological reasons. In particular, the microalga *Nannochloropsis gaditana* was selected.

3.3.1. Nannochloropsis gaditana

Even if the term “microalga” was previously referred to a small taxonomic group with restricted phenotypical properties, nowadays it is commercially used for all the unicellular photosynthetic organisms (both procaryotes and eukaryotes) [10]. The big advantages in using microalgae over of fungi or other microorganisms are their minimalistic growth requirements (only micronutrients, being autotrophic), the relief of the greenhouse effect thanks to CO_2 sequestration and O_2 production (through photosynthesis) and the possibility of obtainment from other established industrial processes (like waste water management), virtually eliminating the cultivation costs [10,11,104–106].

Even if the chosen microorganism was not already proven to be able to produce nanoparticles, this microalga was selected for its simplicity as organism (in view of future systematic studies about the biomolecules involved in the synthesis). In particular, *Nannochloropsis gaditana* is an eukaryotic microalga of *Eustigmatophyceae* class [107]. The overall genus of *Nannocloropsis* comprises marine non-motile spherical microalgae with a diameter between 2 and 3 μm [108]. Despite its small size, most of the cell volume is occupied by a four-wall chloroplast originated from a second endosymbiotic event, in which the eukaryotic microalga engulfed another unicellular photosynthetic organism (a red alga) [109]. Interestingly, the photosynthetic system of *N. gaditana* lacks of accessory chlorophylls containing only the chlorophyll A, even if carotenoids and other pigments are present [110]. Finally, the study of this organism had a revival in recent year due to its rapid growth, nutritional features (being a source of eicosapentaenoic acid, EPA (20:5ω3)) and the possibility of producing biofuels exploiting its high concentration in triglycerides [111–113]. In the following **Figure 3.3.1 I**, a micrograph of *Nannochloropsis gatidata* obtained through optical microscopy is shown.

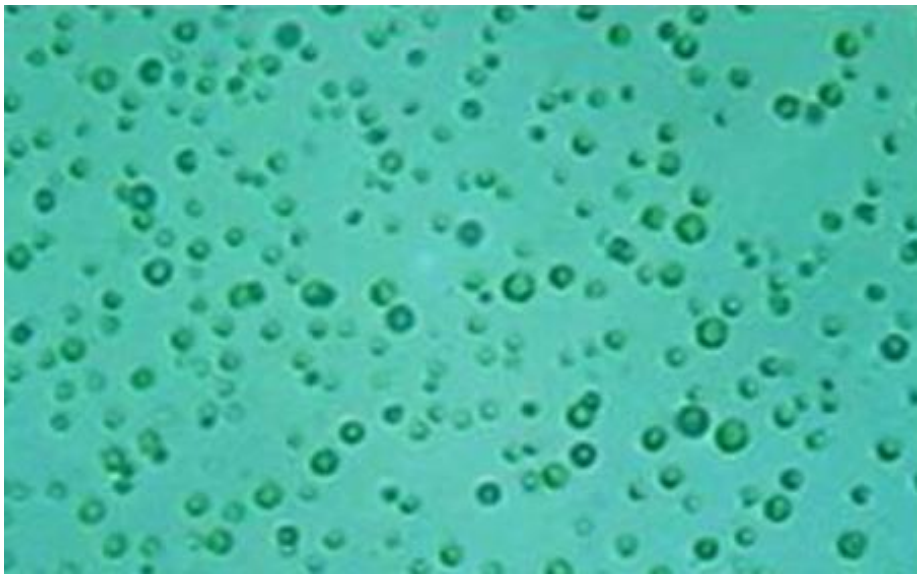

Figure 3.3.1 I *Optical microscopy of Nannochloropsis gaditana [113]*

4. PARTICLE FUNCTIONALISATION

Once obtained the desired NPs, colloidal stabilisation with ligands is needed to obtain stable formulations. However, the ligand choice is crucial as it may be not soluble in water or trigger inflammatory responses.

The use of PEG to obtain stealth NPs is so widely diffused that it was termed the name "PEGilation" to describe it [114,115]. For many years it was considered the only possible polymer for nanosystems in biomedicine. Among the possible alternatives, poly(2-alkyl-2-oxazoline)s (PAOXAs) have recently emerged, due to their stability towards oxidative degradation, biocompatibility and chemical versatility [18]. In **Figure 4 I**, the general structure formula of PAOXA is shown.

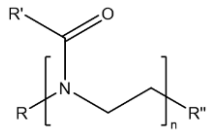

Figure 4 I *General structure of PAOXA, where R represent the initiator moiety, R' the monomer specific side chain and R'' the chain terminator*

These polymers are already used in a variety of biomedical applications, such as for drug delivery and protein coatings [116]. Considering these features, PMOXA was chosen as a polymer ligand for all the particles produced within this thesis. PMOXA is particularly convenient as ligand for the NPs fabricated in this work, as it is highly hydrophilic and can thus stabilize NPs in aqueous medium [116]. In order to anchor robustly the different inorganic NPs the introduction of a specific functional group as chain end is required. In this case of Ag NPs a disulfide anchor was introduced, whereas for ZnO NPs a catechol end group was incorporated in the PMOXA chain. [20,21]. In **Figure 4 II**, the PMOXA modification process performed in this thesis is summarized.

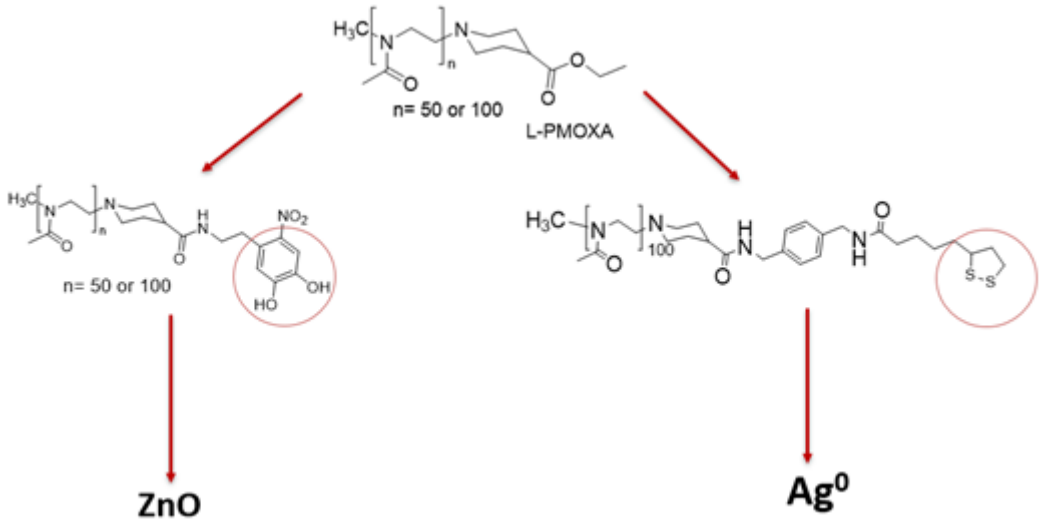

Figure 4 II *Scheme of anchor group polymer links performed in this thesis.*

4.1. Poly(2-methyl-2-oxazoline)

PMOXA is synthesized by cationic ring opening polymerization (CROP) CROP 2-methyl-2-oxazoline (MOXA) [116]. Thanks to the use of chemically tailored initiator and terminator agents CROP enables the accessible modulation of end-groups, allowing one to subsequently introduce anchor moieties [19].

Even if it is considered comparable to PEG, the *in vivo* immune reaction against it is still not completely characterised. However, it is known that, in humans, the innate complement serum system is triggered through the sensing protein C1q [117].

4.2. Catechol group

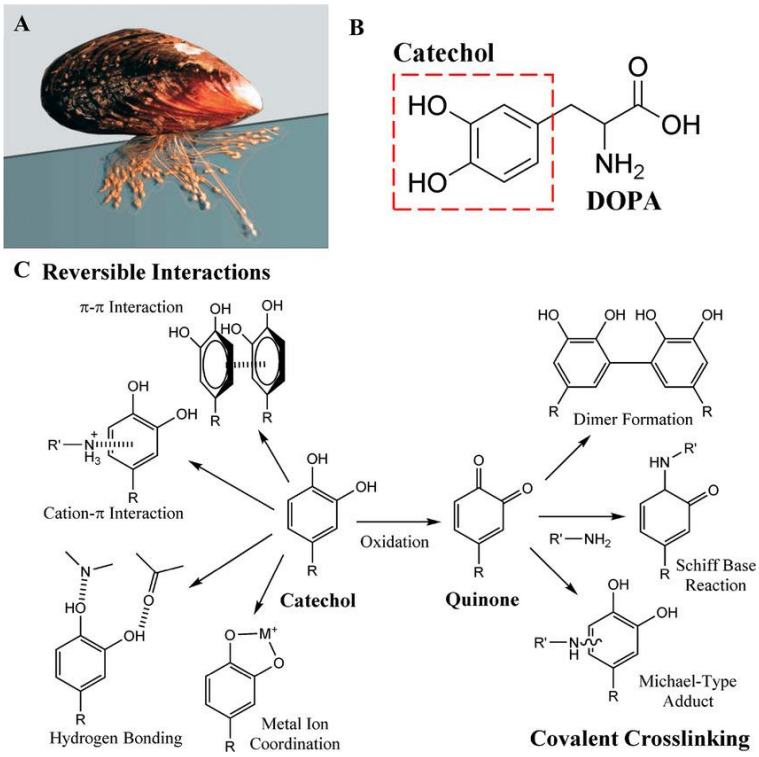

Figure 4.2 I *Catechol group in mussels (Mytilus californianu in the photograph) and its network of modifications to obtain a strong, yet reversible, bond with inorganic surfaces [118]*

The catechol group (shown in **Figure 4.2 I**) is chemically defined as a 1,2-Benzenediol and it is present in mussel foot proteins (Mfps), in the form of the L-DOPA (L-3,4-dihydroxyphenylalanine) amino acid [21,118] (which in mammals is exploited an intermediate precursor for dopamine biosynthesis [119]). In these clams, the moiety is used as anchor group to adhere on inorganic wet surfaces strongly enough to resist sea turbulences. Mussels, however, can attach and detach their tentacles by chemically modifying the DOPA within Mfps. In nature the

switch-off mechanism is due to the oxidation of catechol to quinone, which reduces the adhesion strength, against metal oxides, by 80% (however it is possible to exploit several other modifications for technological purposes) [118]. This last feature left the development of several technological application regarding the obtainment of redox responsive swich devices [118]. Nevertheless, the mechanism exploited for strong adsorption on metal oxide is dependent the deprotonation of the -OH moieties present in the catechol ring. In order to obtain an increase in acidity, and prevent oxidation to quinone, an electron-withdrawing nitro group (-NO_2) was introduced. to the obtained nitro-catechol was previously demonstrated to provide strong and irreversible anchoring with metal oxide surfaces (like ZnO). [118,120,121].

4.3. Disulphide group

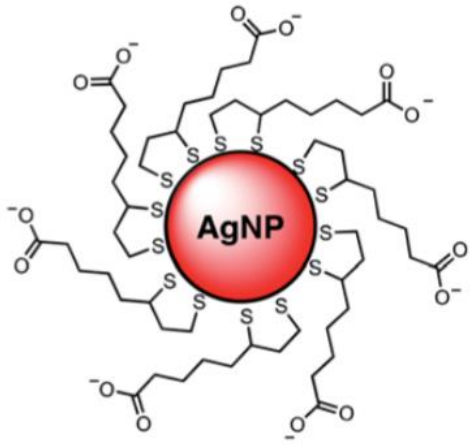

Figure 4.3 I *Representation of a AgNPs covered with lipoic acid molecules trough the disulphide binding [20]*

The sulfhydryl group (-SH, also known as thiol group) is the most renowned moiety used to strongly ligate organic molecules on noble metal surfaces, forming what is known as a the metal-thiolate bond [122]. This functional group is exploited both in the classical Brust-Shiffrin synthesis and for the production of self-assembled monolayers (SAMs) [91,123]. Nevertheless, disulphide group (S-S) is emerging as a better alternative since it is more stable towards oxidation compared to thiols [124].

Most of literature about the topic revolves around the use of the disulphide bearing molecule lipoic acid. The latter is a well-known endogenous molecule widely used in food supplements and medical therapies [125–127]. Even if the use of these kind of ligands is still very new, research work have been made demonstrating the superior affinity [20] and enhanced biocompatibility for AgNPs engulfed in lipoic acid [128]. Nonetheless literature about this specific topic is scarce.

5. RESULTS AND DISCUSSION

In this section, the experimental results obtained in this project are described and discussed. Prior to data illustration, it is dutiful to make a preface dealing with the whole following work. The biogenic synthesis method, for both ZnO and Ag^0 particles, suffers from an intrinsic lack of reproducibility [9].

Microorganisms may differ from clones of their own colony due to environmental factors, even if they underwent the same treatment and belong to the same production lot. In addition, microalgae biomolecular composition heavily depends on cultivating conditions such as lighting [129]. Even though these effects are minimal, as far as this work concerns, it is important to clarify this negative aspect.

For both ZnO and Ag particles, classical golden standard synthesis techniques were also carried out as benchmarks to be referred to. In particular, for ZnO the chosen protocol was the one established by Bahnemann et al. [5], in which an aqueous solution of NaOH and zinc acetate is heated yielding ZnO as a stable suspension eventually leading to a white precipitate. Regarding this project, a molar ratio of 1:1 zinc acetate to sodium hydroxide was used in all batch non-biogenic synthesis. The hydrothermal method was exploited as well, using both the 1:1 zinc acetate to NaOH molar ratio and a more complex protocol by Diodati et al., explained later in the dedicated section (**5.1.1**) [130].

Regarding the non-biogenic synthesis of metallic silver nanoparticles, the Turkevich synthesis method was chosen [90]. This method was firstly deigned for gold nanoparticle but, like the Brust-Shiffrin synthesis, is widely used also for silver and it is considered the standard technique [91,131]. In this project, a molar ratio of 1:3.4 $AgNO_3$ to sodium citrate dihydrate was chosen in order to obtain small and stable colloidal dispersions. Moreover, with the intention of obtaining smaller and less polydisperse NPs, a variant of the method was also explored, hereby called *"Reverse"* synthesis, in which the reagents introduction order was reversed. In addition, the latter procedure better simulates the biogenic ones, being also a closer comparison since the introduction order of reagents is the same.

This chapter describes and discuss the experimental results and their critical discussion. In particular, in the 5.1 section, the syntheses of ZnO are illustrated including non-biogenic (**5.1.1**) and biogenic (**5.1.2**) syntheses. Instead, in subchapter **5.2**, the results coming from metallic silver nanoparticles productions are explored. In details, this section comprises syntheses by the Turkevich method (**5.2.1**) and the biogenic ones (**5.2.2**).

5.1. Zinc oxide particle synthesis

As stated before, this project aims to obtain stable water suspensions of biogenically synthetised ZnO particles, through the support of water-soluble polymeric ligands. Going in details, the protocol for the biogenic syntheses of the material is based on a previous work, made by another research group member (Tinello, S. 2022) as her Master's Degree Thesis [132]. Though it is worth mentioning that the reaction mechanism governing these syntheses is still unclear.

Differently from other biogenic syntheses (like Ag^0 NPs), the oxidation status of Zn remains the same from the precursor salt to the final product, being +2 in both compounds. This means that the metal salt is not reduced by biomolecules, which instead may have only a scaffolding role. In the literature reductive enzymes are proposed to be part of the formation mechanism, thanks to the aim of other organic compounds such as nicotinamide adenine dinucleotide (NADH) and nicotinamide adenine dinucleotide phosphate (NADPH) [94,99,100] in a reduction-oxidation fashion with molecular oxygen O_2.

Even if there are some hypotheses in literature, the main issue behind this lack of knowledge is to be charged to the difficulty in identifying the involved biomolecules. The understanding of mechanistic phenomena and systematic definition of biological components in microalgae (having a role in these situations) are the main question marks remaining to be addressed. Studies involving XAS (X-ray Absorption Spectroscopy), HPLC-MS (High Performance Liquid Chromatography-Mass Spectrometry) and other similar analyses need to be extensively performed in the future, for the sake of understanding such cheap and environmentally sustainable synthesis method.

Both the biogenic and the classical wet chemical approaches are based on the equilibrium between $Zn(OH)_2$ and ZnO. Conventionally, a precursor is provided as a metal salt (Zn^{2+}), and thanks to a basic pH, $Zn(OH)_2$ is eventually formed. The latter, in turn, decomposes generating H_2O and ZnO (precipitate). This mechanism was extensively studied by Bahnemann et al. who investigated the nucleation process using zinc acetate as a precursor (like in this work) [5]. The precipitation of ZnO is also due to the low solubility of $Zn(OH)_2$ ($K_{sp} = 3.5 \cdot 10^{-17}$) [133,134] which pushes the reaction towards the formation of crystalline ZnO [135]. Moreover, high temperature is needed to establish the dehydration reaction [136]. Alkaline pH is demonstrated to be a key factor in the production of zinc oxide, that is why many synthetic protocols include NaOH (or other metal hydroxides like KOH [137]) as precipitating agent. This applies also to hydrothermal methods [138] and for the non-biogenic synthesis carried out in this work. On the other hand, acidic pH determines the dissolution of ZnO, stabilising the Zn^{2+} cation [139]. Finally, higher temperature favours the synthesis overall [132,140].

Even though there are exceptions [141,142], many of the biogenic synthesis present in literature exploits NaOH as a precipitating agent alongside the biogenic agent

[143]. In these types of syntheses, the role of the microalgae cannot be addressed, since another well-known and established precipitating agent is triggering precipitation. Regarding this work, all the biogenic syntheses were performed without the aid of other precipitating agents, apart from the microalgae extract itself.

5.1.1. Non-biogenic synthesis

As described previously, the non-biogenic batch syntheses of ZnO particles were carried out following a modified version of the method explored by Bahnemann et al in 1987 [5]. In particular, a reaction temperature of 100 °C and a molar ratio of zinc acetate to sodium hydroxide of 1:1 was chosen. The procedure yielded a bright white precipitate with a rection yield of 71%. This sample, hereby called "ZnO 0.3", was analysed through x-ray diffraction crystallography (XRD) to define its crystal form and confirm the success of the synthesis. In the following **Figure 5.1.1 I**, the XRD diffractogram is shown.

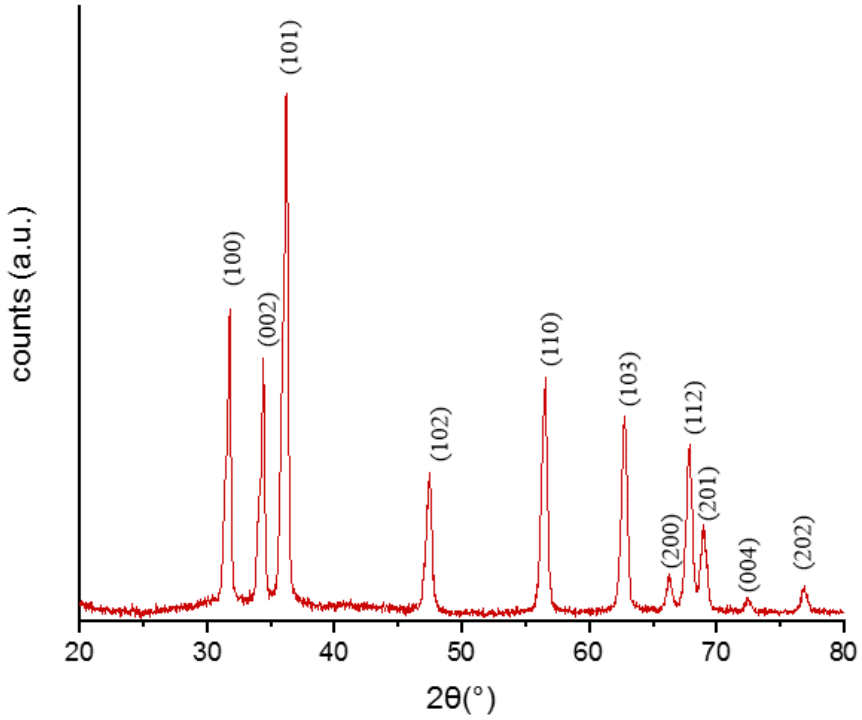

Figure 5.1.1 I *diffractogram of ZnO 0.3. Miller indices hkl were assigned based on a reference [144]*

As can be seen, the batch synthesis produced crystalline ZnO in the hexagonal structure, corresponding to the wurtzite mineral (Crystallography Open Database reference pattern ID: COD 2300112) with the space group P 63 m c (186). The reflections were indexed following a reference [144]. Moreover, with the Scherrer's equation [145,146] it was estimated a crystallite size of 22 nm which is comparable with other studies in literature [147–149].

The molar ratio, the reaction time and temperature were chosen based on a previous optimisation made by another group member [132] and are described in the experimental section of this elaborate (subchapter **7.2.1.1**).

Powder attenuated total reflectance infrared spectroscopy (ATR-IR) analysis was also carried out to study sample composition. In the next **Figure 5.1.1 II**, the IR spectrum sample "ZnO 0.3" is shown.

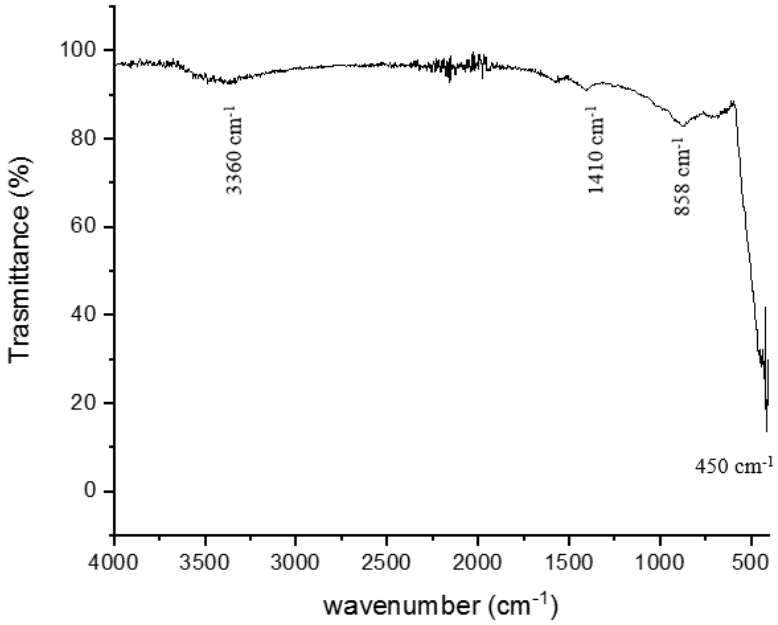

Figure 5.1.1 II *ATR-IR spectrum of the sample ZnO 0.3*

From this spectrum is not possible to clearly distinguish the Zn-O stretching mode signal near 450 cm^{-1} [150] due to the instrument detection limit. Nonetheless, there is an appreciable broad transmittance decrease in the region corresponding to the stretching of interest. Being broad and intense, compared to the other peaks, this signal indicates the presence of Zn-O bond and, more importantly, its amount against contaminants, qualitatively. Regarding this aspect, peaks at 3360, 1410 and 875 cm^{-1} are related to small traces of organic compounds and residual water. These signals are probably due to the CO_2^- scissor vibration (858 cm^{-1}) and symmetrical stretching (1410 cm^{-1}), of acetate [151]. The signal at 3360 cm^{-1} is, instead, ascribed to of residual -OH groups [152]. Since the peak intensities relative to contaminants are insignificant compared to the ZnO band, this last measure indicated the purity of the sample.

Zeta potential measurements were performed to estimate the average charge of the particles. This value is defined as the electric potential in the interfacial double layer of a dispersed particle with respect to the bulk phase [153]. In this case, it was +20 mV at pH 7. However, a colloidal dispersion is considered stable if the particles have a zeta potential higher than or equal to ±30 mV [100], reinforcing the observation that ZnO precipitates in water. Nonetheless, the value is positive as

expected since a pH of 7 is below the zinc oxide isoelectric point pH (which is 9) [154].

The NPs diameter and morphologies of the batch synthesis were measured through electron microscopy techniques. In particular, the transmission electron microscopy (TEM) was used to precisely measure the average particle size and to calculate the polydispersity of the diameter distribution. In the following **Figure 5.1.1 III** the images retrieved from the TEM analysis and the diameter distribution plot are reported.

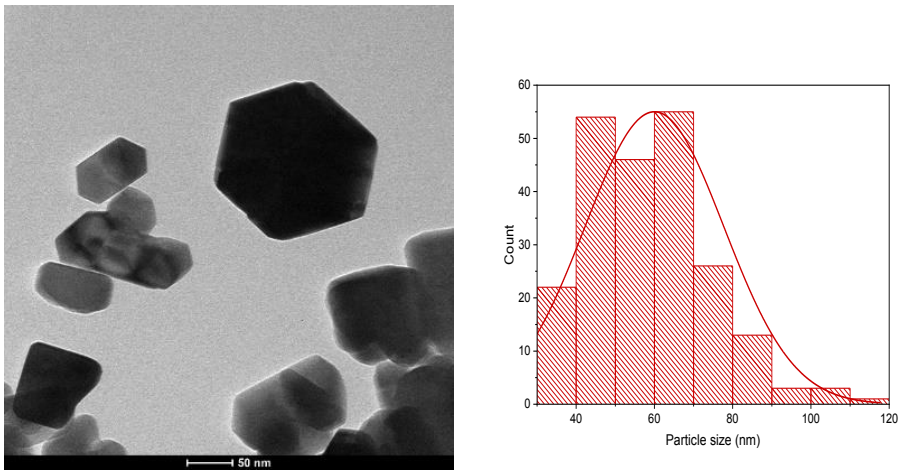

Figures 5.1.1 III *TEM images of the batch synthesis "ZnO 0.3" (on the left) accompanied by the particle size distribution plot (on the right)*

From these measurements, an average particle diameter 60±18 nm was calculated with a polydispersity index (PDI) of 0.3. In particular, for solid particles, this value is calculated as the ratio between standard deviation and the average size of particles, varying between 0 and 1. For a PDI value smaller than 0.2, the suspension is considered monodispersed, whereas if it is between 0.2 and 0.5 is on average polydisperse. Lastly, values higher than 0.6 represent highly polydisperse distributions [155]. Having described that, it is safe to define the polydispersity of this synthesis on average polydisperse, making this sample suitable as a standard also from this point of view.

Regarding microscopic measurements, scanning electron microscopy (SEM) method was exploited to determine the morphology of the particles. In **Figure 5.1.1 IV**, a SEM image of the ZnO particles is shown.

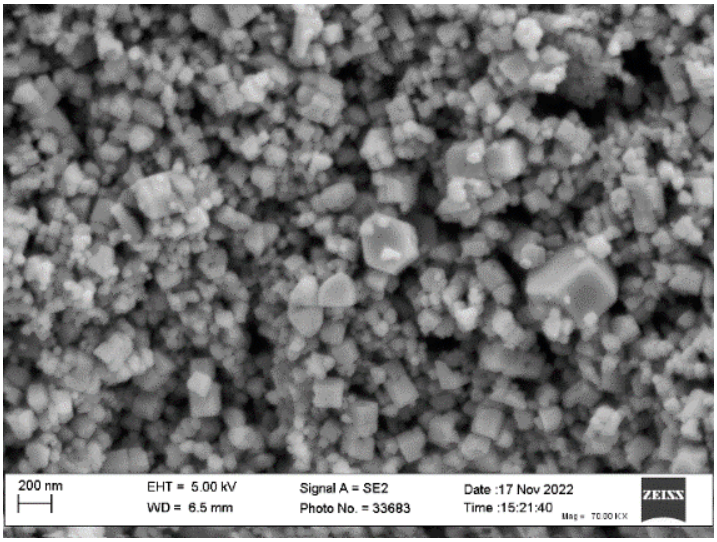

Figure 5.1.1 IV *SEM image of the particles from sample "ZnO 0.3"*

As can be seen in the picture, the morphology is similar to prisms with hexagonal bases which is common for ZnO NPs, considering the hexagonal crystal lattice of wurtzite [156–158].

Another non-biogenic synthesis explored in this work is the hydrothermal one. As explained previously in the dedicated section (**3.1.1**), this method consists in conducting reactions under unconventional conditions, namely, above 1 atm of pressure and at a temperature above the solvent boiling point thanks to a hermetically closed system. In order to have another synthesis comparison, also this particular synthesis method was investigated. Initially, the same molar ratio of the previous synthesis (1:1 zinc acetate to sodium hydroxide) was used. This procedure, however, (sample "ZnO 1.2") generated a yield of only 37%, after 24 hours of reaction time. For that reason, another sample was produced doubling the reaction time ("ZnO 1.3") albeit, even this time the yield was only 35%. Even these samples were analysed through XRD and the diffractograms are reported in the next **Figures 5.1.1 V** and **5.1.1 VI**.

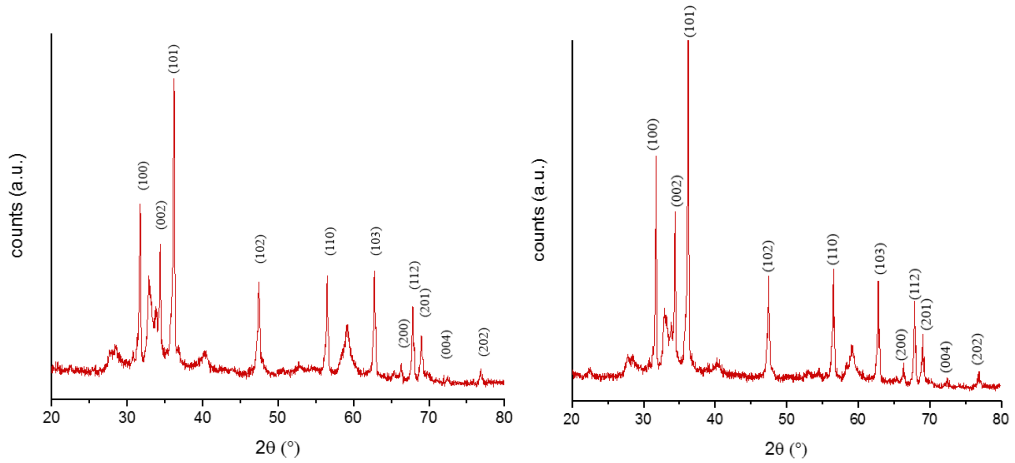

Figure 5.1.1 V and 5.1.1 VI *Diffractogramsof samples 1.2 (on the left) and 1.3 (on the right). Miller indices hkl were assigned based on a reference [144]*

As can be highlighted in the diffractograms, the are some reflections which do not belong to the hexagonal zinc oxide crystal lattice. These can be likely ascribed a spurious phase of hydrozincite (COD: 72-1100, C2/m (12)). Regarding that issue, it is important to note that this time only two centrifuge washing steps were performed (instead of 3, like in the previous sample) since the products were more soluble than batch syntheses and less prone to precipitate. Nonetheless, both samples appeared to be crystalline hexagonal ZnO like the previous synthesis (cod: 900887, space group P 63 m c (186)). The crystallite sizes were 50 and 61 nm for ZnO 1.2 and ZnO 1.3, respectively.

To qualitatively assess the level of contamination, ATR-IR spectroscopy measurements were performed, and the relative spectra are reported in the next **Figures 5.1.1 VII** and **5.1.1 VIII**.

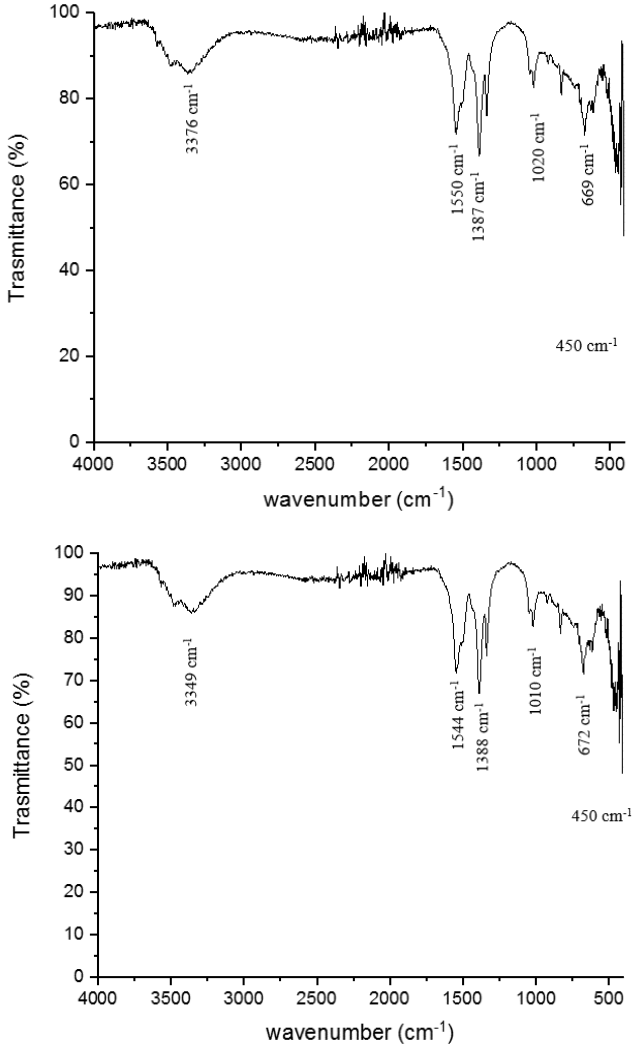

Figures 5.1.1 VII and 5.1.1 VIII *ATR-IR spectra of samples ZnO 1.2 (on top) and 1.3 (at the bottom)*

The peaks at 669 and 672 cm^{-1} are probably ascribable to CO_2^- scissor vibration and the signals at 1020 and 1010 cm^{-1} are ascribed to the acetate ion as well [151]. The peaks at 3376 and 3349 cm^{-1} (for "ZnO 1.2" and "1.3", respectively) are probably

due to the stretching of residual OH groups [152]. Since there is not a large qualitative difference between contamination peaks and Zn-O signal, the samples were not particularly pure.

Even for these syntheses, the zeta potential was estimated through electrophoretic measurements. In both cases it was positive as expected. In particular, the values were +38 and +52 mV (at pH 7) (for ZnO 1.2 and 1.3, respectively) which are above the stability threshold [100]. This high values partially explains the tendency of these particles to remain suspended during centrifugation.

To explore the size of these particles, TEM analyses were performed on each sample. As depicted in the following **Figures 5.1.1 IX** and **5.1.1 X**, different morphologies were found.

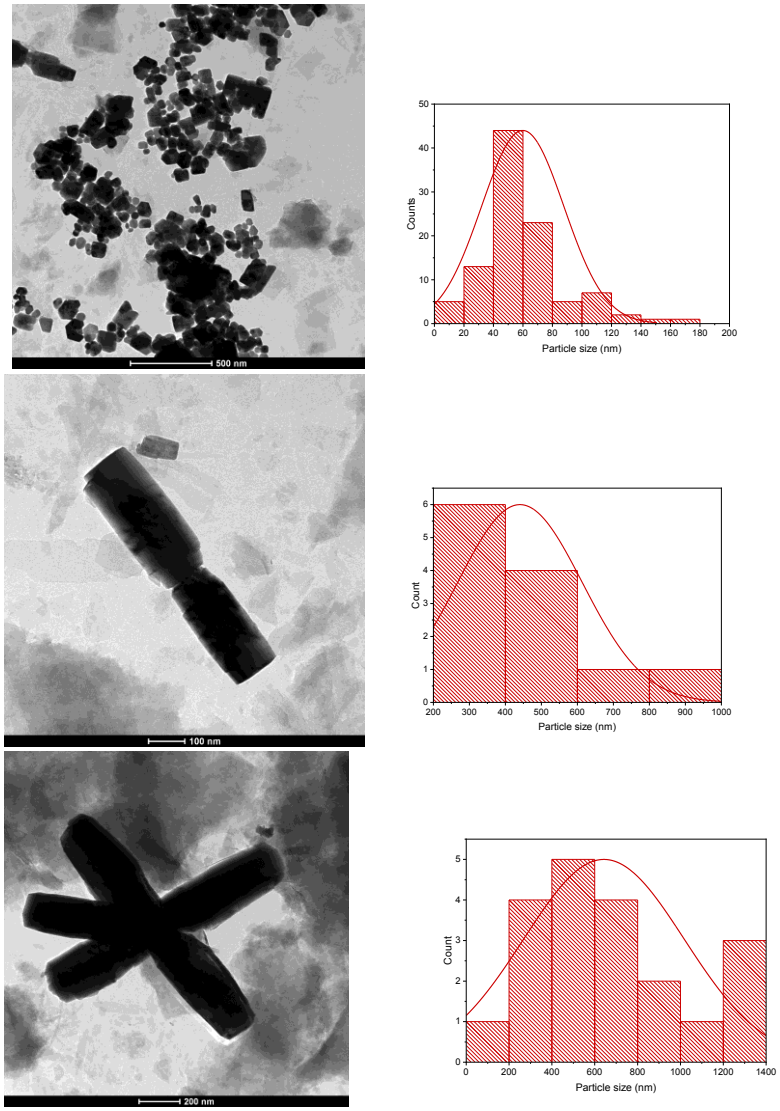

Figure 5.1.1 IX *TEM images of sample "ZnO 1.2" with different morphologies along with the corresponding size distribution plots below. From top to bottom: similar to hexagonal base prisms, nanorods and big clusters*

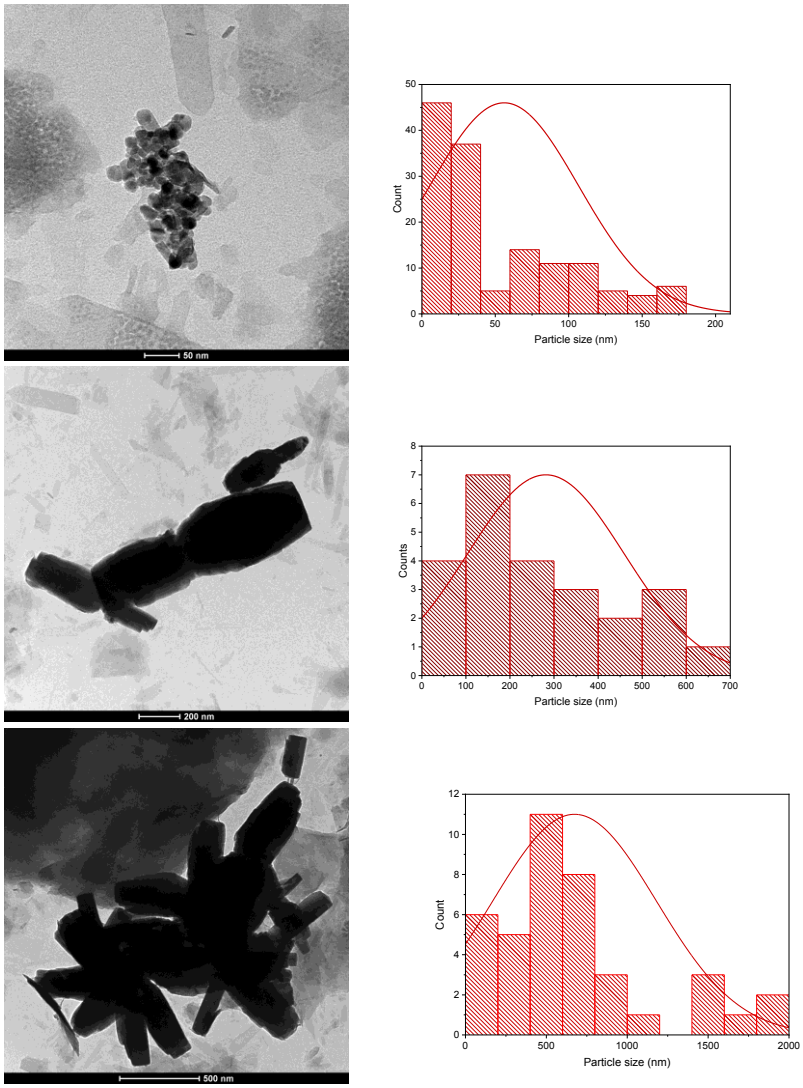

Figure 5.1.1 X *TEM photographs of sample "ZnO 1.3" with the different morphologies along with the corresponding size distribution plots below. From top to bottom: similar to hexagonal base prisms, nanorods and big clusters*

As can be evidenced by these pictures, this type of synthesis yielded different and polydisperse morphologies with particles similar to prims with hexagonal bases, nanorods and big clusters (from top to bottom of each picture set). The reason behind these results may be the need for a stabilising peptising agent during syntheses at such unusual conditions which might shape assist the obtainment of particles in a singular and more monodisperse morphology. The fact that both syntheses present the same particle morphologies with similar sizes, along with XRD data, confirm the completion of reactions during the first 24 hours. Due to the high polydispersity and lack of shape coherence, this type of synthesis was abandoned in favour of another hydrothermal protocol, in which a peptising agent to maintain a uniform morphology amongst particles.

The approach was the one from Diodati et al. [130] in which the pH was set at 10 (with a 1 M NaOH aqueous solution) while the morphology was also shaped by the presence of a peptising agent, the tetraethylammonium hydroxide (TENOH). The metal precursor was zinc acetylacetonate, in a 1:1 molar ratio with respect to oxalic acid to obtain zinc oxalate. Oxalates are prone to be decomposed into CO_2 upon heating, indeed, without leaving any contamination [159,160]. For each equivalent of oxalic acid and zinc oxalate, 0.26 equivalents of TENOH were used.

The reaction was carried out at 135 °C in a closed vessel, with a filling ratio of 55%. The overall synthesis produced a white powder precipitate with a 55% reaction yield. XRD analysis was performed in order to assess the crystallinity of the obtained compounds. In the following **Figure 5.1.1 XI**, the XRD diffractogram is reported.

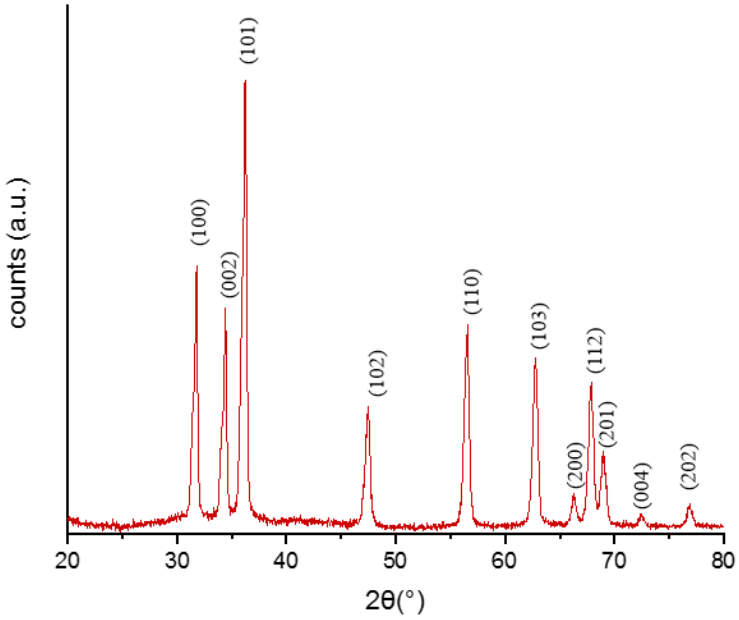

Figure 5.1.1 XI *"ZnO 1.7" XRD diffractogram. Miller indices hkl were assigned based on a reference [144]*

XRD analysis confirmed that presence of crystalline ZnO in the form of hexagonal wurtzite (COD 2300112, space group P 63 m c (186)), and no further reflections due to spurious phases were detected. In addition, Scherrer's equation allowed to estimate two different crystallite sizes: 18 and 25 nm. This result is in line with anisotropy of the particles themselves (TEM and SEM images reported further **Figures 5.1.1 XIII** and **5.1.1 XIV** respectively) and literature about elongated ZnO systems such as prisms and cones [161,162].

To verify the organic compounds decomposition, as well as to evaluate the degree of sample purity, the IR spectroscopic analysis was performed, as reported in **figure 5.1.1 XII**.

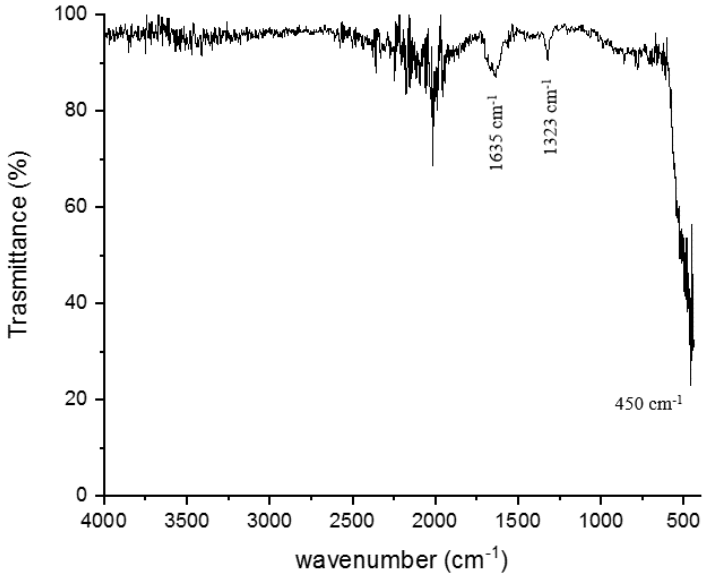

Figure 5.1.1 XII *ATR-IR spectrum of the sample "ZnO 1.7"*

As can be easily seen, there are small peaks corresponding to contamination. In particular, it is possible to recognize the band at 1638 and 1323 cm^{-1}, probably ascribable to the enolic form (1638 cm^{-1}) of acetylacetonate (being a β-diketone [163]) and C-O stretching of a carboxylic acid (oxalic or acetylacetonic acid) (1323 cm^{-1}) modes [151]. The wavy signals between 2500 and 2000 cm^{-1} are due to instrumental noise. With this measurement it was possible to confirm the purity of crystalline ZnO and the occurred decomposition of most of the organic reactants.

After that, the zeta potential was also measured. In this case, a negative charge at neutral pH (7) was observed (while all the previous samples presented a positive one). In particular, the value obtained was -8.4 mV, even if, as it was explained before, the ZnO isoelectric point is at pH 9 [154]. This unexpected value is still very close to neutrality, implying it is probably the result of residual carboxylic acids remained adsorbed onto the surface (which is likewise positive) contrasting the real charge of the particle.

As the previous samples, to define the average diameter and morphologies, the sample was analysed by TEM and SEM, **Figure 5.1.1 XIII**.

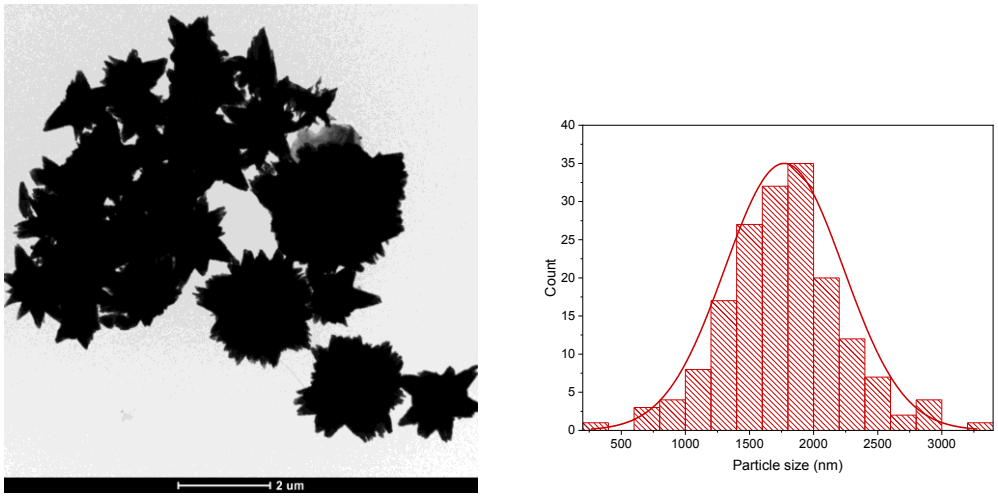

Figure 5.1.1 XIII *TEM image of the sample "ZnO 1.7" along with the corresponding size distribution plot*

As can be seen at a first glance, these particles are bigger than those obtained by the previous syntheses, with an average diameter of 1771±463 nm and a PDI of 0.3. This instance means that they cannot be defined as nanoparticles (1-100 nm [52]). The dispersion was equal to the chemical batch synthesis, being in average polydisperse.

Moreover, to define particle morphology, SEM measurement was performed, as reported in **Figure 5.1.1 IV**.

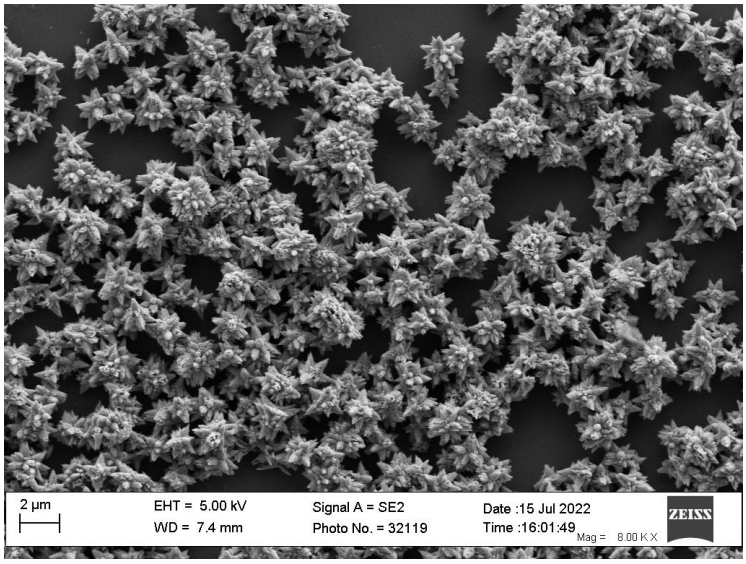

Figure 5.1.1 IV *SEM image of sample "ZnO 1.7"*

In Fig. 5.1.1 IV the particles shape can be appreciated as acicular (needle shape). This is the same morphology obtained by Diodati et al. [130], confirming the synthesis reproducibility.

All the previous measurements and analyses determined that samples "ZnO 0.3" and "1.7" are, respectively, suitable standard for the biogenic batch and hydrothermal syntheses. The following biogenic synthesis methods were tailored to

match the characteristics of these sample regarding, for instance, dimension, crystallinity and powder colour appearances.

5.1.2. Biogenic synthesis

The biogenic approach used in this project is based on the work of S. Tinello [132]. It is notable to underline, prior to the discussion, that all the following syntheses were performed at neutral pH and without the aid of any precipitating agent like NaOH. The syntheses were carried out by the biogenic agent only (apart for a small concentration of OH^- anions naturally present in solution at that pH) being more green [3] than previous state-of-art biogenic syntheses of the same compound [143].

The sample "ZnO 2.1" was produced following the approach of S. Tinello. For this sample, 1 g of microalgae was boiled for 20 minutes, filtered on paper and diluted to 100 ml with deionised water and let to react with 20 mmol of zinc acetate (1g of biogenic agent every 20 mmol of metal precursor). The precipitated product was bright green instead of white, due to the presence of biological components on the particles. The sample appearances and synthesis process are shown in the following **Figure 5.1.2 I**.

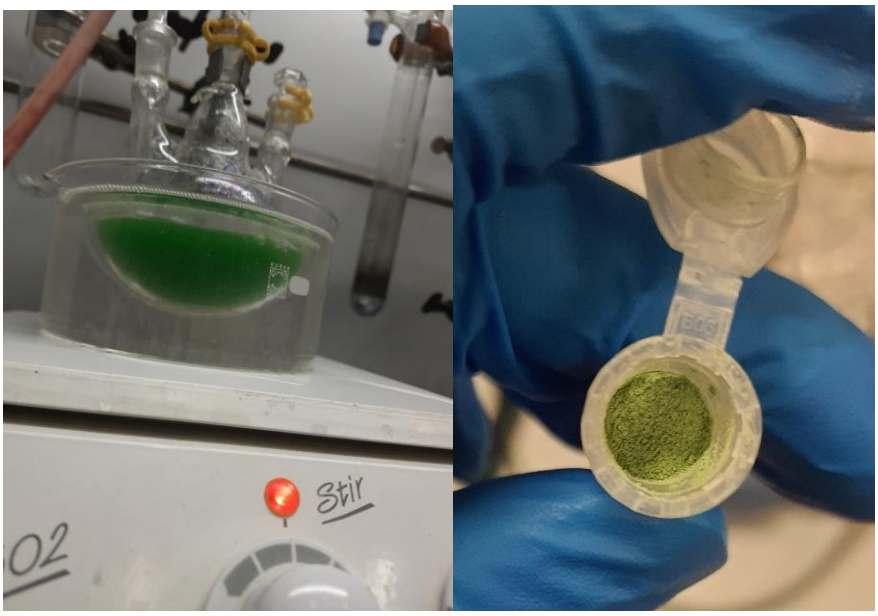

Figure 5.1.2 I Synthesis of sample "ZnO 2.1" and its powder

The apparent reaction yield was 37%. However, this high value is mainly due to the presence of biological debris which increased the product weight. According to the original work from S. Tinello, the actual product weights (estimated through thermogravimetric analyses (TGA)), were the 15% of the total. Consequently, the real reaction yield would be only 6%.

XRD analysis was performed revealing that the sample is amorphous as reported in the following **Figure 5.1.2 II**.

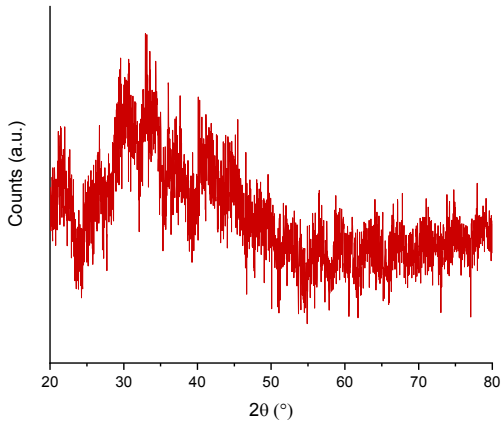

Figure 5.1.2 II *Diffractogram of the sample "ZnO 2.1"*

Then, a powder ATR-IR spectroscopy measurement was performed, and the spectrum is reported in the following **Figure 5.1.2 III**.

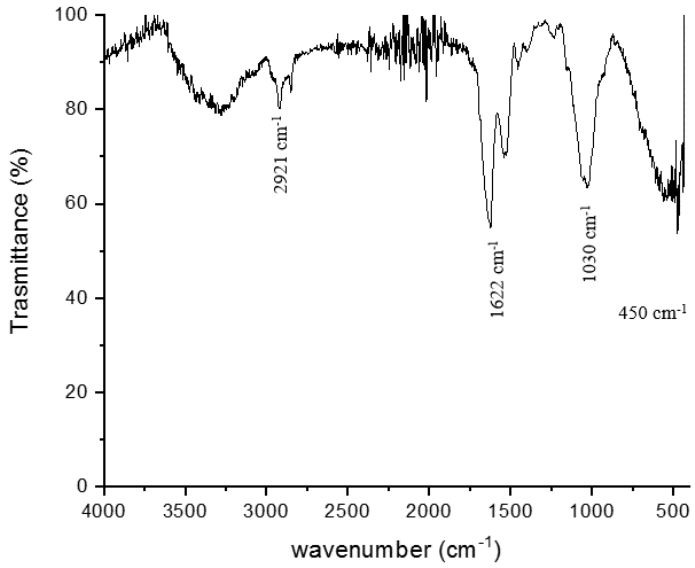

Figure 5.1.2 III *"ZnO 2.1" IR spectrum*

As can be seen, the sample appears to be contaminated by biomolecules coming from microalgae. The band near 450 cm^{-1} has an intensity similar to other signals; yet it is present, testifying the presence of Zn-O bonds within the sample. Particularly evident are the signals of O-H stretching mode (2921 cm^{-1}) from carboxylic acid dimers, amide II at 1622 cm^{-1} (which is the combination of N-H bending and C-N stretching in proteins) and the acetate characteristic band (1030 cm^{-1}), which are all due to residual of microalgae [151]. Also, these measurements, as expected, indicated the poor purity of the sample.

Since the previous protocol was problematic and never yielded a pure white ZnO powder, it was decided to improve it. In detail, the preparation of the biological extract was changed. In particular, 1 g of microalgae was left at boiling temperature

(~100 °C) until the solvent (deionised water) was evaporated and left for another 20 minutes under the same heating conditions. Once this procedure was completed, the remaining brown slurry was suspended in 100 ml in deionized water. Finally, the processed extract was filtered and used as a reactant along with 20 mmol of zinc acetate (like the previous synthesis, 1 g of microalgae each 20 mmol for precursor) precipitating the sample "ZnO 2.2". This approach was used in order to take advantages from heat (boiling temperature) and atmospheric O_2 to partially burn the biogenic agent to decompose phenols, chromophores and other organic compounds which may not be part of the synthesis mechanism, yet they can interfere with particles production and sample purity. In literature most of biogenic productions of ZnO rely on a post-synthesis calcination step (with temperatures between 350 and 700 °C), with the aim of purifying the final product and to obtain a crystalline ZnO [142,164,165]. Calcination is an extreme energy demanding activity for industries, requiring a significant amount of heat [166]. For these reasons, the use of a milder heating step was chosen.

This approach was successful since it yielded white crystalline ZnO particles, comparable to the one made with the classical batch approach while still using less energy compared to a state of art calcination-assisted biogenic synthesis. The use of a biogenic agent and less heat are coherent with the principles of green chemistry, in particular the use of less hazardous synthesis (3° principle) and the design for energy efficiency (6° principle) [3].

To assess the synthesis efficiency and comparability in regard to its batch counterpart (sample "ZnO 0.3"), the same analysis and measurements sets were performed onto this product. Firstly, an apparent reaction yield of 5% was calculated. Even if it is lower than the yield obtained with "ZnO 0.3", the value is similar to the ones obtained by S. Tinello with TGA analyses. Then a XRD analysis was performed (**Figure 5.1.2 IV**).

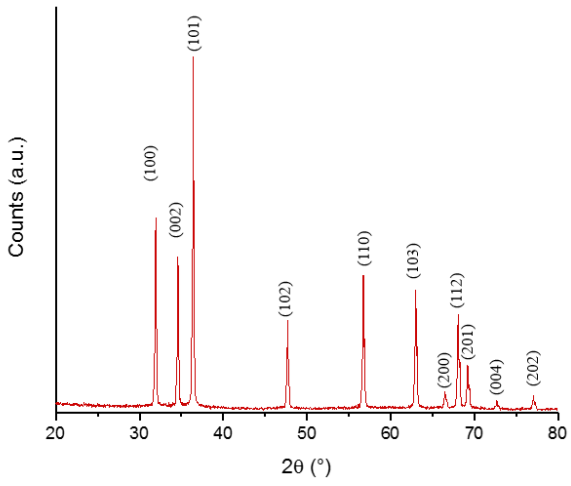

Figure 5.1.2 IV *XRD pattern of sample "ZnO 2.2"[144]*

As can be evaluated by the diffractogram, this method yielded crystalline hexagonal ZnO (COD 900887, space group P 63 m c (186)), just like its batch reference sample. In this case, the calculated crystallite size was 56 nm which is significantly higher than the one from "ZnO 0.3" (22 nm).

Then, IR spectroscopy analysis was performed, as reported in **Figure 5.1.2 V**.

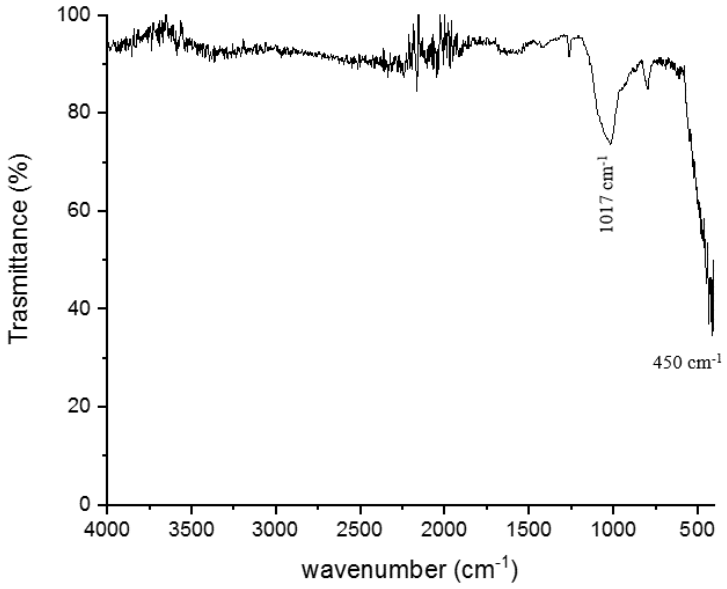

***Figure 5.1.2 V** ATR-IR spectrum of sample "ZnO 2.2"*

As can be seen, the presence of Zn-O stretching signal confirms the presence of the corresponding bond. Besides instrumental noise between 1750 and 2500 cm^{-1} and the acetate peak at 1017 cm^{-1}, there are not signals ascribed to microorganism adsorbed biomolecules, being the spectrum very similar to "ZnO 0.3". This analysis further confirms the higher product purity of this new biogenic protocol with respect to the previous one.

Zeta potential measurement was also performed resulting in a value of -19 mV at neutral pH. This result is ascribed to the presence of various biomolecules adsorbed onto the particles which confer a negative charge.

Finally, TEM analyses were performed as well and in **Figure 5.1.2 VI** the particle TEM micrograph and the corresponding size distribution plot are depicted.

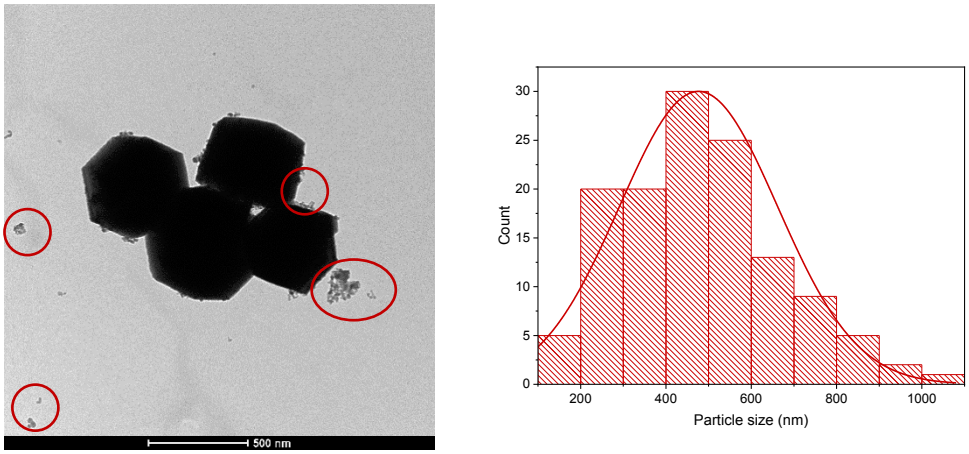

Figure 5.1.2 VI *TEM images of sample "ZnO 2.2" and its size distribution plot. In red circles, some of the microalga debris are highlighted*

As can be seen in the image, the particles are bigger than the ones produced with the batch method. having an average diameter of 476±186 nm. This value is in agreement with biogenic syntheses performed previously by S. Tinello [132], as well as, the PDI being about 0.4 which is still considered on averagely polydisperse. To define the morphology, SEM images were taken and reported in **figure 5.1.2 VII**.

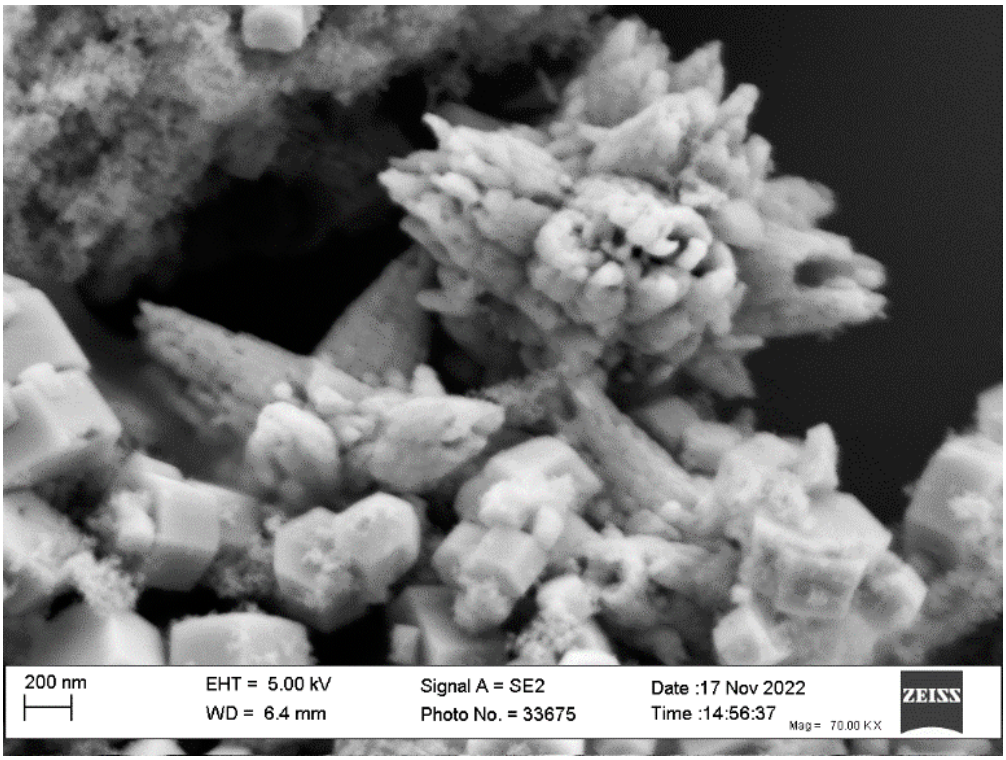

Figure 5.1.2 VII *SEM image of sample "ZnO 2.2".*

In the Fig. 5.1.2 VII it is possible to observe particles shaped like hexagonal prisms along with the presence of bigger acicular-like aggregates. Nonetheless, microalgae debris are still present adsorbed on particles (see red circles in **Figures 5.1.2)**,

highlighting that, even with this enhanced protocol, a little biomolecules amount is still present.

In conclusion, referring to the batch synthesis benchmark ("ZnO 0.3"), the obtained biogenic particles had a bigger size and crystallite size and a positive surface charge. However, the sample "ZnO 2.2" has less biogenic agent adsorbed on the surface compared to "ZnO 2.1", meaning that the first one is more similar to the one made with batch method. Moreover, "ZnO 2.2" is crystalline and has the same appearances as the batch product. In conclusion, this biogenic synthesis is suitable for all the applications that need cheap ZnO big particles without an excessive product purity. The biogenic synthesis is considered more economic and sustainable than conventional chemistry because of microalgae. For instance, they can be obtained as industrial discards from other processes like wastewater flocculation [105] diminishing the synthesis cost. As last consideration, the presence of microalgae debris may also enhance the biocompatibility of the product (which is already high, being ZnO considered to be a GRAS compound) [24,167].

Using the sample "ZnO 1.7" as a benchmark, also biogenic-hydrothermal syntheses were tried by performing the biogenic synthesis into a hydrothermal vessel. However, none of the various ratios (grams of microalgae over mmol of metal salt) generated any product after 24 hours of reaction time at 135 °C with a filling ratio of 48%, determining the abandonment of the biogenic-hydrothermal research line. The probable causes are the extreme conditions met in hydrothermal syntheses in which high temperatures and pressures may have interfered with the role of the biogenic agent, deactivating it. Nevertheless, hydrothermal reference sample "ZnO 1.7" was kept and still functionalised with polymers to generate a stable water suspension, for further considerations. In the **Table 5.1.2 VIII** the biogenic-hydrothermal attempts are reported and summarised.

Sample	Zinc acetate (mmol)	Microalgae (g)	Zinc acetate/microalgae (mmol/g)
ZnO 4.0	2	0.05	1 : 0.025
ZnO 4.1	2	0.10	1 : 0.050
ZnO 4.2	2	0.50	1 : 0.250

Table 5.1.2 VIII *List of ZnO biogenic-hydrothermal syntheses*

5.2. Silver nanoparticles synthesis

As stated before, even for metallic silver, the aim is the obtainment of stable water suspensions of nanoparticles synthesised through biogenic methods. The synthesis product is a colloidal dispersion. Nevertheless, biogenic synthetised metallic silver do not have the same colloidal stability with respect to the Turkevich conventional batch counterparts, unless in high ionic strength conditions [168]. On the other hand, is reported in literature that biogenic particles should be highly stable due to the stabilisation effect brought by the adsorbed charged biomolecules [169]. Biogenic syntheses produced in this thesis were not considered stable, hence polyoxazolines were employed to stabilise the suspensions [170].

Even for AgNPs the biogenic synthesis mechanism is not completely clear, however, there is the reduction of metal cations (oxidation state +1) to their metallic form (oxidation state 0). For this reason, we can assume that biomolecules act as both scaffolding and reducing agents [9]. The biomolecules probably involved in this process are flavonoids and terpenoids [97], polysaccharides [95] and reductive enzymes such as flavoproteins and nitrate reductases [96,98]. Even considering the greater consensus amongst the reductive mechanism (in contrast to zinc oxide) there is not a precise knowledge of which biomolecules are involved. Therefore, even in this case, extensive studies would be required. In particular, HPLC-MS, XAS and biochemical essays such as immunoprecipitation could be performed. In addition, the majority of studies about biogenic silver nanoparticles are conducted using leaf extracts or bacteria, determining more difficulties to identify the organic compounds involved in microalgae [171]. Taking into account the cost-effectiveness, biocompatibility and antibacterial activity, it is crucial to continue these researches [172–175], thanks to the already established market of AgNPs as sanitising agents (representing 50% of commercialised nanoparticles in 2015 [63]).

Despite its peculiar synthesis mechanism, biogenic silver nanoparticles growth can be modelled with the LaMer-Sugimoto model, likewise their batch counterparts [83,84,176]. As shown in the following **Figure 5.2 I**, this model is based upon the idea of the existence of two temporarily separated main steps during which the synthesis of nanoparticles takes place: nucleation and growth.

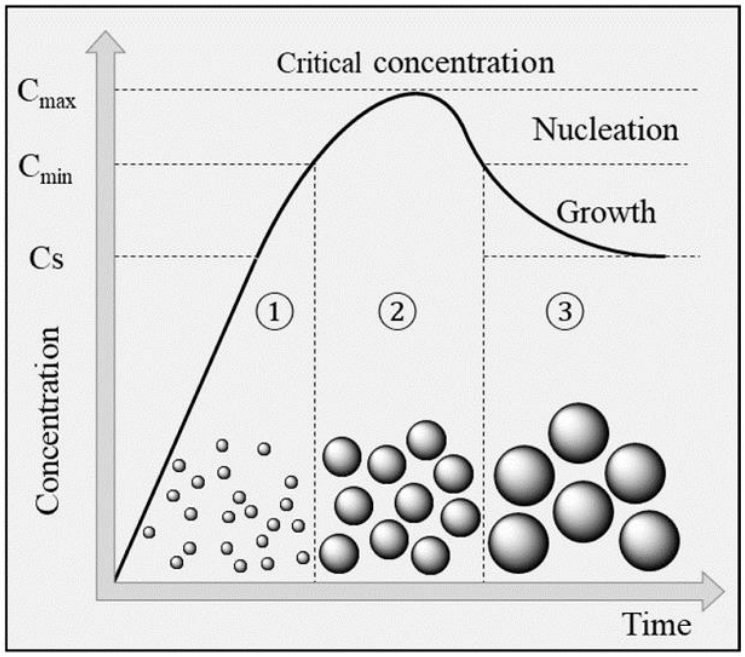

Figure 5.2 I *LaMer-Sugimoto nucleation model for nanoparticles formation [177] where the number refers to the generation of metallic atoms (1), nucleation (2) and growth (3) phase*

As shown in the figure the addition of metal precursor triggers the generation of metallic nuclei (oxidation number 0). After reaching a certain concentration of reagents (above the solubility), small clusters are formed, due to atoms aggregation (nucleation), which eventually grow, through mass diffusion, into bigger particles [83].

Smaller nanoparticles are demonstrated to generally possess a higher colloidal stability [57] and present a smaller surface, which facilitates the polymeric ligand coating process. For this reason, the obtainment of small sizes was a target of this thesis. As shown in the previous **figure 5.2 I**, the growth of particles relaxes the supersaturation (defined as the ratio between the actual precursor concentration and its solubility in the current solvent [178]) thereby preventing further nuclei from being produced. This means that, to obtain smaller and more monodisperse nanoparticles, the phases of nucleation and growth should be as temporally separated as possible. One of the possible route is the use of pre-synthesised nanoseeds of the same material in order to skip the nucleation phase and obtain monodisperse, bigger particles [179]. Nonetheless, focusing the synthesis on the nucleation phase would be desirable [176] since faster nucleation leads to smaller crystals (as well as high supersaturation) [180].

These colloidal systems are tunable since their morphology and sizes are influenced by many experimental conditions, such as stirring rate, temperature, precursor to reductant molar ratio and pH [181]. Regarding this thesis, two main parameters were explored: reaction time and reactant addition order. An excessively long reaction time leads to particle aggregation, eventually resulting in loss of colloidal stability, colour change to darker tones and the precipitation of silver as bulk

material. Even though colour change is a good indicator for silver Turkevich synthesis completion (from transparent to yellow, due to the occurrence of Plasmon resonance [48]), timing the reactions was found to be a more reproducible manner to assess the most suitable moment for synthesis quenching.

The other parameter evaluated was the reactant introduction order. With the aim of focusing the process within the nucleation phase, the "reverse" method was used for Turkevich and biogenic methods. The metal salt was added to a hot stirring water solution already containing an excess of reducing agent, contrarily to classical technique. This process may cause the quasi-instantaneous generation of several small nuclei, exhausting the Ag^+ in solution before the starting of growth phase. In literature, this method produces smaller and more monodisperse particles for colloidal gold synthesis [182,183] (compared to the classical Turkevich method [7]) which implies it may lead to the same outcome for silver particles as well. Moreover, since biogenic synthesis is known as a method which intrinsically produces wider size distributions [184], syntheses with microalgae were performed with the reverse method, in order to minimize polydispersity (meaning, the metal salt was added to a solution of microalgae and not vice versa). Being more similar to the biogenic synthesis, the reversed synthesis, along with the classic one, is considered as the comparison benchmark for the biogenic method.

During these syntheses, the pH did not change significantly (remaining neutral) in both biogenic and non-biogenic samples and were carried out under vigorous stirring. Finally, in biogenic syntheses, similarly to ZnO, only the metal precursor salt and the biogenic agent were exploited without the aid of other chemicals, assuring the products are only the results of microalgae presence.

5.2.1. Turkevich method

The method used was a modified version of the Turkevich colloidal gold method [7] adapted for silver. A molar ratio of 1:3.4 silver nitrate to sodium citrate was used in all non-biogenic synthesis. The excess of citrate was chosen with the aim of obtaining small particles completely covered and stabilised by organic molecules [185].

From preliminary attempts of AgNPs batch syntheses (not reported), it was obvious that reaction time was the most important parameter to avoid unstable sols. For that reason, initially both the reverse and normal methods were performed and every minute a time point sample was taken (from 0 to 5 minutes). The success of syntheses were assessed by UV-Vis spectroscopy measurement in which the occurrence of the silver surface plasmon resonance was observed [48,186]. In the following **Table 5.2.1 I**, the samples synthesised, and their maximum absorbance are reported.

Normal		Reverse		
sample	**λ_{max}(nm)**	**sample**	**λ_{max}(nm)**	**Reaction time (minutes)**
Ag Normal 1 min	/	Ag Reverse 1 min	/	1
Ag Normal 2 min	396	Ag Reverse 2 min	411	2
Ag Normal 3 min	413	Ag Reverse 3 min	410	3
Ag Normal 4 min	420	Ag Reverse 4 min	413	4
Ag Normal 5min	/	Ag Reverse 5 min	/	5

Table 5.2.1 I *List of samples synthesised through Turkevich normal and reverse colloidal silver routes.*

As can be seen in the previous table, for both syntheses, samples with a reaction time of one and five minutes do not have an absorbance maximum reported. The reason behind is the impossibility of observing to see any colour change or measure a plasmon resonance absorbance peak before 2 minutes, indicating the absence of nanoparticles. After the fifth minute, on the other hand, the sols assumed a dark silver colour caused by particle aggregation into bulk material, thereby determining the synthesis failure. In the following **Figure 5.1.2 II**, the absorbance spectra of samples obtained between two and the four minutes of rection time are reported.

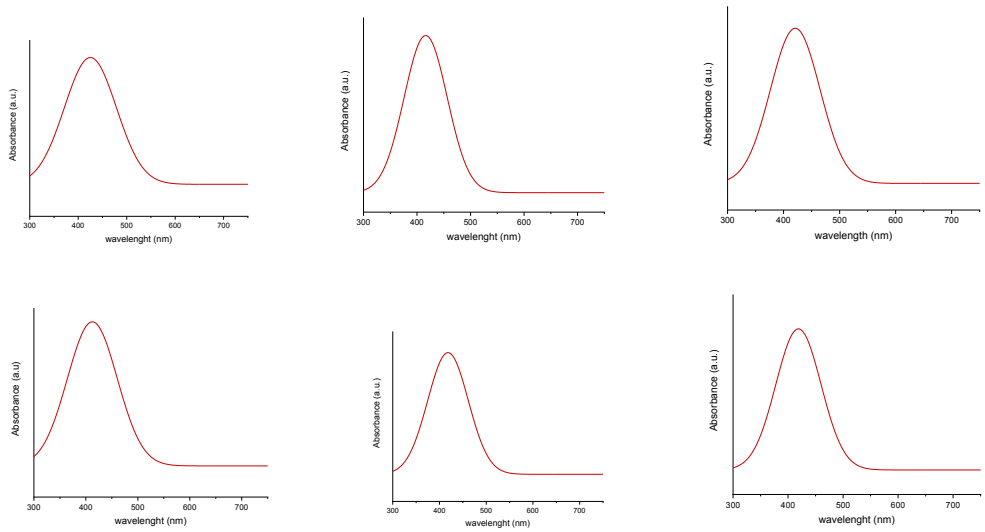

Figure 5.1.2 II *UV-Vis spectra of the following samples: on the top line (from left to right): "Ag Normal 2 min","Ag Normal 3 min" and "Ag Normal 4 min"; on the bottom line (from left to right) "Ag Reverse 2 min","Ag Reverse 3 min" and "Ag Reverse 4 min"*

As can be seen in the spectra and the table, all samples present broad absorption peaks near 390-420 nm which is compatible with the silver plasmonic resonance of particles with sizes smaller than 30 nm [68,187,188].

To determine long term colloidal stability of these samples, the surface zeta potential was measured and monitored for 1 week. See the following **Table 5.1.2 III**.

Sample	Ag Normal 2 min	Ag Normal 3 min	Ag Normal 4 min	Ag Reverse 2 min	Ag Reverse 3 min	Ag Reverse 4 min
Zeta potential (mV) 3 days	-37	-41	-46	-41	-58	-47
Zeta potential (mV) 5 days	-44	-46	-42	-48	-43	-46
Zeta potential (mV) 7 days	-47	-47	-49	-41	-45	-42

Table 5.1.2 III *Zeta potential measurements of non-biogenic silver syntheses*

As can be seen in the previous table, besides some minor oscillations ascribed to experimental error, the surface charge remained stable throughout the time lapse evaluated for every sample. Moreover, all the measurements reported a zeta potential value above the colloidal stability threshold of ±30 mV [100]. These data suggest that all samples should not undergo aggregation and precipitation processes during in a reasonable time frame.

To have a more precise measure of colloidal stability, the plasmon UV-Vis maximum absorptions were monitored as well and for a longer timeframe. The data are shown in the next **Table 5.1.2 IV**.

Sample	**λ_{max}(nm) 3 days**	**λ_{max}(nm) 5 days**	**λ_{max}(nm) 7 days**	**λ_{max}(nm) 14 days**	**λ_{max}(nm) 28 days**
Ag Normal 2 min	408	422	417	423	430
Ag Normal 3 min	417	415	412	424	432
Ag Normal 4 min	420	420	425	425	432
Ag Reverse 2 min	420	414	421	420	420
Ag Reverse 3 min	417	419	421	425	427
Ag Reverse 4 min	418	423	421	425	428

Table 5.1.2 IV *Time resolved λ_{max} shifts of non-biogenic silver syntheses*

The spectroscopic data confirmed an overall colloidal stability for every sample within two weeks. However, after 14 days there is a more sensible redshift for samples made with the standard Turkevich method. These data suggest that the reverse method may produce more stable sols.

Finally, the long-term stability was evaluated through the optical observation of sols for four weeks. Pictures of this analysis are reported in the next **Figure 5.1.2 V**.

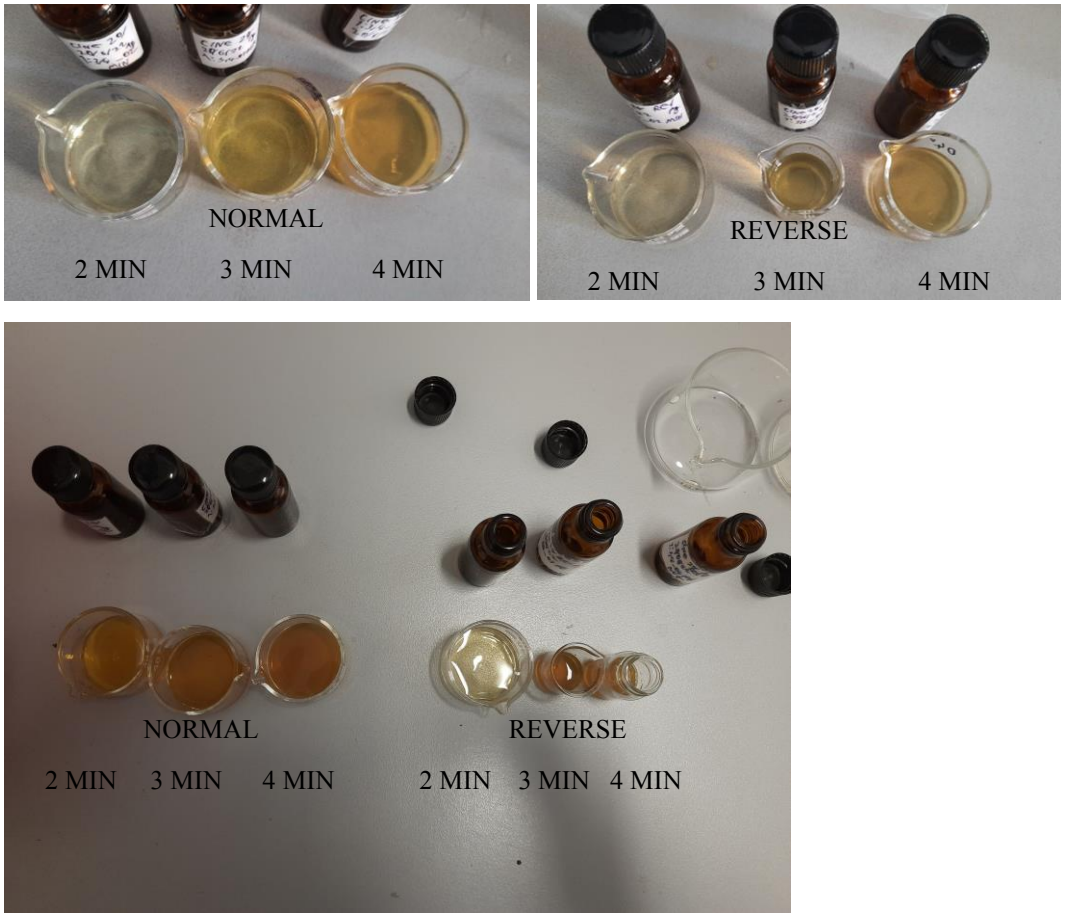

Figure 5.1.2 V *Long term analysis of batch silver samples. on top samples freshly made are shown whereas at the bottom, they are shown after 4 weeks.*

As it is evident from the pictures in **Figure 5.1.2 V**, there was a net colour change in the samples produced via the classical Turkevich approach and a reaction time greater than two minutes after the first week. This observation confirms the idea of the increased colloidal stability of the "reverse" samples with respect to the standard ones. Nonetheless, every sample showed a colour change after four weeks except for the ones synthetised with a reaction time of 2 minutes. Consequently, these two samples were chosen to be the reference standard as they were the most stable.

The TEM analysis was performed onto "Ag Normal 2 min" and "Ag Reverse 2 min". In **Figures 5.1.2 VI** and **VII**, results are shown.

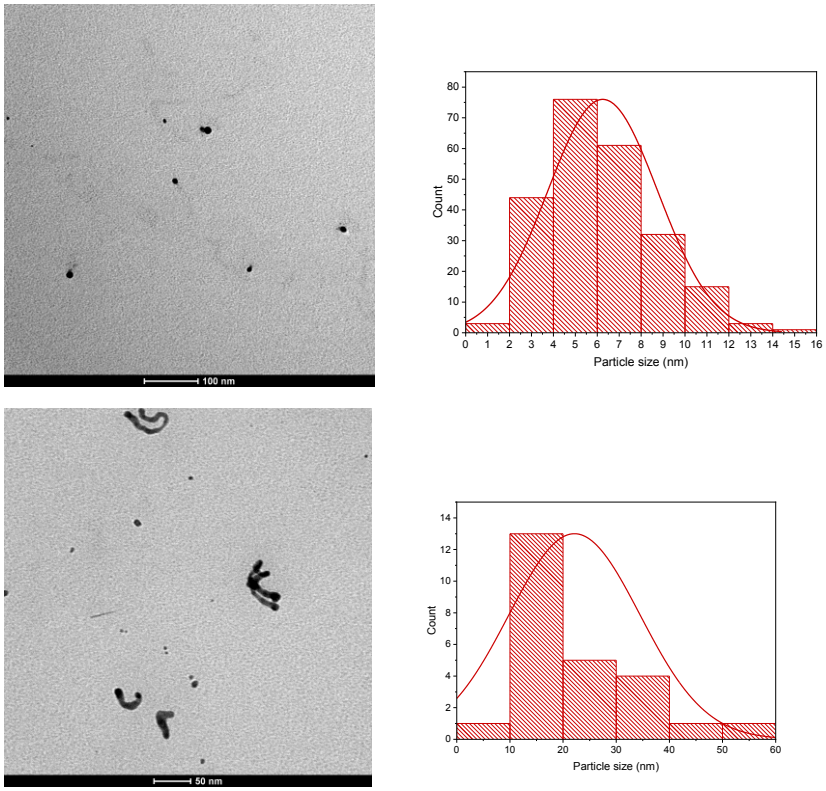

Figure 5.1.2 VI *TEM images of sample "Ag Normal 2 min" with the different morphologies found (on the left) accompanied by the corresponding size distribution plots (on the right). On the top row: small spherical particles; on the bottom row: anisotropic aggregates*

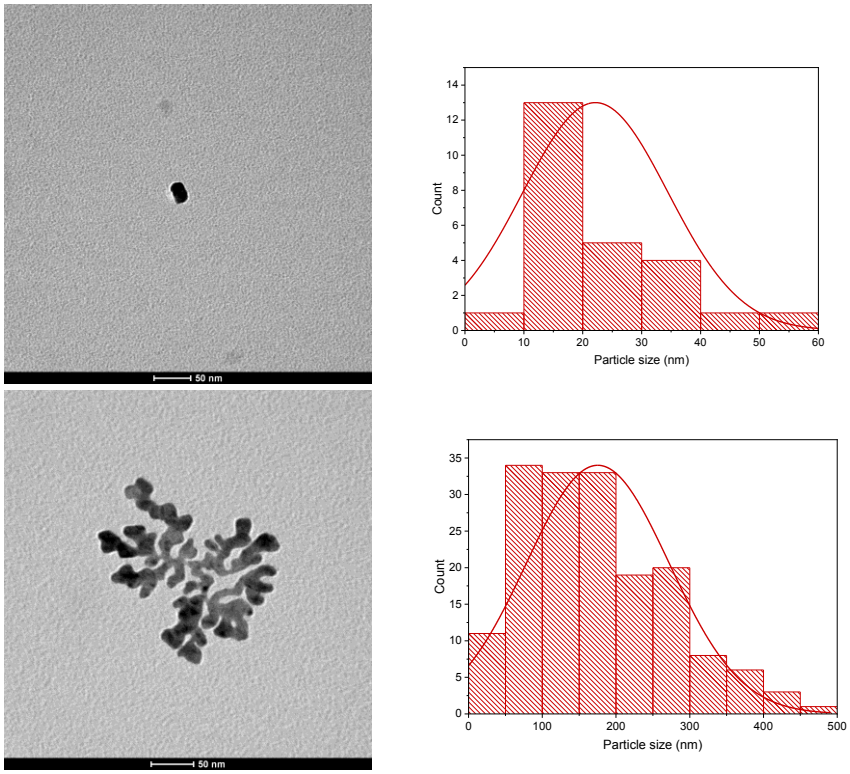

Figure 5.1.2 VII *TEM images of sample "Ag Reverse 2 min" with the different morphologies found (on the left) accompanied by the corresponding size distribution plots (on the right). On the top row: small spherical particles; on the bottom row: anisotropic aggregates*

As can be seen in the previous images, alongside particles, these is a small component of anisotropic aggregates (of 22 and 175 nm, for the "Ag Normal 2min" and "Ag Reverse 2min", respectively). As confirmed by the analysis, even though there were not macroscopic precipitates in these sols, some nanoparticles still aggregated. For the reverse synthesis, this effect was more evident, generating bigger aggregates. Nevertheless, contrary to what expected, nanoparticles produced with the reverse method featured a bigger diameter (20±7 nm) compared to the ones obtained with the conventional techniques (6.0±3 nm). At first glance, it may be seen as a worse synthesis, however "Ag Reverse 2 min" was slightly more monodisperse (PDI 0.3) than is traditional counterpart (PDI 0.4) (even being both average polydisperse [155]). However, since monodispersity is, generally, a more desirable feature than smaller sizes; it is hereby possible to state that the reverse Turkevich method is a better synthesis for technological applications that do not require nanoparticles below 20 nm. SEM measurement were not possible due to the instrument detection limit above the dimensions of the nanoparticles at issue.

Regarding TEM measurements, it is worth noting that the aggregates represent a only small portion of the particle population. Then, to avoid the formation of these components, the samples to be used for polymer functionalisation were synthetised and used fresh withing the first 24 hours (using the hereby established optimal reaction time and conditions). Even though the Turkevich method is based upon the subjective colour change observation (which is not to be highly reproducible [92]), the exploitation of the same optimised conditions, such as reaction time, should lead to the same product. This implies that even if the functionalised samples were not the ones subjected to the analysis, they still retained the same characteristics of the ones used in microscopic analysis, in term of size distribution.

5.2.2. Biogenic synthesis

In this part the biogenic syntheses were performed following the reverse Turkevich method in which instead of adding $AgNO_3$ to a boiling solution of citrate, the metal salt was added to a hot stirring suspension of microalgae extract. However, in the very first attempt, the conventional Turkevich addition order was used (first the salt then the reducing agent). This choice is functional to the type of experiment preformed. The first parameter explored was the ratio between microalgae extract and metal salt required to obtain AgNPs. 1 ml of biogenic agent (10 g/l) were added to a hot stirring solution of $AgNO_3$ (with the same quantity in mass of precursor of the batch syntheses, for reference, 0.017 g, 0.1 mmol) every fifteen minutes.

Right after the addition of the first milligrams of microalgae, the solution turned from bright green to a slightly greyer tone, probably due to interactions of Ag^+ cations with negatively charged molecules withing the microorganism which, as a result, shifted their absorption spectra. Nevertheless, it is not ascribed to AgNPs formation. After adding 0.04 g of extract to the solution, a slight shade of pink was

observed, however, only after 0.1 g the colour changed markedly, indicating the presence of nanoparticles. Unfortunately, it was not possible to perform spectroscopic analyses due to the high optical density of the sols, the presence of chromophores from the photosynthetic organism and instrumental saturation. Thereby, apart for optical observation, there are not further indication of AgNPs existence within the liquid.

DLS analyses were performed onto samples recovered by the sols after adding 0.04 and 0.1 g total of extract (called "Ag BIO 4ml" and "Ag BIO 10 ml", respectively). For these two samples, the measured hydrodynamic diameters were, respectively, 123 and 178 nm. Even though the sizes increased as time passed by, as expected, these values are not considered reliable since the measurements were performed 6 hours after the synthesis, meaning the data obtained are to be referred to larger aggregates (due to colloidal instability). Every biogenic silver sols synthesised in this thesis, which were not subjected to further purification steps to remove adsorbed and non-adsorbed biomolecules (namely, centrifugation, filtration, polymeric ligand exchange and dialysis), were completely subjected to precipitation during the first 12 hours of shelf life.

Moreover, zeta potential measurements were taken as well. The samples presented a charge of -26 and -22 mV ("Ag BIO 4ml" and "Ag BIO 10ml", respectively). These values mark the instability of colloidal suspensions, thereby explaining the appearance of a precipitate after such short time.

Once established that 0.1 g of microalgae and 0.1 mmol of $AgNO_3$ are needed to obtain a net solution colour change (thereby, generating AgNPs), all the following syntheses were performed using the reverse technique. In particular, since the heating is one of the most expensive industrial activity [166,189], beside the classical approach of heating the extract solution, reactions were performed also at room temperature (RT). Even if in the work of S. Tinello [132], a sufficient heating was required to produce biogenic ZnO, the elevate concentration of reductive compounds within microalgae was sufficient to synthetise metallic silver particles at RT.

The first samples produced were "Ag BIO 3.0 100 °C" and "Ag BIO 3.1 RT" which, as the names suggest, were performed respectively at boiling point and at room temperature. Even for these samples it was not possible to evaluate the absorption spectra, being the signal too weak. However, the optical observation of samples during synthesis determined the reaction time required for a colour change from green (microalgae) to pink-yellow. In particular the at boiling point condition, the reaction time was 45 minutes, whereas the reaction conduction at room temperature required 24 hours. For these syntheses (and all the following discussed in this section), as soon as $AgNO_3$ was added the solutions turned from bright green to a grayish green, due to Ag^+ ions being coordinated by chromophores present in microalgae.

Finally, DLS measurements were performed. The hydrodynamic diameters were 69 and 38 nm (for the synthesis at boiling point and at room temperature, respectively). This analysis was exploited to have an indication of particle formation due to the impossibility to visualise an absorption spectrum or obtaining a sample powder to be analysed with XRD diffractometry. These data suggest that room temperature synthesis yielded smaller particles. This statement was later confirmed by TEM (**Figures 5.2.2 II** and **III**).

Having established the quantity of biogenic agent and the reaction time required, the following step of this research was devoted to separate microalgae debris from nanoparticles with the aim of improving colloidal stability (since microalgae extract showed a tendency to precipitate on its own) and detect a plasmonic resonance through UV-Vis spectroscopy. To precipitate the microalgae a mild setting of 7000 rpm for 3 minutes was chosen. The resulting supernatant and pellet are shown in the following **Figure 5.2.2 I**.

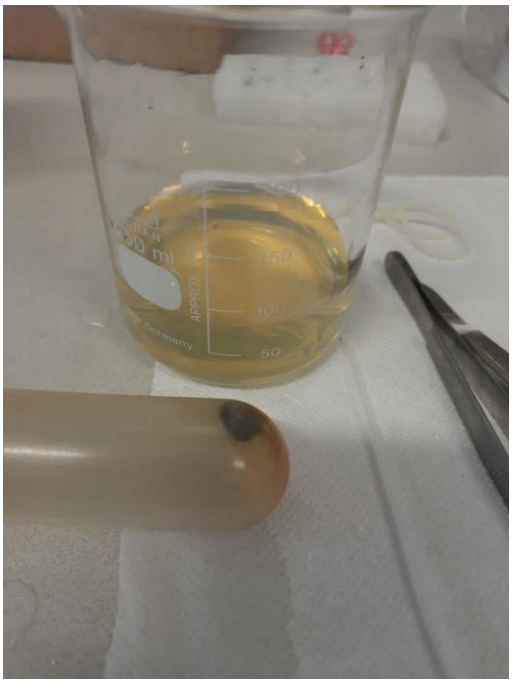

Figure 5.2.2 I *Picture of sample "Ag BIO 3.9 100 °C-C", the supernatant is stored in the becker in the background whereas the pellet is in the centrifuge tube (bottom-left)*

In the previous picture the classical silver colloidal yellow suspension (even if with a tonality similar to green) is present in the supernatant, whereas the pellet mostly contained microalga debris. Assuming similar sizes and tendency to precipitate between room and boiling point temperature synthesis products, this first purification step was essayed only for the hot biogenic synthesis. Moreover, before the centrifuge step, the sol was split into two samples, namely "Ag BIO 3.9.1 100 °C-YES C" and "Ag BIO 3.9.2 100 °C-NO C". The treatment was performed only for the first one whilst the other was kept as a control reference. After this procedure, "Ag BIO 3.9.2 100 °C-NO C" lost its stability after 24 hours whereas the other one remained suspended for 3 days. The last consideration further

underlines the confinement of particles in the supernatant and the intrinsic tendency of microalgae debris to precipitate by their own. Finally, even after centrifugation it was not possible to detect any plasmon absorbance in the UV-Vis spectrum due the massive presence of microalga debris even after centrifugation.

Considering the centrifugation as an effective method to enhance colloidal stability, all the following synthesis were performed including that purification step. Finally, in order to assess the size of Ag nanoparticles, TEM analyses were performed on freshly prepared samples synthesised with each temperature condition explored in this work ("Ag BIO 3.13 100 °C-C" and "Ag BIO 3.14 RT-C") and the results are reported in the following **Figures 5.1.2 II** and **III**.

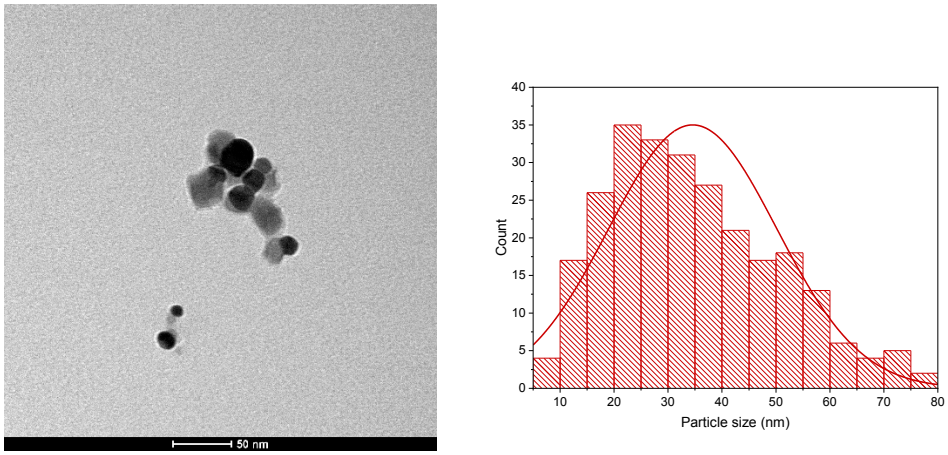

Figure 5.1.2 II *TEM results of sample "Ag BIO 3.13 100 °C-C TEM"*

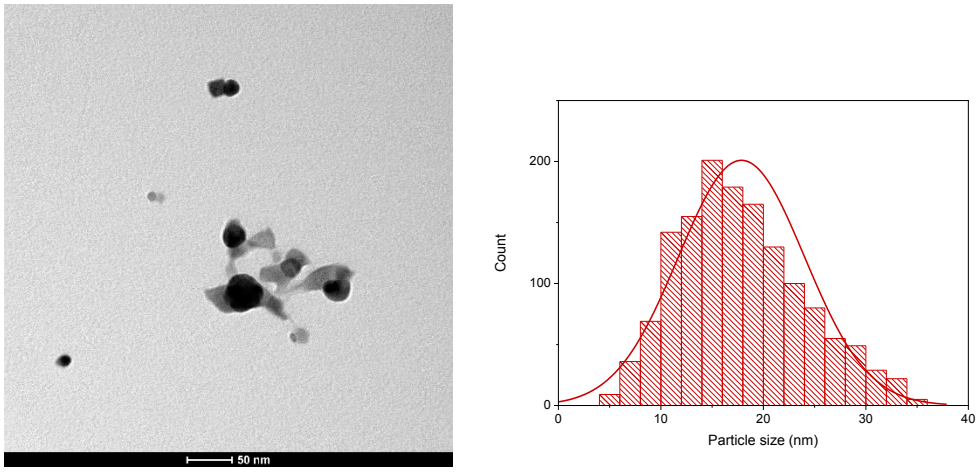

Figure 5.1.2 III TEM *results of sample "Ag BIO 3.14 RT-C TEM"*

In the images, the presence of spherical (black) particles is shown: this could be probably ascribable to the formation of Ag nanoparticle, even if there is not an observable plasmon absorbance. As can be noticed there is not the presence of any aggregates (differently from the synthesised batch standards, **Figures 5.1.2 VI** and **VII**). This could be explained with the fact that the samples were freshly prepared and analysed in the following 2 hours. The particles diameter was measured for both samples, resulting in 18±6 nm (PDI 0.3) for Ag BIO 3.1 RT-C and in 35±16

nm (PDI 0.5) for Ag BIO 3.0 100 °C-C. Besides, the measured particle diameters unravel a particular feature, already suggested by DLS (samples "Ag gaditana BIO 3.0 100 °C-C" and "Ag gaditana BIO 3.1 RT-C"): syntheses at room temperature generated smaller and more monodispersed nanoparticles (18 nm, PDI 0.3, average polydisperse) compared to the ones obtained through heating (35 nm, PDI 0.5, average polydisperse). The result definitively confirmed that the usage of lower temperature leads to better particles (in both terms of size and polydispersity) with lower energetic expenditures in favour to sustainability. Finally, the microscopic analysis confirmed that the DLS measurements were overestimated due to the presence of biogenic debris adsorbed on the particles. Even for these samples it was not possible to observe the silver plasmon through UV-Vis analysis. The following **Figure 5.1.2 IV** reports the spectrum of the extract taken from the centrifugation supernatant used as blank.

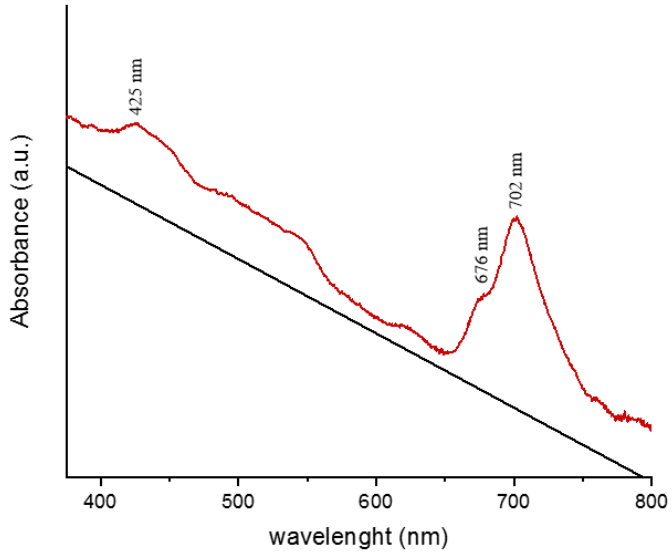

Figure 5.1.2 IV *Absorbance spectrum of the biogenic extract supernatant (red) and its scattering contribution (black)*

As can be highlighted, there is a significant contribution of scattering due to the presence of big particles, ascribed to the biogenic agent (highlighted by the black line [190]). It is possible to observe absorption peaks at 425, 676 and 702 nm which belongs to the Soret (425 nm) and Q bands (676 and 702 nm) of chlorophyll A [191], which is abundant in N. gaditana [110]. The presence of these compounds might explain the particular coloration of these sols.

Then, in order to further purify the samples, a filtration on PTFE filters was carried out (pore diameter of 0.2 μm). The samples were renamed as "Ag BIO 3.17 100 °C-CF" and "Ag BIO 3.18 RT-CF". A UV-Vis analyses was then repeated, by obtaining a broad band at 412 nm, ascribable to the silver plasmon resonance, as reported in **Figure 5.1.2 V**.

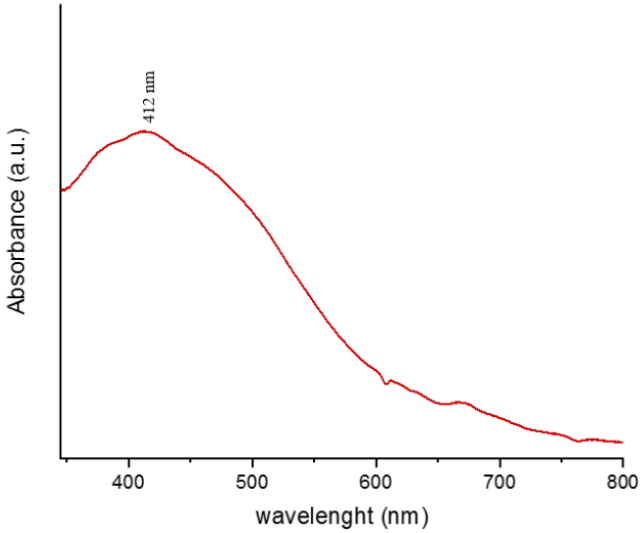

***Figure 5.1.2 V** UV-Vis of sample "Ag BIO 3.18 RT-CF"*

As can be noticed, a plasmon resonance is present, confirming the presence of silver nanoparticles. Nonetheless, due to instrumental noise and to the residual presence of contamination, it was not possible to fit the spectrum into a proper gaussian function (R-squared: 0.78).

Subsequently, both samples were subjected to a ligand exchange procedure with PMOXA-100-S-S (see **s**ection **7.5.2)** with the aim of removing the last adsorbed biomolecules, displacing them with organic molecules and expelling them from the colloidal dispersion through dialysis. After functionalisation, the sample presented a clear plasmon and the solution turned completely pink (compared to the previous green-pink colour). Moreover, it was possible to fit the spectrum with a gaussian function (R-squared 0.90). Considering the spectrum reported in F**igure 5.1.2 V** and the absence of chlorophyll peaks in the 650-750 nm region (**Figure 5.1.2 IV**), it is possible to state that the peak at 409 nm was indeed due to the metal nanoparticles only, definitively confirming the synthesis positive outcome. In **Figure 5.1.2 VI** the fitted spectrum, after functionalisation, is reported.

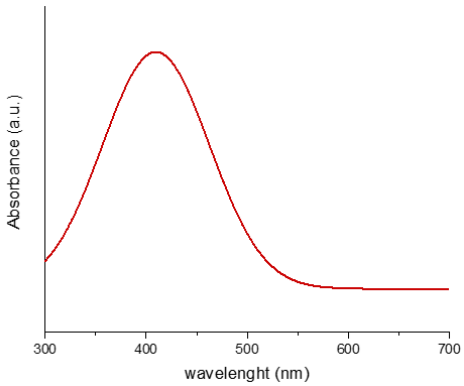

***Figure 5.1.2 VI** Spectrum of sample "Ag BIO 3.17 100 °C-CF" after functionalisation with PMOXA-100-S-S.*

The previous plots definitively confirm the synthesis success. Regarding that, the absorption peak of the polymer in water is at 327 nm, which is distant enough and not influence significantly the plasmon spectrum.

Even if the TEM data were obtained from samples which were not subjected to any purification steps besides centrifugation, these measurements can be assumed to be referable also to the other samples. This feature is ascribed to the image processing analysis performed in which only the diameters of darker metal nanoparticles were considered without the semi-transparent organic corona, which was removed through purification step in other samples.

In conclusion, biogenic metallic silver nanoparticles were successfully synthesised, at least for samples produced at room temperature. These ones showed the same PDI (0.3) of their batch counterpart ("Ag Reverse 2 min") and as well as similar dimensions (20 nm against the 18 nm of the chemical approach). Even though further purification steps are required, the reduced energy consumption and the cost-effectiveness of the reactants might justify the production process. These considerations imply that biogenic silver nanoparticles produced in this thesis may be a valuable economic asset for industries for diminishing the price and the environmental impact of an already widely commercialised nanosystem [63].

5.3. PMOXA synthesis and particle functionalisation

In order to obtain stable suspensions from biogenic Ag and ZnO particles, the functionalisation with) PMOXA ligands was carried out. For functionalisation, polymer chains were modified with anchor groups proven to be specific for adsorption upon the inorganic material produced, namely catechol and disulphide, for ZnO and Ag respectively [20,21]. PMOXAs were synthetised with two different DPs, ∼50 and ∼100. After several modifications of the chain terminator, the organic compounds were used as ligands for the particles of ZnO and Ag. In particular, for Ag the polymer with a length of 100 units was exploited whereas for ZnO PMOXAs with both lengths were used. Beside the simple colloidal stabilisation, on objective of the thesis was to establish whether biogenic particles could be functionalised or not. As shown in previous chapters (sections **5.1.2** and **5.2.2**) both biogenic particles of Ag and ZnO presented a variable amount of microalgae debris adsorbed upon, which may contain strongly binding compound such as flavonoids (which are polyphenols, secondary metabolites used as glues [97,192]).

The polymerisation of PMOXA (like the other polyoxazolines) follows the cationic ring opening polymerisation (CROP) mechanism [116] (see **figure 5.3 I)**. The general mechanisms for the initiation and propagation of 2-oxazolines depends on

the nature of the initiator used in the reaction. Two different types, ionic and covalent, are involved in the reaction. In this case an alkyl tosylate [193]) was used, therefore the covalent mechanism was exploited. Once activated, the cationic polymerization of 2-oxazolines begins with the nucleophilic attack of a nitrogen atom of 2-oxazoline onto the C(5) carbon of the propagating 2-oxazolinium species, resulting in 0(1)-C(5) bond cleavage and isomerization of the intermediate species to give a product with N-acylethylenimine units [194]. In this thesis, after polymerization completion, a terminating agent was added (a nucleophilic amine) [195]. In particular, for this thesis a polymerisation terminator with a hydrolysable ester group was chosen (ethyl isonipecotate). Once deprotected, the carboxylic acid can be exploited to couple functional groups through a stable amide bond [196,197]. In particular, DCC (N,N′-dicyclohexylcarbodiimide), NHS (N-Hydroxysucinimide), COMU ((1-Cyano-2-ethoxy-2-oxoethylidenaminooxy)dimethylamino-morpholino-carbenium hexafluorophosphate) and HBTU (N,N′,N′-Tetramethyl-O-(1H-benzotriazol-1-yl)uronium hexafluorophosphate (HBTU) were used, in different reactions, to activate the terminator carboxylic moiety to react with amines .

The polymerisation mechanism is reported in the following **Figure 5.3 I.** The graph was drawn with the compounds used for this thesis, based on a reference [116].

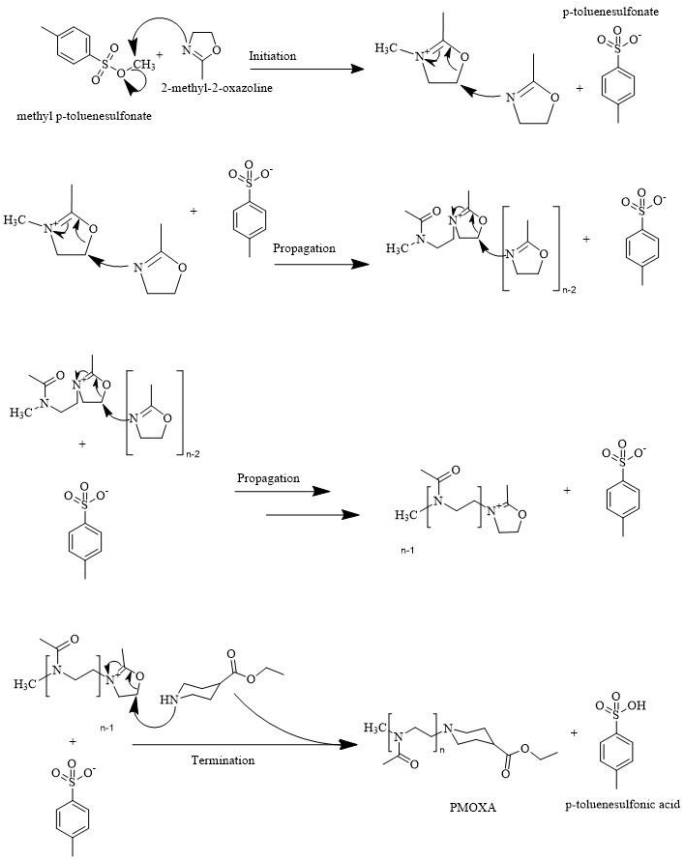

Figure 5.3 I *PMOXA CROP mechanism*

After polymers synthesis and modification, they were used as ligand for previously synthesised nanoparticles. The obtained colloids were monitored for signs of precipitation over time to confirm sols stability.

5.3.1. PMOXA-COOEt polymerisation

The polymerisation reaction process was conducted based on a previous work of Morgese et al. [120] and in **Figure 5.3.1 I** the process (reported in detail in the "**experimental procedures**" chapter, section **7.4.1**.) is shown.

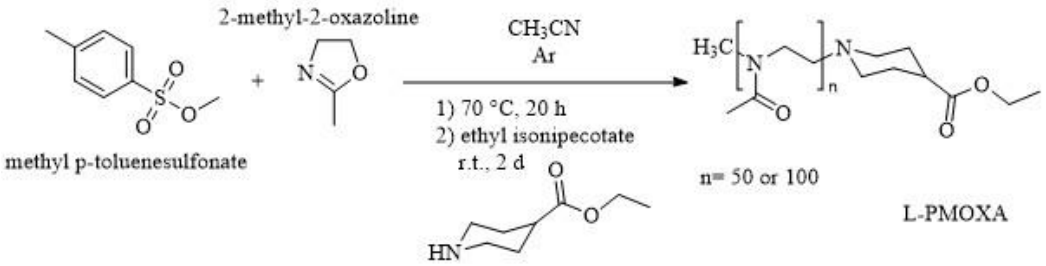

Figure 5.3.1 I *Scheme of the syntheses performed for PMOXAs polymerisation*

As can been noticed in the figure, the same method was exploited to produce both PMOXA-50-COOEt and PMOXA-100-COOET by using, respectively, an initiator to monomer molar ratio of 1:50 and 1:100.

To confirm the positive synthesis outcome, ^{1}H NMR analysis was performed on both products. The relative spectra are shown in **Figures 5.3.1 I** and **II**.

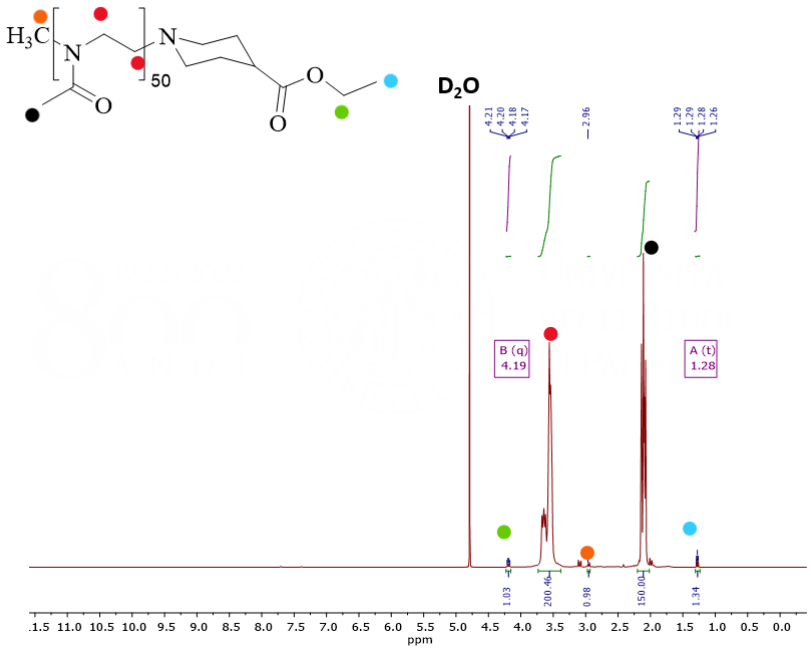

Figure 5.3.1 I *^{1}H NMR spectrum of PMOXA-50-COOEt in D_2O*

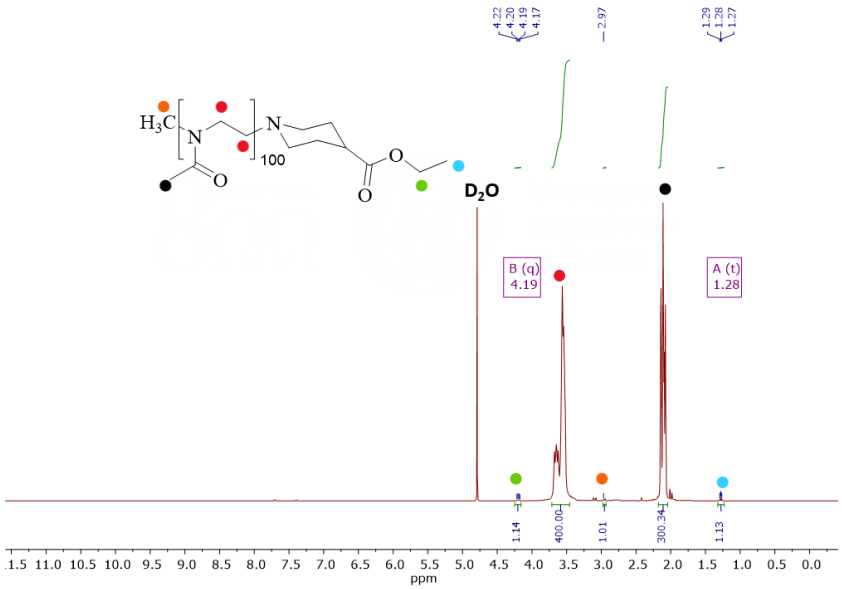

Figure 5.3.1 II *^{1}H NMR spectrum of PMOXA-100-COOEt in D_2O*

The peaks assignment was performed comparing the spectra to references reported in literature [120,198] and through J-coupling analysis (for protons belonging to the ethyl isonipecotate esters). As for all the ^{1}H NMR measurements performed in this thesis, it was not possible to identify protons signals from the piperidinic ring, being likely covered by protons belonging to the repeating units [199]. Furthermore, the integrals of the signals related to the protons from the terminator ethyl-ester (-CH_2- and -CH_3) and the initiator (-CH_3) do not correspond to the expected values (3, 2 and 3 respectively). This is due to the signal ratio between the repeating units and the un-repeated parts which makes the latter ones difficult to be detected. Nonetheless, the degree of polymerisation (DP, corresponding to the number of repeating units in the polymer [200]) was estimated for both polymers, from the integral ratio between protons of the repeating units and the terminator ester. In the **table 5.3.1 III** the calculated values are reported.

Polymer	Terminator ester CH_3 with oxazoline CH_3	Terminator ester CH_3 with oxazoline CH_2-CH_2	Terminator ester CH_2 with oxazoline CH_3	Terminator ester CH_2 with oxazoline CH_2-CH_2
PMOXA-50-COOEt	113	115	94	95
PMOXA-100-COOEt	270	272	178	180

Table 5.3.1 III *DP (adimensional) calculated from NMR spectra of PMOXA-50-COOEt and PMOXA-100-COOEt*

None of the calculated DPs correspond to the expected values (50 and 100). The causes are either the incomplete termination with ethyl isonipecotate (of all chains) or ester hydrolysation during work up steps. In any case, considering the correct molar ratios of initiator to monomer, it is safe to assume the chains length obtained are the ones wanted. As last consideration, even though NMR analysis did confirm the polymers syntheses, an analytical gel permeation chromatography run (GPC) should be performed in the future to confirm the DPs and calculate the PDIs [201].

5.3.2. PMOXA-COOH synthesis

Following a method previously from Trachsel et al. [198], the ethyl isonipecotate terminating esters, of the previously obtained PMOXAs, were hydrolysed obtaining the corresponding carboxylic acids.

The reaction scheme is shown in the following **Figure 5.3.2 I**.

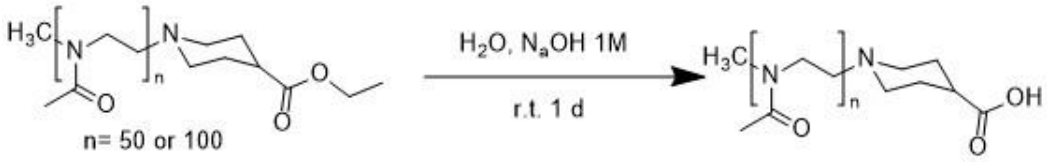

Figure 5.3.2 I *Scheme of the syntheses performed for ester hydrolysis*

Once the chains were polymerisated and terminated, the carboxylic acid cannot react with active MOXA moieties (generating chain cross-links [202]), meaning that the ethyl ester can be hydrolysed for further reactions. The process was performed for both polymers. The polymers NMR spectra are reported in the following **Figures 5.3.2 II** and **5.3.2 III**.

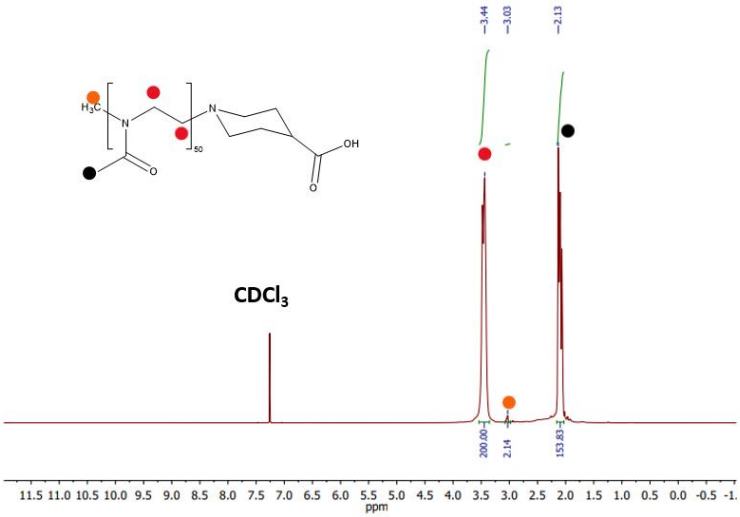

Figure 5.3.2 II *PMOXA-50-COOH ^{1}H NMR spectrum*

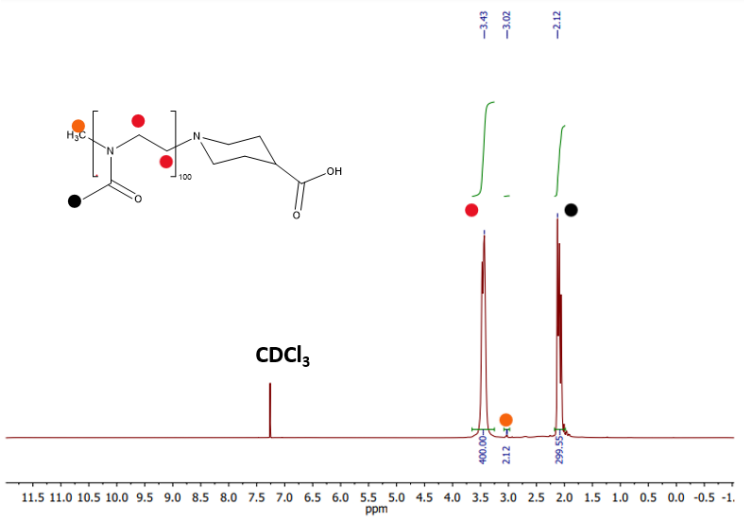

Figure 5.3.2 III *PMOXA-100-COOH ^{1}H NMR spectrum*

As can be easily interpreted from the spectra, there is not the presence of esters protons, indicating the protecting group was successfully removed and confirming the reaction success. After these procedures, the batches of both polymers were split to form PMOXA-ND and PMOXA-S-S.

5.3.3. PMOXA-ND synthesis

Before coupling with a molecule containing the catechol group, the latter one was nitrated. As it is known in literature, the $-NO_2$, being an electron withdrawing group, reduces the pK_a of the catechol ring it is bound to (from 9 to around 6.5). Thus it facilitates deprotonation and allows for stronger interactions with metal oxides [120]. In this case, the dopamine molecule was nitrated and used as a catechol bearing compound (obtaining 6-nitrodopmaine (ND)). The anchor group choice is dictated by the high biocompatibility of the molecule, being a natural neurotransmitter in the stimulus-rewarding circuit [203] and by the fact that catechol strongly bound to oxide surfaces [21]. The reaction performed (following the protocol of Morgese et al. [120]) is a classical electrophilic aromatic nitration [204] and the experimental conditions exploited are schematised in **Figure 5.3.3 I**.

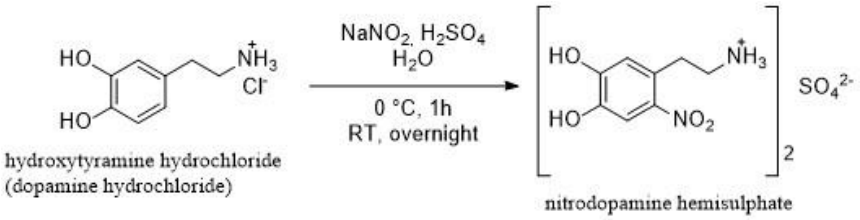

Figure 5.3.3 I *Dopamine nitration reaction*

The process produced a brown powder with a reaction yield of 19 %. The ^{1}H NMR, as well as the ESI-MS analyses, were performed in order to confirm the reaction success. The spectra are reported in **Figures 5.3.3 II** and **III**.

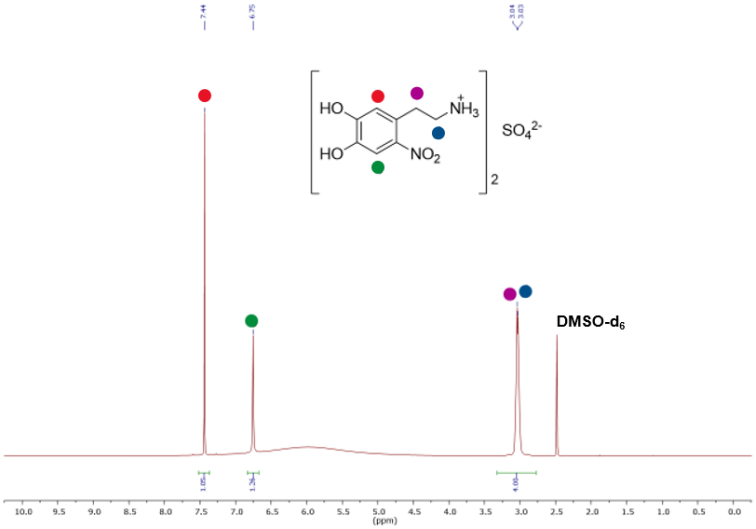

Figure 5.3.3 II *^{1}H NMR of nitrodopamine hemisulphate*

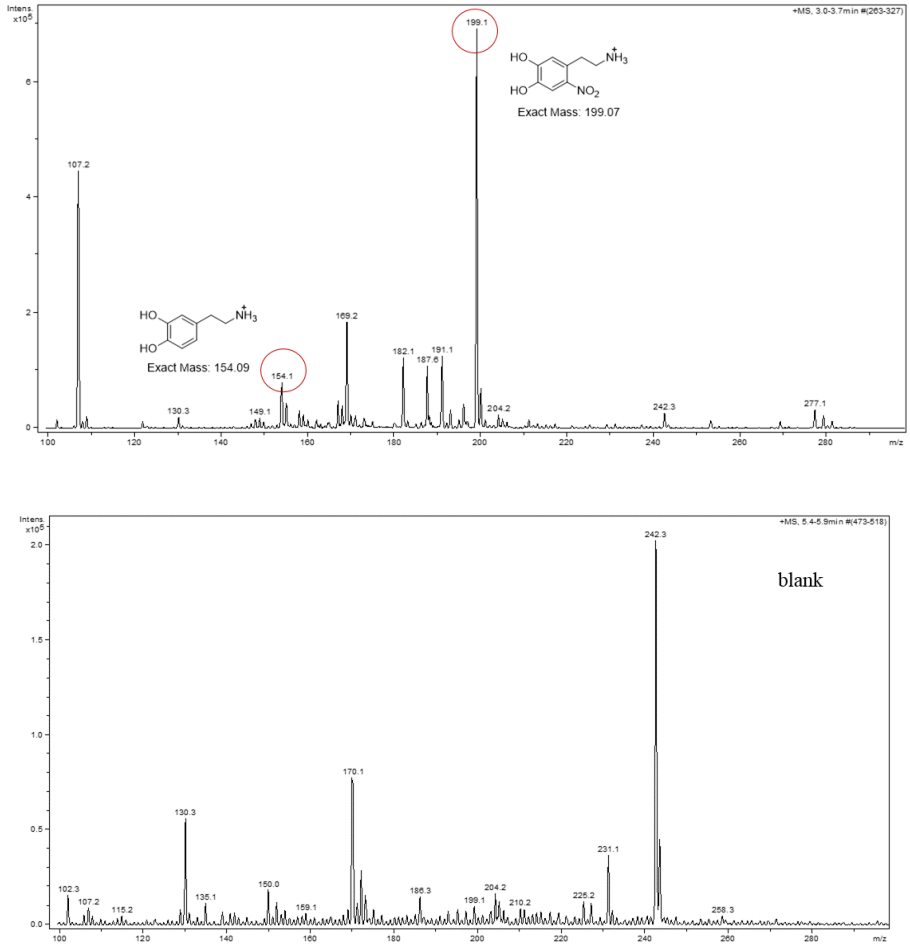

Figure 5.3.3 III *ESI-MS spectrum of nitrodopamine hemisulphate. On top, the sample spectrum is shown (dopamine compounds are highlighted in red circles); whereas at the bottom the blank exploited is reported*

The peak assignment of ^{1}H NMR was performed by comparison with a reference [120] and it confirms the reaction success. The ESI-MS analysis assessed the sufficient purity of the product (high intensity signal at 199.1 m/z, highlighted in a red circle in **Figure 5.3.3 III**). By comparison with the blank spectrum, it is noticeable that most of the impurity signals detected in the sample spectrum (such as 107.2, 130.3, 149.1, 169.2 and 204.2 m/z) are actually ascribed to residual contaminations already present in the instrument. However, there is still a small presence of the reactant (154.1 m/z, highlighted in a red circle in **Figure 5.3.3 III**) meaning it did not react completely, as suggested by the low reaction yield. Nonetheless, the impurities were likely removed with further dialysis steps (once the coupling reaction was performed) and the presence of unreacted dopamine molecules might have only generated a small polymers population without a strong bond with ZnO which, again, were probably removed in the last dialysis step.

Once obtained the 6-nitrodopamine, it was linked to both PMOXA-50-COOH and PMOXA-100-COOH using the DCC/NHS chemistry to form an amide bond [120].

The DCC is a carboxylic acid activator, meaning that by linking itself to carbonylic carbon, it enhances the susceptibility of the latter to be subjected to a nucleophilic attack. The reaction mechanism is shown in **Figure 5.3.3 V** [205].

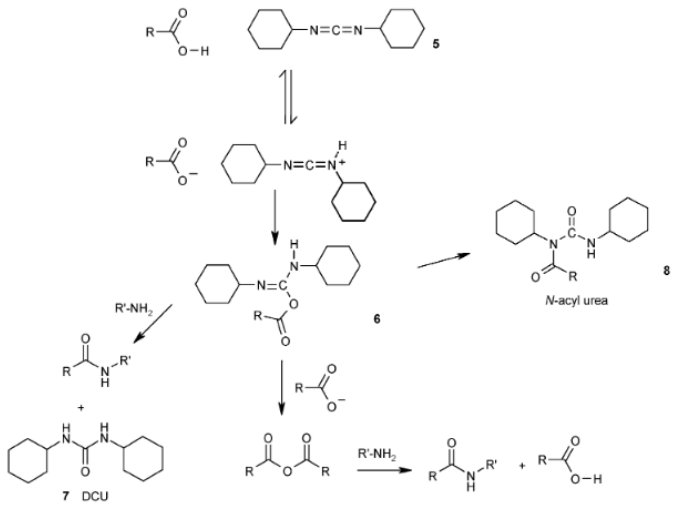

***Figure 5.3.3 V** Reaction mechanism of DCC [205]*

As shown in the picture, after coupling to an amine (or another group such as an alcohol), an N,N-dicyclohexylurea (DCU) molecule is released as a side product (insoluble in most solvents [206]). Moreover NHS is often used with DCC to form a more stable, yet activated, intermediate (through an ester bond) which may be purified (in this case by precipitation) before continuing the coupling process [207]. Moreover, an NHS-ester is particularly reactive towards amines [208,209]. In **Figure 5.3.3 VI** the amide formation from an NHS-ester is briefly reported, for clarity [208].

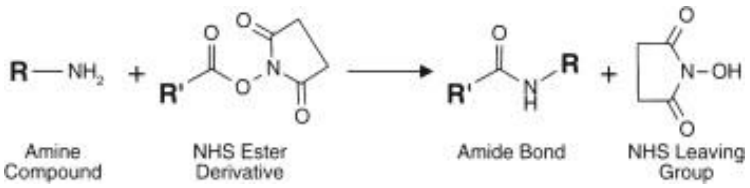

Figure 5.3.3 VI *Formation of an amide from a NHS-ester [208]*

For the synthesis, a molar ratio of 1:10:10 (polymers : DCC : NHS) was used in the first reaction step (generation of PMOXA-NHSs). After that, the formation of PMOXA-NDs was performed with a molar ratio of 1:1.18:1.18 (polymer : ND : TEA). The reaction scheme utilised is summarised in **Figure 5.3.3 IV.**

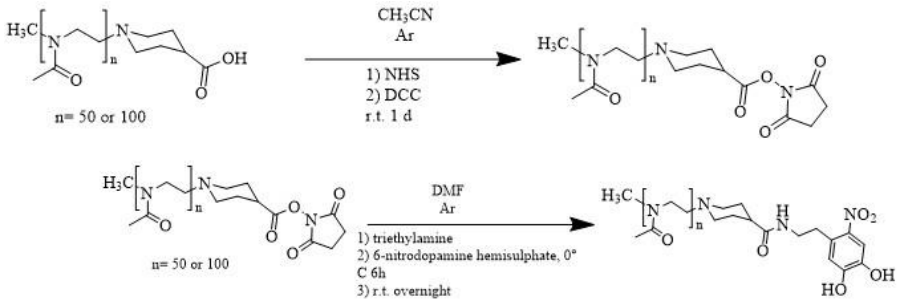

Figure 5.3.3 IV *Scheme of the coupling PMOXA-COOH with nitrodopamine*

To establish the synthesis effectiveness, ^{1}H NMR analyses were performed and the retrieved spectra are shown in **Figures 5.3.3 VII** and **VIII**.

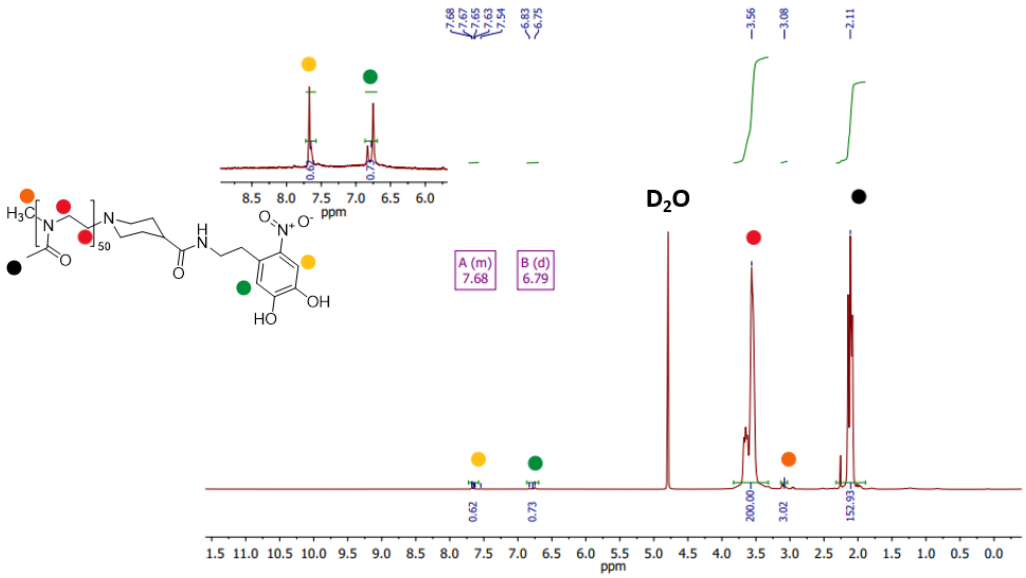

Figure 5.3.3 VII *^{1}H NMR of PMOXA-50-ND. In the left panel, the protons belonging to the aromatic ring are highlighted along with their multiplicity*

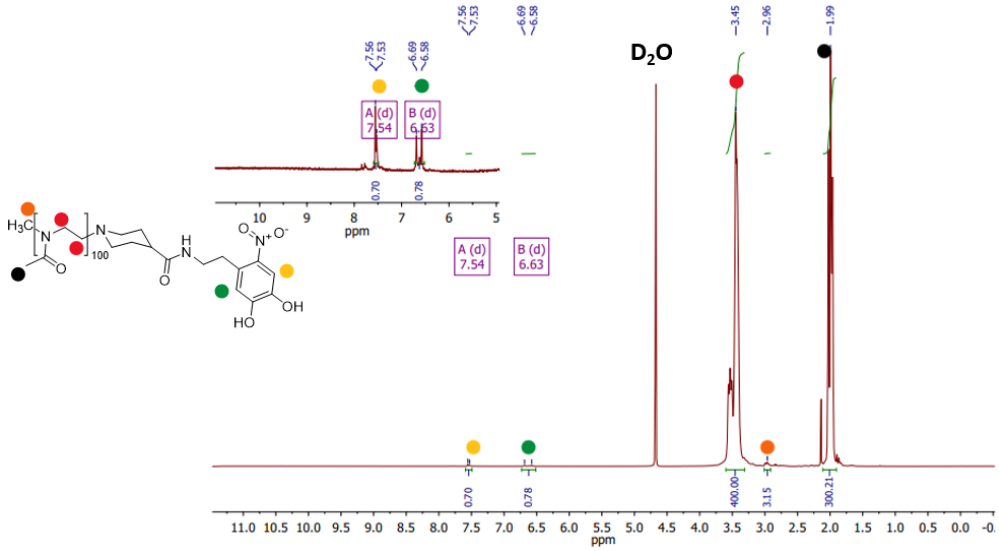

Figure 5.3.3 VIII *^{1}H NMR of PMOXA-100-ND. In the left panel, the protons belonging to the aromatic ring are highlighted along with their multiplicity*

Based on the reference used [120], it was possible to determine the synthesis success. Nonetheless, it is worth noticing that the protons signals corresponding to the ND aromatic rings are spitted into doublets (highlighted in the top-left mini-spectra in **Figures 5.3.3 VII** and **VIII)**. Rather than J-coupling, the cause of these double signals is, realistically, the presence of two polymer populations: one with an amide bond (between the polymer and amine group of ND) and another one with an ester bond (between the macromolecule and the catechol group of ND). Nitrating the dopamine diminished the pKa value of the compound, this entails that (being deprotonated) the alkoxy groups of catechol may react with the NHS-ester forming another ester with themselves. For that reason, it was not possible to determine the reaction conversion (by comparing the integers of protons from ND and the repeating units). However, the ester-bound polymers were lost during the last dialysis work up step after particle functionalisation (as non-ligands), as adsorption through the catechol group is sterically hindered for them. Differently from other synthesised polymers, the obtained powders were brown instead of bright white, due to the ND group attached (having that colour by itself).

5.3.4. PMOXA-S-S synthesis

In order to graft PMOXA polymers onto AgNPs, the PMOXA-100-COOH was linked to a lipoic acid molecule. The latter contains the disulphide group (S-S) which is proven to bind silver surfaces with high affinity (being a double thiol) [20]. Moreover, lipoic acid is known for its biocompatibility being a human endogenous molecule [128,210]. However, this time, in order to link an acidic compound (PMOXA-100-COOH) to another one (lipoic acid), a linker molecule was required. For that purpose, p-xylylenediamine was exploited. This compound was chosen for

being a molecule with two amine moieties (which can form the same number of amide bonds) and an aromatic ring (easily detectable by ^{1}H NMR).

In this synthesis, COMU was used as an activating agent for the carboxylic acid. This one is a uronium type-coupling agent containing an Oxyma moiety (ethyl 2-hydroximino-2-cyanoacetate), a common coupling additive in peptide synthesis [211,212]. The proposed reaction coupling mechanism for amide formation is reported in **Figure 5.3.4 I** [213].

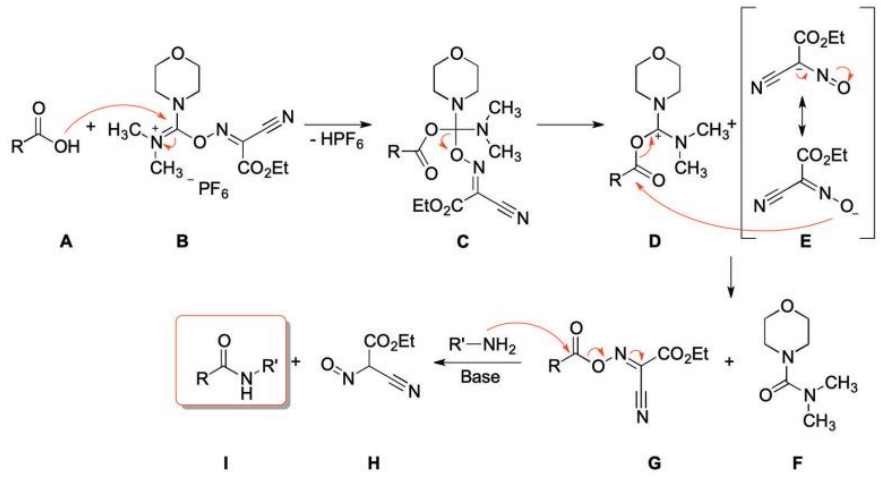

Figure 5.3.4 I *Proposed mechanism for COMU coupling. In particular the molecule A is a generic carboxylic acid, B is COMU, F is the uridinic by-product whereas H is the oxyminic one*

For this synthesis, a molar ratio 1:5:10:10 (polymer : p-xylylenediamine : COMU : DIPEA) was chosen. The reaction performed is briefly summarised in **Figure 5.3.4 II**.

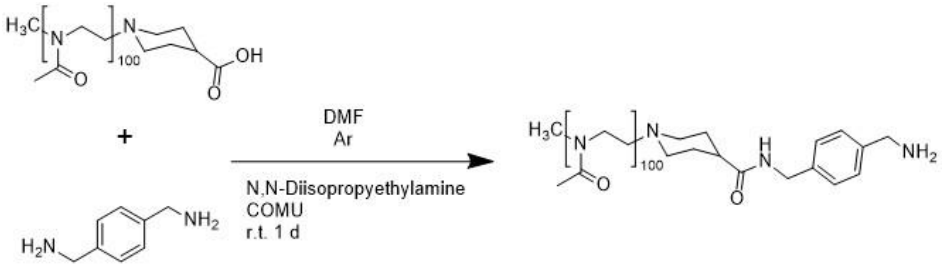

Figure 5.3.4 II *Coupling reaction between PMOXA-100-COOH and p-xylylenediamine*

The synthesis success was confirmed by ^{1}H NMR analysis, see spectrum in **Figure 5.3.4 III**.

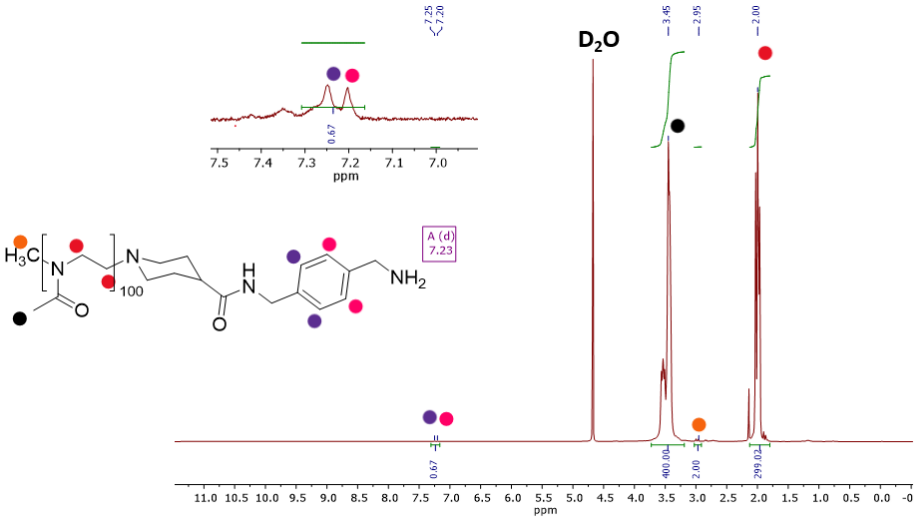

Figure 5.3.4 III *NMR spectrum of PMOXA-100-NH_2. On top-left, the zoom-in of the aromatic ring protons is reported*

Proton assignments were performed based on previous polymer spectra and, in absence of suitable literature references, on a MestReNova prediction (software version: 12-0-0), for signals belonging to the aromatic ring. By comparison of integers from the aromatic ring and the repeating units of the polymer, a conversion of 15 % was calculated. Being considered an excessively low value for an effective particle functionalisation, the same batch was subjected to another coupling reaction with a different activating agent.

For this reaction the coupling agent chosen was HBTU. This one is a well renowned amide forming compound for peptide synthesis, being part of the uronium class coupling reagents [205]. The coupling mechanism (for peptide synthesis, yet it is the same for any amide formation) is shown in the following **Figure 5.3.4 IV**, (retrieved from the book "Oxytocin" by Thomas Kremsmayr & Markus Muttenthaler [214]).

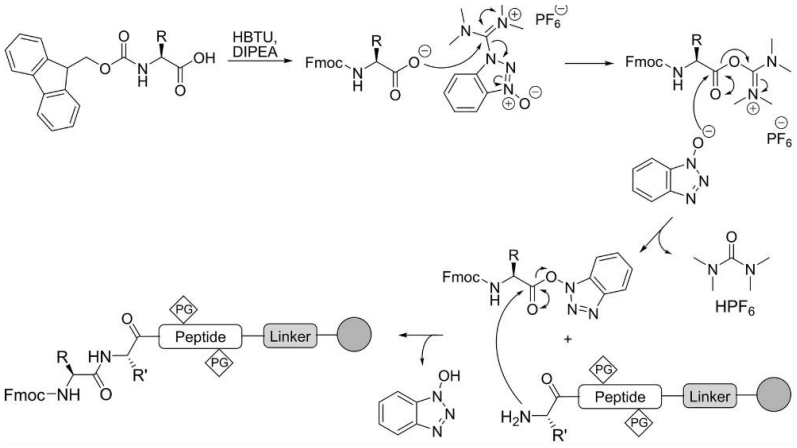

Figure 5.3.4 IV *HBTU reaction mechanism in a peptide synthesis*

The molar ratio used was 1:1.2:8:8 (polymer : HBTU : p-xylylenediamine : TEA) This reaction scheme for this new coupling is shown in the following **Figure 5.3.4 V**.

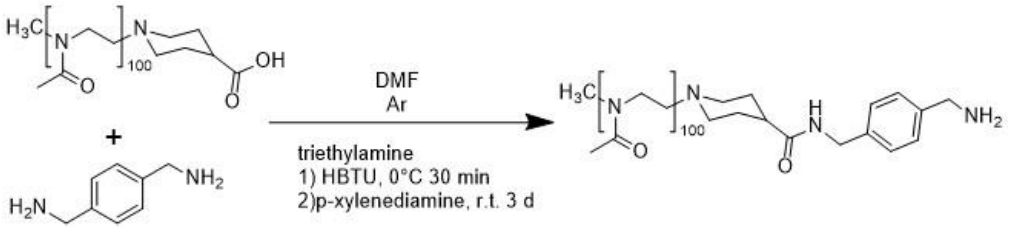

***Figure 5.3.4 V S**econd coupling reaction between PMOXA-100-COOH and p-xylylenediamine*

To evaluate the conversion and general synthesis success, an ^{1}H NMR analysis was performed (**Figure 5.3.4 VI**).

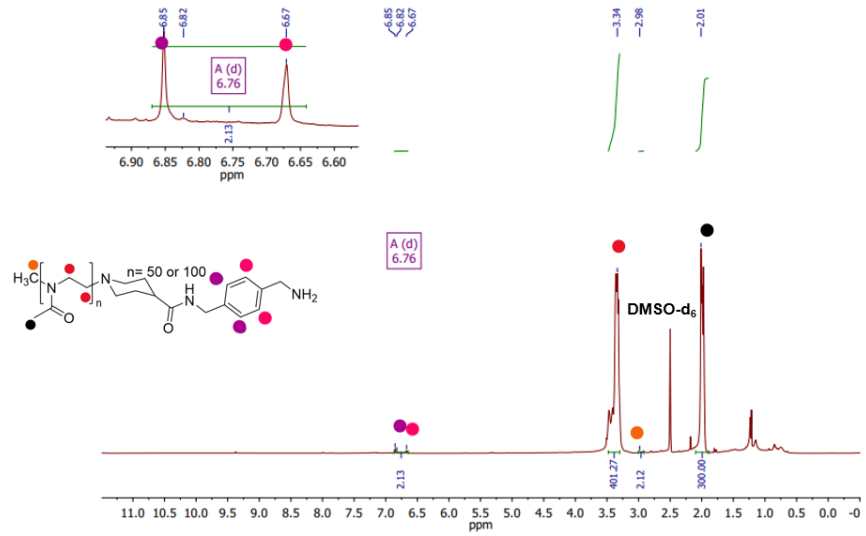

***Figure 5.3.4 VI** ^{1}H NMR spectrum of the second amine coupling reaction*

Adding this reaction step, a conversion of 53% was reached, which is deemed as more than enough to continue with coupling steps. However, at very low chemical shifts (below 1.25 ppm), the presence of contamination is noticeable. Nonetheless, any component which was not properly adsorbed onto silver particles was lost during the various dialysis step, such as these impurities.

As last step, lipoic acid was linked to the p-xylylenediamine linker moiety, to complete the particle anchor attachment. For this last organic synthesis, a molar ratio of 1:5:6:20 (polymer : lipoic acid : HBTU : TEA) was chosen. In the next **Figure 5.3.4 VII** the reaction scheme is reported.

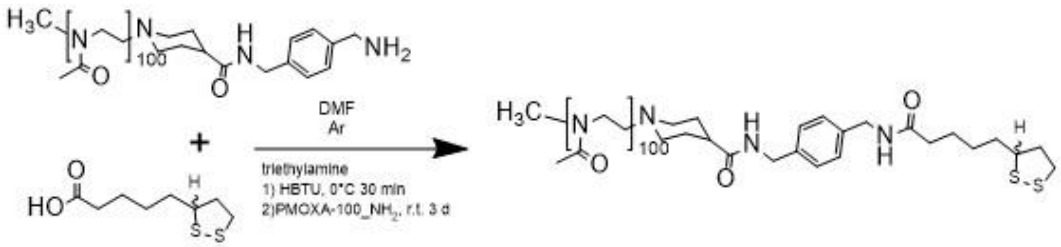

Figure 5.3.4 VII *Lipoic acid coupling reaction*

As can be noticed in the picture, the acid used was a raceme, yet only the enantiomer R of alpha-lipoic acid is naturally produced by organisms. However, the raceme is a cheaper and biocompatible option, being is widely used in dietary supplements and may enhance the therapeutic action of the standalone biologic isomer [125,127]. Contrarily to previous organic syntheses, for this reaction it was not possible to evaluate the product with ^{1}H NMR since the protons of lipoic acid present a chemical shift similar to the repeating units of the polymer [126]. Nevertheless, the small organic molecule at issue shows a peculiar absorbance peak in UV-Vis spectroscopy near 330 nm [215]. For that reason, the characterisation was made by comparison of a 1 mg/ml standard lipoic acid solution (in DMF) with another one of the polymer (PMOXA-100-S-S, 2 mg/ml). The spectra are reported in **Figure 5.3.4 VIII.**

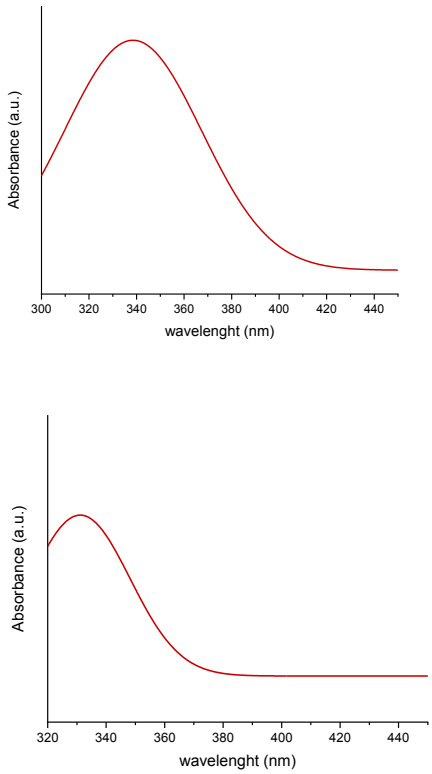

Figure 5.3.4 VIII *UV-Vis spectra of the standard solution of lipoic acid (top) PMOXA-100-S-S bottom) in DMF*

The two spectra shown present similar absorption maxima, being 338 nm for lipoic acid alone and 331 nm for PMOXA-100-S-S. The spectra similarity confirmed the coupling success. The concentration of the polymer solution was chosen in order to have a good enough signal to noise ratio. Nonetheless, due to probably sample polydispersity altering the real value of molar concentration, it was not possible to estimate the conversion.

5.3.5. Particles functionalisation

Once obtained the final polymers (PMOXA-50-ND, PMOXA-100-ND and PMOXA-100-S-S), they were mixed with a dispersion of ZnO and Ag particles obtaining a hybrid material sol. The colloidal stability was then evaluated on a weekly basis three times.

5.3.5.1. ZnO@PMOXA particles

ZnO particle were functionalised with polymers based on the weight ratio optimised by Morgese et al. [120]. The ratios were adapted based on the particle sizes of synthetised systems. However, polymer quantities were chosen based on the diameter instead of the surface area. Furthermore, for hydrothermally synthetised particles, an even smaller amount of PMOXA was added (compared to diameter requirement). This non optimal surface derivatisation was dictated by PMOXA-NDs stock availability. The weight ratio used, the quantities of polymer and ZnO and the overall ZnO@PMOXA retrieved, are summarised in **Table 5.3.5.1 I**.

ZnO sample	Polymer used	Polymer (mg)	ZnO (mg)	Weight ratio (ZnO/polymer)	Obtained mass ZnO@PMOXA (g)
Zno 0.3	PMOXA-100-ND	20	10	1:2	22
ZnO 1.7	PMOXA-100-ND	250	10	1:25	128
ZnO 2.2	PMOXA-100-ND	150	10	1:15	100
Zno 0.3	PMOXA-50-ND	20	10	1:2	26
ZnO 1.7	PMOXA-50-ND	150	10	1:15	15
ZnO 2.2	PMOXA-50-ND	150	10	1:15	47

Table 5.3.5.1 I *Synoptic table of ZnO functionalisation*

As can be extrapolated from the previous table, a recognisable general trend is the obtainment of lower amount of ZnO@PMOXA for the PMOXA-50-ND polymer functionalisations. Even though it may seem that PMOXA-100-ND is more adsorbed onto particles, the product retrieving process is a delicate step. Therefore, from this data it is not possible to assess if one polymer performed better than the other one.

To confirm adsorption, DLS size measurements were performed and compared to TEM measured diameter of particles. In the following **Table 5.3.5.1 II** the resulting DLS "number" data are reported.

sample	ZnO diameter (nm)	ZnO@PMOXA DLS size (nm)
PMOXA-50-ND + ZnO 0.3	60	280
PMOXA-50-ND + ZnO 1.7	1771	989
PMOXA-50-ND + ZnO 2.2	476	582
PMOXA-100-ND + ZnO 0.3	60	277
PMOXA-100-ND + ZnO 1.7	1700	782
PMOXA-100-ND + ZnO 2.2	476	650

Table 5.3.5.1 II *Synoptic table of ZnO@PMOXA DLS size*

As can be noticed by the previous table, for small nanoparticles produced by batch, the functionalisation occurrence is evident by the large increase in diameter. Moreover, the increase of size was similar for both polymers, this may be explained with chain coil phenomena due to the length of the molecule itself. However, for other samples, the increase is not significant. Furthermore, for "ZnO 1.7" (hydrothermal synthesis) a reduction in size is detected. The reason for these wrong data is ascribed to instrument upper detection limit for unusually big particles. Nevertheless, for these four samples, the functionalisation was indeed confirmed with an ATR-IR analysis, and spectra are shown in **Figure 5.3.5.1 III**.

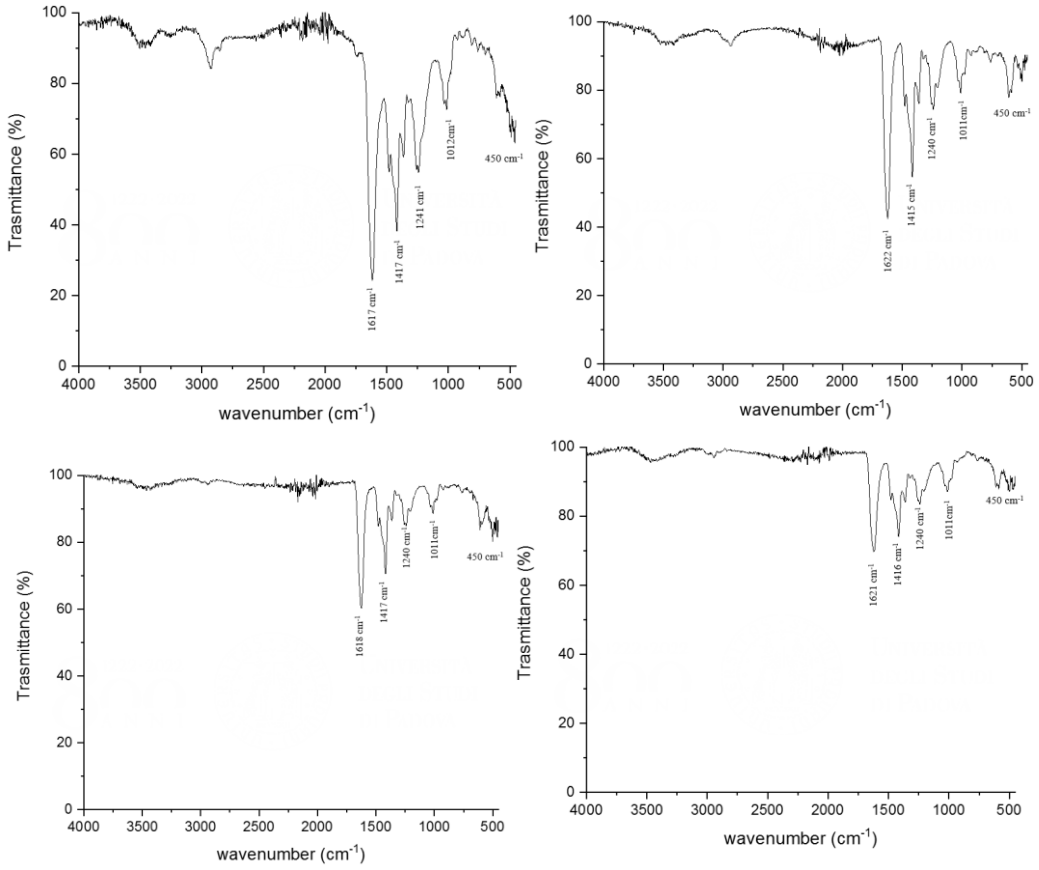

Figure 5.3.5.1 III *ATR-IR spectra of ZnO@PMOXA: on top the spectra of "ZnO 1.7@PMOXA-50" (left) and "ZnO 1.7@PMOXA-100" (right) whereas at the bottow row "ZnO 2.2@PMOXA-50" (left) and "ZnO 2.2@PMOXA-100" (right) are shown*

As can be easily seen in the spectra, the polymer is present in all samples (comparison from reference [120]). In particular, organic peaks are even qualitatively more intense with respect to the Zn-O signal near 450 cm^{-1} [150]. In details, peaks at 1620 cm^{-1} are ascribed to the C=C aromatic stretching mode (of 6-nitrodopamine) [216]. Furthermore, the polymer repeating units generated the signals close to 1420 cm^{-1} (aldehyde C-H bending mode [151]), 1240 cm^{-1} (CH_2/NH_2 twisting vibration [217]) and signals near 1010 cm^{-1} (C-C skeletal stretch [218]). These measurements finally confirmed the adsorption of both polymers on every ZnO particle type used.

Once confirmed the ZnO@PMOXA formation (for every ZnO synthesis with all the PMOXA-ND produced), colloid dispersions were prepared and their stability was monitored through time. In **Figures 5.3.5.1 IV** and **V** photo of samples freshly made and after three weeks, respectively, are reported.

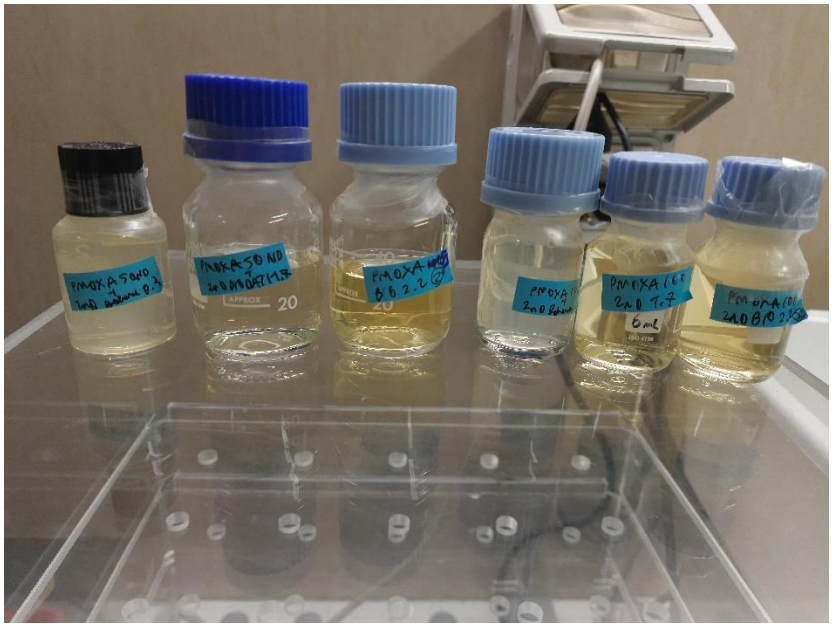

Figure 5.3.5.1 IV *Freshly prepared ZnO@PMOXA colloids. From left to right: "ZnO 0.3@PMOXA-50", "ZnO 1.7@PMOXA-50", "ZnO 2.2@PMOXA-50", "ZnO 0.3@PMOXA-100", "ZnO 1.7@PMOXA-100" and "ZnO 2.2@PMOXA-100"*

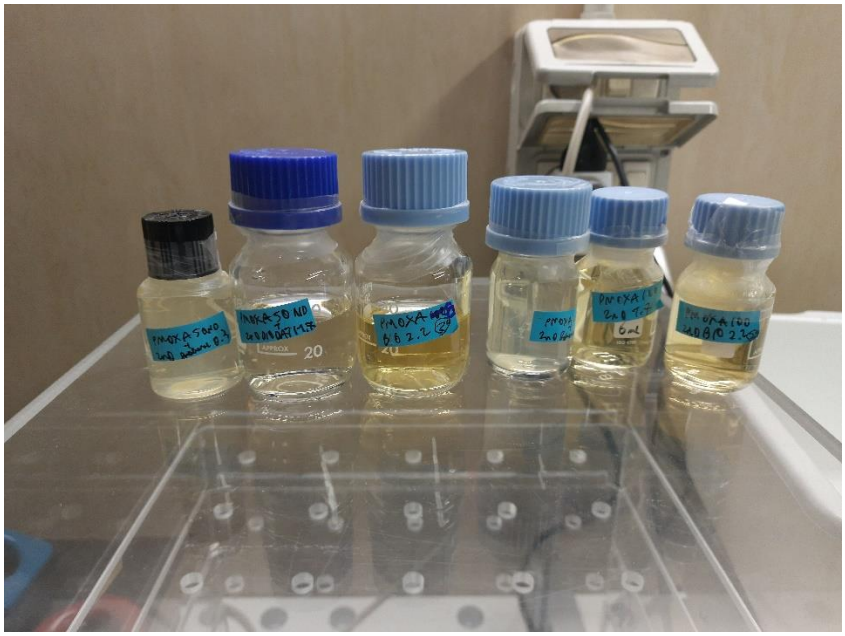

Figure 5.3.5.1 V *ZnO@PMOXA colloids after 3 weeks. From left to right: : "ZnO 0.3@PMOXA-50", "ZnO 1.7@PMOXA-50", "ZnO 2.2@PMOXA-50", "ZnO 0.3@PMOXA-100", "ZnO 1.7@PMOXA-100" and "ZnO 2.2@PMOXA-100"*

During the first week of shelf life, all the colloids obtained presented good stability without showing the presence of any precipitate. Nevertheless, after two weeks, colloids produced by syntheses made with the biogenic and batch methods (independently from the polymer used) presented precipitates indicating the beginning of an aggregation process and stability loss (see **Figure 5.3.5.1 VI**). It is worth noticing that these two types of synthesis are similar in the way they were carried out (ZnO precipitation). This feature suggests that the synthesis procedure

may have influenced the colloidal stability even more than the presence of microalgae (since all the sols at issue started precipitating after the same time). Surprisingly, both "ZnO 1.7@PMOXA50" and "ZnO 1.7@PMOXA100" (produced by the hydrothermal method) remained completely stable after the whole time frame (3 weeks total), even though the particle generated by the hydrothermal method were the biggest and were the ones with a reduced weight ratio (ZnO to polymer) compared to their size (being, supposedly, not completely covered by the macromolecule).

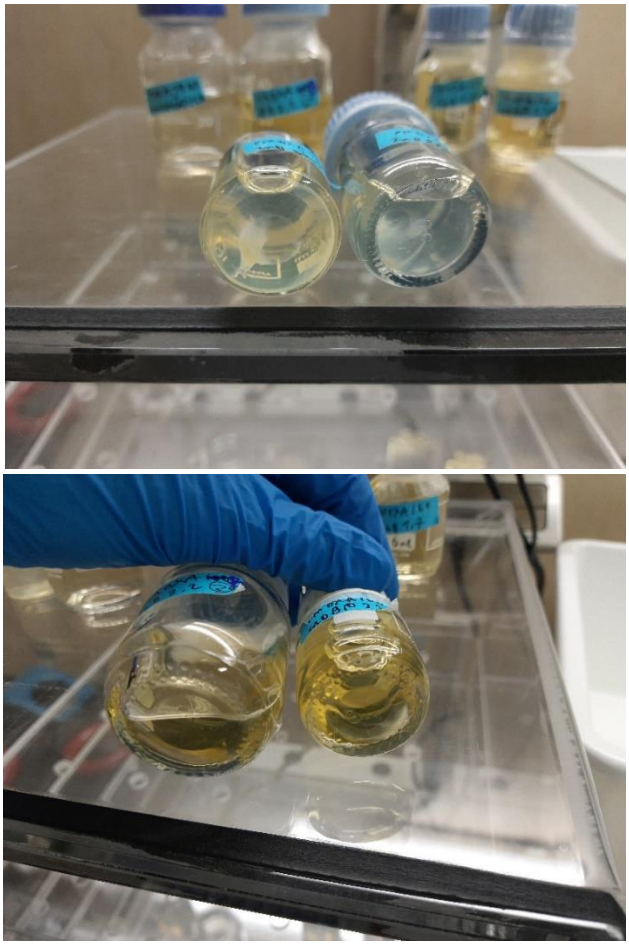

Figure 5.3.5.1 VI *Precipitate after 2 weeks of "ZnO 0.3@PMOXAs" (top) and "ZnO@PMOXAs" (bottom)*

These results determined that the synthesis procedure influence the colloidal stability more than the used precipitating agent (NaOH or microalga) and the polymer length chosen (PMOXA-50-ND or PMOXA-100-ND). Nonetheless, PMOXA-ND did strip microalgae components on the particle surface as confirmed by ATR-IR analysis. In conclusion, biogenic synthesis of ZnO particles did generate a product comparable to the batch counterpart, even from the point of view of colloidal stability. Nonetheless, microalgae may have played a role in stability, even though it was not crucial.

5.3.5.2. Ag@PMOXA particles

AgNPs were functionalised with PMOXA-100-S-S by mixing freshly prepared metal colloids with a polymer solution (see section **7.5.2**). The process outcome was confirmed by comparing the diameter increase through DLS analysis. In T**able 5.3.5.2 I**, the resulting DLS plotted as number data are reported.

sample	Ag diameter (nm)	Ag@PMOXA DLS size (nm)
PMOXA-100-S-S + Ag Turkevich Normal	6.0	54
PMOXA-100-S-S + Ag Turkevich Reverse	20	68
PMOXA-100-S-S + Ag BIO 3.18 RT-CF	18	68

Table 5.3.5.2 I *Synoptic table of Ag@PMOXA DLS size*

As can be easily determined from the previous table, for all samples, the functionalisation process succeeded.

The time resolved colloidal stability was assessed and in **Figures 5.3.5.2 II** and **III** sol photos are reported of Ag@PMOXA samples freshly prepared and after three weeks at room temperature, respectively.

Figure 5.3.5.1 II *Freshly prepared Ag@PMOXA colloids. From left to right: "Ag Turkevich Normale@PMOXA100", "Ag Turkevich Reverse@PMOXA100", "Ag BIO 3.18 RT-CF@PMOXA100"*

Figure 5.3.5.1 III *PMOXA@Ag colloids after three weeks. From left to right: "Ag Turkevich Normale@PMOXA100", "Ag Turkevich Reverse@PMOXA100", "Ag BIO 3.18 RT-CF@PMOXA100"*

Even the PMOXA@Ag colloids did not present any sign of instability after one week of shelf life. Nevertheless, after the second week (out of 3), "Ag BIO 3.18 RT-CF@PMOXA100" presented precipitates indicating the start of an aggregation process (see **Figure 5.3.5.1 IV**). The reason behind this loss colloidal stability may be the synthesis method (since the Turkevich counterparts remained dispersed). Microalgae debris might be still present onto particle surface, event after polymer functionalisation, determining the instability.

Figure 5.3.5.1 IV *Precipitate after 2 weeks of "Ag BIO 3.18 RT-CF@PMOXA100"*

These results determined the inefficiency of biogenic AgNPs in polymer stabilisation compared to their chemical synthesis benchmarks. Nevertheless, the functionalisation did improve drastically the colloidal stability up to two weeks (from the 72 hours previously achieved in this work without the aid of PMOXA). In the future, the use of longer or different polymers may change the outcome. It is worth reminding in this context, the cheaper cost of biogenic syntheses compared to the chemical ones, which may cover the polymer production [105]. Moreover, biogenic Ag might be more biocompatible and efficient as an antimicrobial further justifying the need of research from that point of view [174].

6. CHARACTERISATION TECHNIQUES

In this section the characterisation techniques exploited in this thesis are reported, along with the relative sample preparation procedures.

6.1. Powder X-ray diffraction (XRD)

The crystallinity and the average crystallite sizes of ZnO samples were analysed through XRD. This is a non-destructive analytical method based on the interaction of an electromagnetic wave and a solid sample. The instrument measures distances similar to the incident wave (X-ray range = 10^{-9} - 10^{-12} m) through the scattering of the incident beam. The wave interfering generated by the process is considered constructing if the resulting wave respects the Bragg's law [219] (**Equation 6.1 I**):

$$2d_{\mathrm{hkl}}\sin\theta = \mathrm{n}\lambda$$

Equation 6.1 I *Bragg's reflection law, where d_{hkl} is the distance between lattice planes, θ is the incident angle, n is the diffraction order and λ is the wavelength of the beam* [219]

The analysis output is a diffractogram where the reflection positions gives information about the elemental cell, their intensity about the atomic positions and their shape about the crystallite morphology and possible defects in the material (see **Figure 6.1 II**).

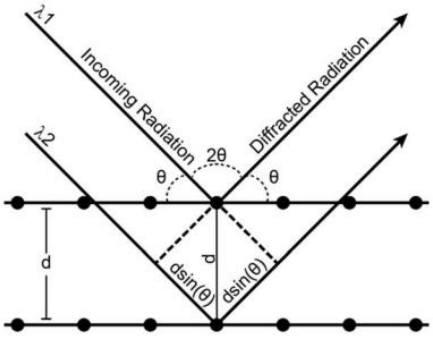

Figure 6.1 II *Geometrical representation of Bragg Law [220]*

Moreover, the average sizes of the crystallites were estimated from the diffractogram using the Scherrer's equation [221], reported in **Equation 6.1 III**.

$$\mathrm{D} = \frac{\mathrm{K}\lambda}{\beta\cos\theta}$$

Equation 6.1 III Scherrer's equation, where D is the mean crystallite size, K is the Scherrer constant (~0.9), λ is the wavelength used in the measurement, β is the full width at half maximum (FWHM) and θ is the Bragg angle of the reflection [221]

In this thesis, a Bruker D8 Advance diffractometer was used with a CuK_α (λ = 1,5406 Å) X-ray source. The data were collected between 20° and 80° 2θ range.

The identification of the compounds was performed with the EVA software from Bruker.

6.2. Dynamic light scattering (DLS)

Dynamic Light Scattering, which is also known as Photon Correlation Spectroscopy, is a technique that provides information regarding the size of the particles present in a suspension. The sample is illuminated by a laser beam, and the fluctuations in the intensity of the scattered light, caused by the Brownian motion of the suspended particles, are measured as a function of time. The relationship between the size of a particle and its velocity due to Brownian motion is defined by the Stokes-Einstein equation (reported in **Equation 6.2 I**) [222].

$$D = \frac{TK_b}{6\,\pi\,\eta\,r_h}$$

Equation 6.2 I *Stokes-Einstein equation where D is the diffusion coefficient, T is the experimental absolute temperature, K_b is the Boltzmann constant, η is the medium viscosity and r_h is the hydrodynamic radius of particles* [222]

When temperature and viscosity are held constant, smaller particles exhibit higher diffusion coefficients and faster changes in scattering intensity, whereas larger particles induce slower changes in intensity due to their slower movement [223]. DLS size measurements were obtained with a MALVERN ZETASIZER Nano-ZS with glass cuvettes.

Moreover, the DLS instrument also enables the calculation of the zeta potential by measuring the particle electrophoretic mobility [224]. In this case, the same equipment was exploited using an electrode cuvette (from the instrument set). For each analysis, 64 scans were used. Solid powder samples were previously dissolved in deionised water and sonicated for 30 seconds with a Sartorius stedim LABSONIC® P.

6.3. Transmission electron microscopy (TEM)

TEM microscope utilizes an electron beam that undergoes scattering upon contact with the atoms of the sample. The transmitted wave is amplified by a system of lenses and then reaches the detector, typically consisting of a charge-coupled device (CCD) or photographic plate. This allows for obtaining high-resolution 2D images, where brighter areas correspond to a greater transmission of electrons, while darker areas, characterized by higher scattering, are due to the presence of heavy atoms or thicker areas of the sample [225].

TEM measurements were performed at the Biology Department (DBio, Dr. Federico Caicci, University of Padua) with a FEI Tecnai G2 microscope (operating at 100 kV) equipped with an Olympus Veleta and a TVIPS F114 cameras. The samples were prepared by depositing a droplet of the suspension containing the

nanoparticles onto a copper grid coated with carbon and let dry at RT. Furthermore, solid samples were also previously treated likewise for DLS and zeta analyses.

6.4. Scanning electron microscopy (SEM)

Scanning electron microscopy (SEM) is a technique for characterizing solid materials by providing information on their size and shape. It exploits the use of an electron beam scanning onto the solid samples. When the electrons collide with the surface, the emission of secondary electrons occurs and a visualisation of the surface morphology takes place. The electron current detected is amplified and converted into three-dimensional images [226].

For this thesis, SEM analyses were performed with a Zeiss SUPRA 40VP microscope with a primary beam acceleration voltage range of 2.0-5.0 kV. Solid samples were prepared with the same procedure as TEM analyses.

6.5. Attenuated total reflectance infrared spectroscopy (ATR-IR)

Fourier transform infrared spectroscopy is an analytical technique used to determine the functional groups present in a compound at characteristic frequencies. In this thesis infrared spectra were taken in ATR mode. In this setting the radiation passes through a particular crystal which allows the electromagnetic wave to be reflected inside itself several times, generating an evanescent wave. Furthermore, the sample is pressed against the crystal that partially absorbs the evanescent radiation (attenuate). The irradiation is continually pulsed until the sample is detected (see schematical representation in **Figure 6.5 I)** [227].

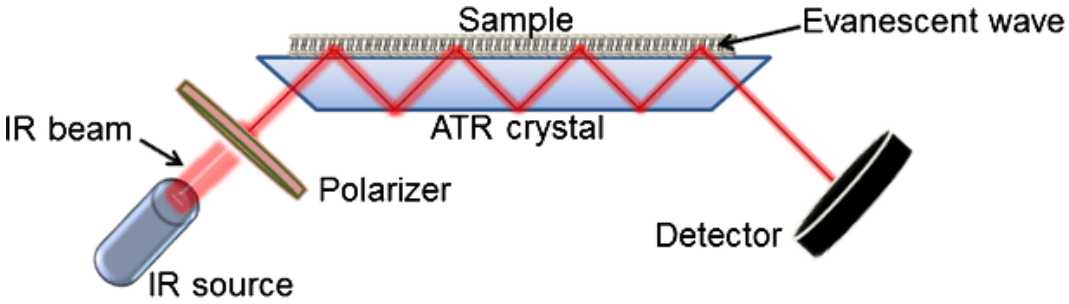

Figure 6.5 I *Schematical representation of the ATR-IR spectroscopy setting [227]*

ATR-IR spectra were retrieved with a NICOLET NEXUS 870 spectrophotometer equipped with a SMART iTX diamond cell. Spectra in the 4000-400 cm^{-1} range spectra were collected through 64 scans with a resolution of 4 cm^{-1}.

6.6. UV-Vis spectroscopy

UV-Vis technique is widely employed in many chemistry subfields. It works by emitting a light beam that passes through a monochromator (which selects a specific wavelength of light). The resulting monochromatic light is then directed through

the sample holder containing the analyte. The sample absorbs some of the light wavelengths, depending on its chemical composition [228].

UV-Vis spectroscopic measurements were performed with an Agilent Varian Cary® 50 UV-Vis Spectrophotometer, using quartz cuvettes at RT. The obtained spectra were fitted into a Gaussian function with the software Origin pro 2018.

6.7. Nuclear Magnetic Resonance spectroscopy (NMR)

The nuclear magnetic resonance (NMR) is used upon of nuclei with spin (namely ^{1}H, ^{13}C and ^{15}N, the most exploited), immersed in an external magnetic field and excited with radio frequencies. Depending on the element of the nucleus and its chemical environment, different wavelengths are absorbed. Exploiting this phenomenon, NMR spectroscopy is used derive the structure of organic compounds [229].

In this thesis, only ^{1}H NMR analyses were performed. Moreover, the measurements were carried out at room temperature with either a Bruker 500 Avance III (equipped with a BBI-ATM-z grad probehead) or a Bruker 400 Avance III HD.

6.8. Electrospray Ionisation-Mass Spectrometry (ESI-MS)

ESI-MS is a spectrometry technique for the detection of compounds within a mixture. The sample is dissolved in a solvent and then charged in the ion source by a high voltage applied to a capillary tube. The charged droplets are desolvated, leaving the analytes ionized. The resulting ions are then transferred to the mass analyzer, where they are separated based on their m/z ratio [230].

ESI-MS analyses were performed with an Agilent Technologies MSD SL Trap. The sample preparation consisted in dissolving the solid in a acetonitrile (ACN) solution (10^{-5} M). The eluent used was a solution of 0.1%$_{w/v}$ formic acid in ACN.

7. EXPERIMENTAL PROCEDURES

In this section the chemicals and materials used, as well as the complete procedures performed, are described.

7.1. Chemicals and materials

The chemical used in this thesis are listed in the following **Table 7.1 I**.

Name	Formula	CAS number	Supplier
zinc acetate dihydrate	$Zn(CH_3COO)_2 \cdot 2H_2O$	5970-45-6	Sigma-Aldrich
sodium hydroxyde	NaOH	1310-73-2	Sigma-Aldrich
oxalic acid dihydrate	$C_2H_6O_6 \cdot 2H_2O$	6153-56-6	Carlo Erba
tetraethylammonium hydroxide (20%$_{p/p}$)	$(C_2H_5)_4N(OH)$	77-98-5	Sigma-Aldrich
sodium citrate tribasic dihydrate	$Na_3C_6H_5O_7 \cdot 2H_2O$	6132-04-3	Sigma-Aldrich
silver nitrate	$Ag(NO_3)$	7761-88-8	Sigma-Aldrich
zinc acetylacetonate	$C_{10}H_{14}O_4Zn$	14024-63-6	Merck
sulphuric acid (96%$_{v/v}$)	H_2SO_4	7664-93-9	Carlo Erba
methanol	CH_3OH	67-56-1	Carlo Erba
sodium nitrite	$NaNO_2$	7632-00-0	Sigma-Aldrich
dopamine hydrochloride	$(HO)_2C_6H_3CH_2CH_2NH_2 \cdot HCl$	62-31-7	Sigma-Aldrich
2-methyl-2-oxazoline	C_4H_7NO	1120-64-5	Sigma-Aldrich
methyl p-toluenesulfonate	$CH_3C_6H_4SO_3CH_3$	80-48-8	Sigma-Aldrich
acetonitrile	CH_3CN	75-05-8	Sigma-Aldrich
ethyl isonipecotate	$C_8H_{15}NO_2$	1126-09-6	Sigma-Aldrich

dimethyl sufoxide-d6	$(CD_3)_2SO$	2206-27-1	Sigma-Aldrich
deuterium oxide	D_2O	7789-20-0	Euriso-top
chloroform-d	$CDCl_3$	865-49-6	Sigma-Aldrich
DCC	$C_6H_{11}N=C=NC_6H_{11}$	538-75-0	Sigma-Aldrich
NHS	$C_4H_5NO_3$	6066-82-6	Sigma-Aldrich
DMF	$HCON(CH_3)_2$	68-12-2	Carlo Erba
DMF, anhydrous	$HCON(CH_3)_2$	68-12-2	Sigma-Aldrich
acetic acid, glacial	CH_3CO_2H	64-19-7	Sigma-Aldrich
triethylamine, anhydrous	$(C_2H_5)_3N$	121-44-8	Sigma-Aldrich
DIPEA, anhydrous	$[(CH_3)_2CH]_2NC_2H_5$	7087-68-5	Sigma-Aldrich
TEA, anhydrous	(C2H5)3N	121-44-8	Sigma-Aldrich
p-xylylendiamine	$C_8H_{12}N_2$	539-48-0	TCI
COMU	$C_{12}H_{19}F_6N_4O_4P$	1075198-30-9	Sigma-Aldrich
HBTU	$C_{11}H_{16}F_6N_5OP$	94790-37-1	Sigma-Aldrich
DL-thioctic acid (lipoic acid)	$C_8H_{14}O_2S_2$	1077-28-7	abcr
dichloromethane	CH_2Cl_2	75-09-2	Carlo erba
calcium hydride	CaH_2	7789-78-8	Sigma-Aldrich
potassium hydroxyde	KOH	1310-58-3	Sigma-Aldrich

7.1 I *Synoptic table of used chemicals*

Most of the previous listed reagents were used at commercial grade without any further purification processes. However, some of them were exploited after a distillation step, in order to obtain anhydrous liquids stored under inert atmosphere (Ar gas). The procedure conditions for the reagents at issue are summarised in the following **Table 7.1 II**.

Chemical	**Water absorbing agent**	**Atmosphere**	**Temperature (°C)**
2-methyl-2-oxazoline	KOH	Ar	130
methyl p-toluenesulfonate	CaH_2	Vacuum (p ≈ 1 mbar)	140
acetonitrile	CaH_2	Ar	105
ethyl isonipecotate	CaH_2	Vacuum (p ≈ 1 mbar)	80

Table 7.1 II *Synoptic table of distillations performed*

In all the above purifications, the chemical was firstly mixed with the water-absorbing agent, under Ar atmosphere for 30 minutes. After that, the temperature was risen through an oil heating bath and, if needed, vacuum was also applied, starting the process. Moreover, the first 10 drops of distilled 2-methyl-2-oxazoline were discarded as they might contain residues of water.

All the procedures which did not exploit an organic solvent, were performed in distilled water. Nevertheless, for synthesis involving Ag, dopamine (or ND) and polymers, milli-Q® water was used instead (filter: Millipak® Express 40).

Regarding microalgae, biological samples were provided from Prof. Thomas Morosinotto's lab. The photoautotrophic microorganisms (Nannocloropsis gaditana, strain CCAP 849/5) were cultivated in a photobioreactor for two weeks, maintaining the pH at 8 through HCl 6 M additions, using sodium bicarbonate as a carbon source. The axenicity was also monitored through microscopical observation. The microbial water suspensions were harvested through centrifugation after the OD_{750} reached 3.1 and stored at 4 °C. In the following **Figure 7.1 III**, the microalgae production process is summarised (the picture is a gentle concession of Dr. Giorgio Perin (Department of Biology (DiBio), University of Padua) who also produced the microalgae for us.

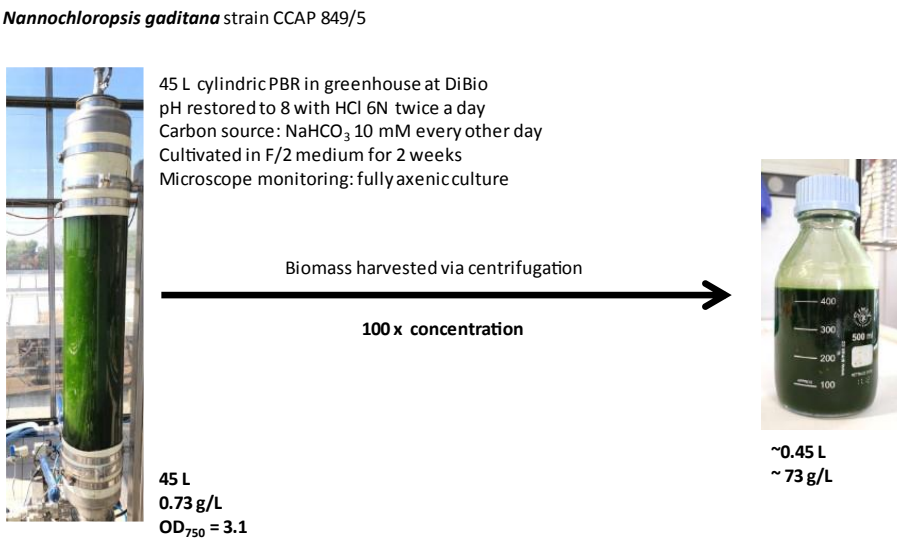

Figure 7.1 III *N. gaditana cultivation process. The picture is a gentle concession from Dr. Giorgio Perin (Department of Biology (DiBio), University of Padua)*

7.2. Zinc oxide particle synthesis

In this section, the synthesis methods exploited for ZnO particles production are described in details.

7.2.1. Non biogenic synthesis

7.2.1.1. Batch synthesis

For a typical ZnO batch synthesis [5], 4.39 g of zinc acetate dyhidrate (0.020 mol) were dissolved into 100 ml of distilled water, in a volumetric flask. The solution was then transferred in a round bottom flask and heated up to boiling point (100 °C, measured with an in-solution thermometer) through an oil bath and a reflux system (using a condenser). To the hot stirring solution, 10 ml of room temperature 10M NaOH were added. The mixture was left stirring and heating for 3 hours. After time passed, the white sol was left cooling at room temperature. The white precipitate was then recovered through three steps of centrifugation and washing in distilled water (fifteen minutes at 13000 rpm, HERMLE Z366 centrifuge with a Z326-0650-HS rotor). Finally, a last washing step in acetone (same centrifugation conditions) removing the remaining acetates was performed. The precipitate was then dried overnight in an oven (MEMMERT CELSIUS 10.0) at 80 °C. The dried solid was finally milled and stored at room temperature.

7.2.1.2. Hydrothermal synthesis

For the synthesis of sample “ZnO 1.2” and “ZnO 1.3”, 2.19 g of zinc acetate (0.01 mol) were dissolved in 10 ml of deionised water in a proper volumetric flask. The solution was then transferred to a PTFE A255AC closed recipient (a “liner”) (23 ml

Teflon® Liner, Parr Instrument Company) along with a 2 ml of NaOH 10 M. The liner was then incapsulated in a stainless steel vessel (4745 General Purpose Acid-Digestion Bomb, Parr Instrument Company). The system was then left in oven at 135 °C for 24 hours (MEMMERT CELSIUS 10.0). After cooling at room temperature, the white precipitate was purified through two centrifugation and washing steps (13000 rpm for 10 minutes, HERMLE Z366 centrifuge with a Z326-0650-HS rotor). Even in this case, a final washing step in acetone was performed. The product was dried overnight in the same oven at 80 °C. Once cooled, it was milled and stored at room temperature.

For sample "ZnO 1.7" [130], 2.75 g of zinc acetylacetonate (0.11 mol) and 1.32 g of oxalic acid (0.11 mol) were suspended in 100 ml of distilled water in a liner (Berghof Pressure Digestion Insert DAB-3 200bar PTFE TFM 250C 210mL Acid 5225200). After, 2 ml of TENOH 20%$_{p/p}$ were also added to the mix. Finally, the pH was then basified up to 10 with a NaOH 10 M water solution and the closed liner was sealed in a stainless stell vessel (Berghof digestec Pressure Vessel (DAB-3 XXL)). The system was left for 24 hours at 135 °C and was subjected to the same treatments of the previous samples (for purification).

7.2.2. Biogenic synthesis

7.2.2.1. Batch biogenic synthesis

For the ZnO biogenic synthesis [132], 1 g of microalgae (corresponding to 13.6 ml of the suspension provided by Prof. Morosinotto's lab) was diluted to 100 ml with distilled water. The suspension was stirred and brought up to boiling point. For "ZnO 2.1" after 20 minutes, the mixture was cooled at room temperature whereas for "ZnO 2.2" it was left at boiling temperature (~100 °C) until the solvent was evaporated and left for another 20 minutes under the same heating conditions. The obtained slurries were resuspended and diluted up to 100 ml with deionised water and vacuum paper filtered (90 mm Black Dot Quantitative Filter Paper Discs / Grade 388). The retrieved liquids were again filtered on paper using another clean paper, obtaining the microalgae extracts. The latter ones were again heated to boiling point, stirred and mixed with a room temperature zinc acetate solution (4.91 g, 0.02 mol, 10 ml). After 3 hours of reaction time, the products were purified in the same fashion of non-biogenic batch ZnO (section **7.2.1.1**).

7.2.2.2. Biogenic-hydrothermal synthesis

For the biogenic-hydrothermal syntheses, a volume corresponding to the targeted microalgae mass was withdrawn from the stored 74 g/l aliquots (4 °C). The suspension was then diluted to 8 ml and processed like the batch biogenic synthesis obtaining the biogenic extract (see previous section **7.2.2.1**). The latter was then mixed with a solution of zinc acetate (0.44 g, 0.002 mol, 3 ml) in a liner (23 ml

Teflon® Liner, Parr Instrument Company) and subjected to the same treatments as the non-biogenic hydrothermal syntheses (section **7.2.2.1**).

7.3. Silver particles synthesis

In the following section, the methodologies used to obtain AgNPs are explained in details.

7.3.1. Turkevich method

7.3.1.1. Normal method

For a classical Ag turkevich method synthesis [90], 0.017 g of $AgNO_3$ (0.0001 mol) (previously kept in the dark) were dissolved in 100 ml of milli-Q® water in a volumetric flask. The solution was then transferred into a conical flask, stirred and heated at boiling point with different reaction times. Once reached boiling point, a sodium citrate tribasic dihydrate room temperature milli-Q® water solution was added (0.1 g, 0.00034 mol, 10 ml), triggering the sol formation. The reaction time was monitored and registered. Once the desired time passed, the reaction was abruptly quenched by dropping the hot conical flask into an ice bath. The yellow suspension obtained was stored in dark at room temperature without any purification steps.

7.3.1.2. Reverse method

Similarly, for a reverse Turkevich Ag synthesis [183], 0.1 g of sodium citrate tribasic dihydrate (0.00034 mol) were dissolved in 100 ml of milli-Q® water in a volumetric flask. The solution was then stirred and boiled in a conical flask. Once reached boiling point a room temperature milli-Q® water solution of $AgNO_3$ (0.017 g, 0.0001 mol, 10 ml) was added to the mix. The process was then stopped at the chosen time point, in the same manner as the Normal method (section **7.3.1.1**). The sol was stored at room temperature in the dark without any purification steps.

7.3.2. Biogenic synthesis

7.3.2.1. Boiling point synthesis

For a hot biogenic synthesis of Ag, the first step was the preparation of the microalgae extract. For that purpose, 1 g of microalgae (corresponding to 13.6 ml of the suspension provided by Prof. Morosinotto's lab) was diluted to 100 ml in milli-Q® water. The suspension was boiled for 20 minutes, cooled at room temperature, vacuum paper filtered (90 mm Black Dot Quantitative Filter Paper Discs / Grade 388). The obtained clean green liquid was further filtered on paper using another clean paper. Finally, the obtained extract was diluted 10 times and 100 ml were withdrawn as a biogenic reactant (corresponding to 0.1 g of initial microalgae suspension). The latter was stirred and heated. Once reached boiling

point, a room temperature milli-Q® water solution of $AgNO_3$ (0.017 g, 0.0001 mol, 10 ml) was added to the mix. The suspension turned slightly grey. The mix was left on stirring and heating for 45 minutes and abruptly cooled in an ice bath. For samples requiring a centrifugation step, this was performed for 3 minutes at 7000 rpm (HERMLE Z366 centrifuge with a Z326-0650-HS rotor) collecting the supernatant. After this step, samples were filtered through CHROMAFIL® Xtra PTFE-20/25 20 µm filters (if it was needed). For instrumental measurements, blank samples containing the same components (but $AgNO_3$) and subjected to the same treatments, were prepared.

7.3.2.2. Room temperature synthesis

For biogenic AgNPs synthesis at room temperature, 100 ml of microalgae extract (prepared as for boiling point synthesis, see previous section **7.3.2.1**) were mixed with a milli-Q® water solution of $AgNO_3$ (0.017 g, 0.0001 mol, 10 ml). The reaction mixture was left stirring in the dark for 24 hours. The next purification steps, for samples which required them, were performed like for Ag boiling point biogenic syntheses (section **7.3.2.1**).

7.4. Polymers synthesis

7.4.1. PMOXA-COOEt polymerisation

The polymer synthesis was performed according to Morgese et al. [120] and the reagents exploited were distilled and used under Ar (with the conditions described in section **7.1**). Firstly, the desired amounts of MOXA (8.51 g (100 mmol, 49 eq) and 4.60 g (54.1 mmol, 93 eq) for PMOXA-50-COOEt and PMOXA-100-COOEt, were dissolved, under Ar, in ACN (16 and 8.5 ml, respectively). Then, 1 eq of methyl p-toluenesulfonate was added to the solutions with a syringe: 380 mg (2.04 mmol) and 108 mg (580 µmol), respectively. The solutions were left to react at 70 °C for 20 hours under stirring in Ar atmosphere. Finally, the polymerisations were terminated though addition of 5 and 10 eq of ethyl isonipecotate at RT, being 1.5 g (1.46 ml, 9.7 mmol) and 0.91 g (0.89 ml, 5.8 mmol), respectively for the polymers with 50 and 100 repeating units. The solutions were left to react for 48 hours under Ar at RT. For both products, the ACN was removed through rotary evaporation (BUCHI® Rotavapor R-300), redissolved in milli-Q® water and dialysed four times against the same solvent using a 1 kDa cut-off membrane (Spectrum™ Labs Spectra/Por™ 6 Pre-wetted Dialysis Tubing). The solutions were eventually frozen and the final solids were obtained by lyophilisation (Künher® Martin Christ ALPHA 1-2 LDplus).

7.4.2. PMOXA-COOH synthesis

Ester hydrolysis was performed following the protocol optimised by Trachsel et al. [198]. Briefly, the solid PMOXA-COOEts were dissolved in the smallest possible volume of a 1 M NaOH Milli-Q® water solution and left stirring in a round bottom flasks overnight at RT. The reaction was then quenched with glacial acetic acid addition, until the pH reached a value of 6. The solutions were dialysed five times, on a 1 kDa cut-off membrane, against milli-Q® water and freeze-dried, like for the polymerisations (previous section **7.4.1**).

7.4.3. Dopamine nitration

The nitration of dopamine was performed following the method by Morgese et al. [120]. 5.011 g (0.026 mol) were dissolved in 200 ml of milli-Q® water along with sodium nitrite (6.309 g, 0.091 mol) and cooled down to 0 °C. Afterwards, 5.3 ml of a 95% $_{v/v}$ H_2SO_4 were added dropwise. The mixture was left stirring at 0 °C for one hour and at RT overnight. The brown slurry was then paper vacuum filtered (90 mm Black Dot Quantitative Filter Paper Discs / Grade 388) and washed with cold milli-Q® water and methanol. The solid retried was eventually recrystallized from milli-Q® water, filtered and washed with the previous procedure and vacuum dried at RT for 3 days.

7.4.4. PMOXA-ND synthesis

The solid polymers were dissolved in 10 ml of distilled ACN, under Ar. 5 ml of two ACN solutions containing NHS and DCC (in the wanted molar ratios based on the polymer used, see section **5.3.3**) (234.4 mg of DCC and 412.4 mg, 0.002 mol) were then added sequentially. The mix was left stirring under Ar for 24 hours at RT. The solid dicyclohexylurea was gravity filtered out (90 mm Black Dot Quantitative Filter Paper Discs / Grade 388) and the PMOXA-NHSs were obtained by precipitation in cold diethyl ether (40 ml) after dissolution in dichloromethane (6 ml). The solid was retrieved by centrifugation and washed three times with cold diethyl ether (ten minutes at 10000 rpm, HERMLE Z366 centrifuge with a Z326-0650-HS rotor). PMOXA-NHSs were subsequently dissolved in 10 ml of anhydrous DMF. After dissolution, 57 mg (0.057 mol, 79 µl) and 30 mg (0.030 mol, 42 µl) of anhydrous TEA were added under Ar for PMOXA-50-NHS and PMOXA-100-NHS, respectively. Previously prepared ND solutions (in anhydrous DMF) were then added dropwise to the mix (281 g and 150 g, respectively). The reaction mixtures were left stirring under Ar at 0 °C for 6h and at RT for another 18 hours. The solids were then precipitated in cold diethyl ether, retrieved through gravity filtration, dissolved in water and dialysed against milli-Q® water until the latter stopped turning yellow (8 times). The final PMOXA-ND solids were obtained through freeze-dying.

7.4.5. PMOXA-NH_2 synthesis

For PMOXA-100-NH_2, the PMOXA-100-COOH powder was mixed with COMU (71 mg, 0.17 mmol) and p-xylylenediamine (46 mg, 0.34 mmol) in a two-necks round bottom flask, in a one-pot fashion. The solid mixture was dissolved, under Ar, in 20 ml of anhydrous DMF (the solution turned yellowish, due to COMU) and 43 mg (0.34 mmol, 58 µl) of dry DIPEA were added. The solution was stirred in Ar at RT for 24 hours. The solvent was then removed through rotary evaporation and the product was redissolved in milli-Q® water to be dialysed against water six times with a 1 kDa cut-off membrane, gravity filtrated and, then, freeze-dried.

For the second coupling, the polymer was dissolved (under Ar) in 15 ml of anhydrous DMF and cooled down to 0 °C. After that, 11 ml of a RT HBTU solution (6.61 g, 0.17 mmol) and 12 mg of dry TEA (0.12 mmol, 16 µl) were added. The mixture was left stirring under Ar at 0 °C for 45 minutes. Finally, 1.4 ml of a p-xylylenediamine solution (16 mg, 0.12 mmol) were added. The reaction solution was left stirring for 72 h at RT. The solvent was eventually removed, and the product was purified as in the previous synthesis.

7.4.6. PMOXA-S-S synthesis

For the synthesis of PMOXA-100-S-S the method used was similar to the one exploited for the second PMOXA-100-NH_2 formation (section **7.4.5**). 8 mg of lipoic acid were dissolved in 10 ml of dry DMF (under Ar) and cooled down to 0 °C in dark (being photosensitive). Subsequently, 3.4 ml of HBTU (33 mg, 0.43 mmol) and 19 mg of DIPEA (0.14 mmol, 25 µl) were added and the resulting mix was left stirring for 45 minutes in dark at 0 °C (under Ar). Finally, the PMOXA-100-NH_2 dry DMF solution is added (4 ml) at RT and the mixture was left stirring for 72 hours (under Ar, RT, in dark). The product was purified as previously done for PMOXA-100-NH_2 (section **7.4.5**).

7.5. Particle functionalisation

7.5.1. ZnO functionalisation

PMOXA-ND functionalisation of ZnO particles was performed as reported from Morgese et al. [120]. Briefly, ZnO and PMOXA-ND were mixed in a round bottom flask in the chosen amounts (weight ratio) and dissolved in 10 ml of dichloromethane. After 36 hours of stirring at RT, the solvent was evaporated, the product was dissolved in milli-Q® water a dialysed four times in a 100 kDa cut-off membrane (Dialysis membrane Spectra/Por® Biotech CE MWCO 100), to remove unbound polymers, and freeze-dried. To obtain the colloids, ZnO@PMOXA solids were suspended in milli-Q® water with a concentration of 0.083 mg/ml. The resulting sols were stored at room temperature.

7.5.2. Ag functionalisation

To obtain Ag@PMOXA 4ml of AgNPs were mixed with a 1 mg/ml milli-Q® water solution of PMOXA-100-S-S in a 15 ml centrifuge tube (Corning™ Falcon™ 15 mL Conical Centrifuge Tube). The dispersions were left under agitation for 72 hours (RT). The suspensions were dialysed four times in a 100 kDa cut-off membrane (Dialysis membrane Spectra/Por® Biotech CE MWCO 100). The sols were finally diluted adding 20 ml of milli-Q® water and stored in dark at RT.

7.6. Data elaboration

The software Origin pro 2018 (version: SR1 b9.5.1.195) was used for data elaboration except for NMR data for which MestReNova (version: 12-0-0) was exploited instead.

8. CONCLUSIONS AND OUTLOOKS

The aim of this thesis was the obtainment of stable water dispersions of ZnO and AgNPs obtained through biogenic synthesis for a possible future application in a biomedical field.

This was carried out through the exploration of new green and cheap pathways to produce already known and marketed materials. The use of a continuously reproducing microorganism, which do not need macronutrients and contribute to atmospheric CO_2 sequestration and may be harvested from other industrial processes, directed the choice over microalgae.

The use of *Nannochloropsis gaditana* posed the problem of purification, since biological components remained adsorbed on the particles, changing the latter properties, such as colloidal stability. To resolve this issue, PMOXA was used as a highly water-soluble polymeric ligand to suspend the obtained nanoparticles.

First, the generation of standard wet chemical benchmarks were achieved for both nano systems. In particular, for ZnO a batch standard sample was easily obtained, whereas for hydrothermal one the use of a peptising agent revealed itself as being crucial for the obtainment of homogenous particles. This observation is in line with the property changes to which the water is subjected during the hydrothermal methods. Regarding the reference standards AgNPs, to establish a repetitive synthesis protocol the reaction time variable was extensively studied. Moreover, the use of a "reverse" protocol led to the production of slightly more monodispersed NPs respect with their classical counterpart. In relation to non-biogenic wet syntheses, all the techniques used were successful.

Once obtained the chemical standard, biogenic syntheses were successfully optimised. For ZnO, the use of heat to thermally purificate the product was required even if, in a green chemistry optic, it was not initially considered. The positive outcome arose from the fact that the heat involved was much less compared to the standard calcination steps present in biogenic literature. ZnO biogenic-hydrothermal syntheses did not yield any product regardless of the relative quantities used, probably due to the unusual reaction conditions. On the other hand, the synthesis of biogenic AgNPs was more complicated. For these systems the adsorption of biological components on the particle surface entailed a loss in colloidal stability and a negative outcome for the whole synthesis. Beside silver, biogenic metal nanoparticles tend not to have long lasting sol stability due to the synthesis exploited itself. Nevertheless, using various purification steps, as well as the aid of PMOXA, it was possible to push the colloidal stability time from 12 hours to 2 weeks. Even if this shelf life is not sufficient for commercialisation, the increase in sol stability (compared to the original one) is still a remarkable achievement. Furthermore, it should be taken into account that the use of less heat conducted to

the production of smaller and less polydisperse AgNPs compared to their hot counterpart. This last result indicated that, in future, the focus of biogenic AgNPs optimal synthesis should be around room temperature methods.

The PMOXA was obtained according to literature and, even if it was not possible to perform an analytical GPC run, the NMR analyses confirmed the positive outcomes for both the polymerisations and the coupling reactions. However, for the PMOXA-100-NH_2 formation synthesis it was not possible to directly obtain a sufficient conversion using COMU as an activating agent. Conversely, the use of another protocol exploiting HBTU resolved the issue, suggesting that the last method is more suitable for PMOXA amide coupling reactions (hence it was adapted and exploited again in the production of PMOXA-100-S-S).

The obtainment of the hybrid materials ZnO@PMOXA and Ag@PMOXA was the pivotal point of this thesis. From DLS measurements, the hydrodynamic diameter increase was similar for ZnO particles with both PMOXA-50-ND and PMOXA-100-ND. The cause of this feature is probably the chain coil effect in water. However, it is very interesting to highlight how (in term of colloidal stability) there are not any differences between the two polymers used for ZnO. Regardless of the ligand, ZnO particle produced by batch and by the biogenic synthesis started to precipitate after 2 weeks (like biogenic Ag@PMOXA). On the other hand, hydrothermal particles (the biggest particles produced in this project) remained completely suspended for all the time frame considered. Regarding the lack of influence from the polymer length and the similar morphology between the two metal oxide systems which precipitated, the instability may be influenced by the particle shape (and the consequent tendency to be functionalised). The previous statement can be also formulated considering that hydrothermal ZnO particles were the most stable colloid (once functionalised) and had the same morphology of those from which the exploited ligation strategy was modelled upon [120]. Regarding Ag@PMOXA, the non-biogenic nanoparticles remained completely stable at every time point while the biogenic one lost its stability after 15 days. This result implies that, even after several purification steps, some biological precipitating agents still remained adsorbed on the metallic surface. Moreover, both biogenic ZnO@PMOXA and Ag@PMOXA began to precipitate at the same time, suggesting that the polymer chosen may have a role in precipitation by itself.

In conclusion, the colloidal stabilisation of biogenic Ag and ZnO particles (along their chemical counterpart) was obtained, even if only for a relative short time. Nonetheless, the main question mark to be answered remains the lack of knowledge about the biological compounds adsorbed on the inorganic surfaces. In the future, systematic studies about this topic are definitively required. Moreover, the use of other polymers, especially branched and with longer chains, should be considered to further stabilise the particles. Regarding biogenic AgNPs, the use of other purification techniques should be also envisioned, as well. Another consideration should be made about the biogenic agent: the use of N. gaditana itself is extremely

reductive considering the variability within photosynthetic organisms. Changing biogenic agent, it might be possible to generate stable particles without the aid of any external polymer as well as producing systems with different morphologies, sizes and concentration of biomolecules adsorbed upon.

Finally, these particles may be exploited in other fields separated from biomedicine. The ZnO particles obtained through the hydrothermal synthesis are too big to be used as injectable formulations, however they may be useful in paint colouring or in photovoltaic cells.

It is worth reminding, at this point, that there is a big market behind nanomaterials and that it pushes towards the production of greener materials and lowering the price, thereby any technology promising these two features must be investigated and kept on the scientific research spotlight.

ACKNOWLEDGMENTS

(versione in italiano alla pagina successiva)

Arriving at this point, which marks the end of my years as a student, it is important to show gratitude to everyone that helped me reaching this goal. First of all, I would like to thank my family for giving the moral support and the financial help (proportional to their possibilities) to complete my studies. In this regard, it is dutiful to thank the University of Padua and ESU Padua for the scholarship granted, giving me the opportunity to live in this city, attend courses and graduate from this prestigious and historical institution (which would have been impossible otherwise). I would like to thank also my friends from my hometown Turin who kept giving me support from afar as well as the ones I made living here who helped me settle and feel at home.

Furthermore, I want to thank the whole AK Colloids research group for welcoming me inside, especially Prof. Silvia Gross for the scientific guidance in the field of inorganic chemistry, Susanna Tinello and Davide Vendrame for the guidance and Martina Leoncini, Corrado Maucieri and Mariarosa Crosato for the mutual support in this long scientific research period. Moreover, I would like also to thank the people from the Macromolecular and Organic Chemistry group and Prof. "Eddy" Benetti for the help, support and sympathy. In particular, special thanks go to Dr. Andrea Rossa for his joyful personality, Carlos Pavon Regana the support and continuous explanations (about everything) and, more importantly, to Alberto Fracasso who many times sacrificed his energies, work and free time for guiding and helping me, even if he was not supposed to (and for his big heart).

RINGRAZIAMENTI

Arrivati a questo punto, che segna la fine dei miei anni da studente, è importante mostrare gratitudine a tutti coloro che mi hanno aiutato a raggiungere questo obiettivo. Innanzitutto, vorrei ringraziare la mia famiglia per avermi fornito il sostegno morale e l'aiuto finanziario (proporzionatamente alle loro possibilità) per completare i miei studi. A tal proposito, è doveroso ringraziare l'Università di Padova e l'ESU di Padova per la borsa di studio concessa, la quale mi ha dato l'opportunità di vivere in questa città, frequentare i corsi e laurearmi presso questa prestigiosa e storica istituzione (cosa altrimenti impossibile). Vorrei ringraziare anche i miei amici della mia città natale, Torino, che mi hanno continuato a sostenere a distanza, così come quelli che ho incontrato qui e che mi hanno aiutato a ambientarmi e sentirmi a casa.

Inoltre, vorrei ringraziare l'intero gruppo di ricerca AK Colloidi per avermi accolto, in particolare la Professoressa Silvia Gross per la sua guida scientifica nella chimica inorganica, Susanna Tinello e Davide Vendrame per la loro guida, e Martina Leoncini, Corrado Maucieri e Mariarosa Crosato per il reciproco sostegno in questo lungo periodo di ricerca scientifica. Vorrei ringraziare anche i componenti del gruppo di Chimica Macromolecolare e Organica e il Professor "Eddy" Benetti per l'aiuto, il sostegno e la simpatia. In particolare, un ringraziamento speciale va al Dr. Andrea Rossa per la sua personalità gioiosa, a Carlos Pavon Regana per il supporto e le continue spiegazioni (su tutto), e, soprattutto, ad Alberto Fracasso che molte volte ha sacrificato le sue energie, il suo lavoro e il suo tempo libero per guidarmi e aiutarmi, anche se non era tenuto a farlo (e per il suo gran cuore).

REFERENCES

1. Sariatli, F. (2017) Linear Economy Versus Circular Economy: A Comparative and Analyzer Study for Optimization of Economy for Sustainability. *Visegrad J. Bioeconomy Sustain. Dev.*, **6** (1), 31–34.
2. Winans, K., Kendall, A., and Deng, H. (2017) The history and current applications of the circular economy concept. *Renew. Sustain. Energy Rev.*, **68**, 825–833.
3. Anastas, P.T., and Warner, J.C. (1998) *Green chemistry : theory and practice*, Oxford University Press, Oxford, UK.
4. Nikam, A.V., Prasad, B.L.V., and Kulkarni, A.A. (2018) Wet chemical synthesis of metal oxidenanoparticles: a review. *CrystEngComm*, **20**, 5091.
5. Bahnemann, D.W., Kormann, C., and Hoffmann, M.R. (1987) Preparation and Characterization of Quantum Size Zinc Oxide: A Detailed Spectroscopic Study. *J Phys Chem*, **91**, 3789–3798.
6. Gul, N., Ata, S., Bibi, I., Ijaz-ul-Mohsin, Azam, M., Shahid, A., Alwadai, N., Masood, N., and Iqbal, M. (2022) Size controlled synthesis of silver nanoparticles: a comparison of modified Turkevich and Brust methods. *Z. Für Phys. Chem.*, **236** (9), 1173–1189.
7. Turkevich, J., Stevenson, P.C., and Hillier, J. (1951) A study of the nucleation and growth processes in the synthesis of colloidal gold. *Discuss. Faraday Soc.*, **11**, 55–75.
8. Rabenau, A. (1985) The Role of Hydrothermal Synthesis in Preparative Chemistry. *Angew. Chem. Int. Ed. Engl.*, **24** (12), 1026–1040.
9. Sharma, D., Kanchi, S., and Bisetty, K. (2019) Biogenic synthesis of nanoparticles: A review. *Arab. J. Chem.*, **12** (8), 3576–3600.
10. Tan, J.S., Lee, S.Y., Chew, K.W., Lam, M.K., Lim, J.W., Ho, S.H., and Show, P.L. (2020) A review on microalgae cultivation and harvesting, and their biomass extraction processing using ionic liquids. *Bioengineered*, **11** (1), 116.
11. Singh, U.B., and Ahluwalia, A.S. (2013) Microalgae: a promising tool for carbon sequestration. *Mitig. Adapt. Strateg. Glob. Change*, **18** (1), 73–95.
12. Durán, N., Marcato, P.D., Durán, M., Yadav, A., Gade, A., and Rai, M. (2011) Mechanistic aspects in the biogenic synthesis of extracellular metal nanoparticles by peptides, bacteria, fungi, and plants. *Appl. Microbiol. Biotechnol.*, **90** (5), 1609–1624.
13. Sirelkhatim, A., Mahmud, S., Seeni, A., Kaus, N.H.M., Ann, L.C., Bakhori, S.K.M., Hasan, H., and Mohamad, D. (2015) Review on Zinc Oxide Nanoparticles: Antibacterial Activity and Toxicity Mechanism. *Nano-Micro Lett.*, **7** (3), 219–242.
14. Sim, W., Barnard, R.T., Blaskovich, M.A.T., and Ziora, Z.M. (2018) Antimicrobial Silver in Medicinal and Consumer Applications: A Patent Review of the Past Decade (2007–2017). *Antibiotics*, **7** (4), 93.

15. Xiong, H.-M. (2013) ZnO Nanoparticles Applied to Bioimaging and Drug Delivery. *Adv. Mater.*, **25** (37), 5329–5335.

16. Savjani, K.T., Gajjar, A.K., and Savjani, J.K. (2012) Drug Solubility: Importance and Enhancement Techniques. *ISRN Pharm.*, **2012**, 195727.

17. Moezzi, A., Cortie, M., and McDonagh, A. (2011) Aqueous pathways for the formation of zinc oxide nanoparticles. *Dalton Trans.*, **40** (18), 4871–4878.

18. Konradi, R., Acikgoz, C., and Textor, M. (2012) Polyoxazolines for Nonfouling Surface Coatings — A Direct Comparison to the Gold Standard PEG. *Macromol. Rapid Commun.*, **33** (19), 1663–1676.

19. Guillerm, B., Monge, S., Lapinte, V., and Robin, J.-J. (2012) How to Modulate the Chemical Structure of Polyoxazolines by Appropriate Functionalization. *Macromol. Rapid Commun.*, **33** (19), 1600–1612.

20. Guzmán-Soto, I., Omole, M., Alarcon, E.I., and McTiernan, C.D. (2020) Lipoic acid capped silver nanoparticles: a facile route to covalent protein capping and oxidative stability within biological systems. *RSC Adv.*, **10** (54), 32953–32958.

21. Kang, T., Oh, D.X., Heo, J., Lee, H.-K., Choy, S., Hawker, C.J., and Hwang, D.S. (2015) Formation, Removal, and Reformation of Surface Coatings on Various Metal Oxide Surfaces Inspired by Mussel Adhesives. *ACS Appl. Mater. Interfaces*, **7** (44), 24656–24662.

22. Alghamdi, G., and Alzahrani, A. (2013) Bonding Formation and Orbitals Nature of Zno Structure. *Middle East J. Sci. Res.*, **13**, 1144–1149.

23. IUPAC. Compendium of Chemical Terminology, 2nd ed. (the "Gold Book"). Compiled by A. D. McNaught and A. Wilkinson. Blackwell Scientific Publications, Oxford (1997). Online version (2019-) created by S. J. Chalk. ISBN 0-9678550-9-8. https://doi.org/10.1351/goldbook.

24. Espitia, P.J.P., Soares, N. de F.F., Coimbra, J.S. dos R., de Andrade, N.J., Cruz, R.S., and Medeiros, E.A.A. (2012) Zinc Oxide Nanoparticles: Synthesis, Antimicrobial Activity and Food Packaging Applications. *Food Bioprocess Technol.*, **5** (5), 1447–1464.

25. Lee, W.C. (2015) Photoelectrochemical water splitting and gas ionisation sensing using metal oxide nanostructures, Doctoral Thesis in Photochemistry, University of Sussex, Brighton.

26. Ching, K.-L., Li, G., Ho, Y.-L., and Kwok, H.-S. (2016) The role of polarity and surface energy in the growth mechanism of ZnO from nanorods to nanotubes. *CrystEngComm*, **18** (5), 779–786.

27. Aspoukeh, P.K., Barzinjy, A.A., and Hamad, S.M. (2022) Synthesis, properties and uses of ZnO nanorods: a mini review. *Int. Nano Lett.*, **12** (2), 153–168.

28. Huang, M.H., Mao, S., Feick, H., Yan, H., Wu, Y., Kind, H., Weber, E., Russo, R., and Yang, P. (2001) Room-Temperature Ultraviolet Nanowire Nanolasers. *Science*, **292** (5523), 1897–1899.

29. Zhang, Y., Chung, J., Lee, J., Myoung, J., and Lim, S. (2011) Synthesis of ZnO nanospheres with uniform nanopores by a hydrothermal process. *J. Phys. Chem. Solids*, **72** (12), 1548–1553.

30. Yang, Z., Ye, Z., Xu, Z., and Zhao, B. (2009) Effect of the morphology on the optical properties of ZnO nanostructures. *Phys. E Low-Dimens. Syst. Nanostructures*, **42** (2), 116–119.

31. Moradpoor, H., Safaei, M., Mozaffari, H.R., Sharifi, R., Imani, M.M., Golshah, A., and Bashardoust, N. (2021) An overview of recent progress in dental applications of zinc oxide nanoparticles. *RSC Adv.*, **11** (34), 21189–21206.

32. Cotton, F.A. (1999) *Advanced inorganic chemistry*, Wiley, New York, NY.

33. Housecroft, C.E., and Sharpe, A.G. (2008) *Inorganic chemistry*, Prentice Hall, Harlow, UK.

34. Chambers, C., and Holliday, A.K. (1975) *Modern inorganic chemistry : an intermediate text*, Butterworths, London, UK.

35. Burdock, G.A., and Carabin, I.G. (2004) Generally recognized as safe (GRAS): history and description. *Toxicol. Lett.*, **150** (1), 3–18.

36. Gil, H.M., Price, T.W., Chelani, K., Bouillard, J.-S.G., Calaminus, S.D.J., and Stasiuk, G.J. (2021) NIR-quantum dots in biomedical imaging and their future. *iScience*, **24** (3), 102189.

37. IUPAC. Compendium of Chemical Terminology, 2nd ed. (the "Gold Book"). Compiled by A. D. McNaught and A. Wilkinson. Blackwell Scientific Publications, Oxford (1997). Online version (2019-) created by S. J. Chalk. ISBN 0-9678550-9-8. https://doi.org/10.1351/goldbook.

38. Kepp, K.P. (2020) Chemical Causes of Metal Nobleness. *ChemPhysChem*, **21** (5), 360–369.

39. Lansdown, A.B.G. (2012) Chapter 4 - Silver and Gold, in *Patty's Toxicology* (eds.Bingham, E., and Cohrssen, B.), vol. 6, Wiley, Hoboken, NJ, 75–112.

40. Liu, X., Luo, J., and Zhu, J. (2006) Size Effect on the Crystal Structure of Silver Nanowires. *Nano Lett.*, **6** (3), 408–412.

41. Taneja, P., Banerjee, R., Ayyub, P., and Dey, G.K. (2001) Observation of a hexagonal *(4H)* phase in nanocrystalline silver. *Phys. Rev. B*, **64** (3), 033405.

42. Fan, Z., Bosman, M., Huang, X., Huang, D., Yu, Y., Ong, K.P., Akimov, Y.A., Wu, L., Li, B., Wu, J., Huang, Y., Liu, Q., Eng Png, C., Lip Gan, C., Yang, P., and Zhang, H. (2015) Stabilization of 4H hexagonal phase in gold nanoribbons. *Nat. Commun.*, **6** (1), 7684.

43. Auvert, G., and Auvert, M. (2016) The Even-Odd and the Isoelectronicity Rules Applied to Single Covalent Bonds in Ionic, Double-Face-Centered Cubic and Diamond-Like Crystals. *Open J. Phys. Chem.*, **06**, 21–33.

44. Othman, N., Mat, H., and Goto, M. (2006) Separation of silver from photographic wastes by emulsion liquid membrane system. *J. Membr. Sci.*, **282** (1), 171–177.

45. Li, W.-X., Stampfl, C., and Scheffler, M. (2003) Why is a Noble Metal Catalytically Active? The Role of the O-Ag Interaction in the Function of Silver as an Oxidation Catalyst. *Phys. Rev. Lett.*, **90** (25), 256102.

46. Zhang, Y., Ferguson, S.A., Watanabe, F., Jones, Y., Xu, Y., Biris, A.S., Hussain, S., and Ali, S.F. (2013) Silver Nanoparticles Decrease Body Weight and Locomotor Activity in Adult Male Rats. *Small*, **9** (9–10), 1715–1720.

47. Kolwas, K., and Derkachova, A. (2020) Impact of the Interband Transitions in Gold and Silver on the Dynamics of Propagating and Localized Surface Plasmons. *Nanomaterials*, **10** (7), 1411.

48. González, A.L., Noguez, C., Beránek, J., and Barnard, A.S. (2014) Size, Shape, Stability, and Color of Plasmonic Silver Nanoparticles. *J. Phys. Chem. C*, **118** (17), 9128–9136.

49. Haider, A.J., Haider, M.J., and Mehde, M.S. (2018) A review on preparation of silver nano-particles. *AIP Conf. Proc.*, **1968** (1), 030086.

50. Freestone, I., Meeks, N., Sax, M., and Higgitt, C. (2007) The Lycurgus Cup — A Roman nanotechnology. *Gold Bull.*, **40** (4), 270–277.

51. Drozdov, A., Andreev, M., Kozlov, M., Petukhov, D., Klimonsky, S., and Pettinari, C. (2021) Lycurgus cup: the nature of dichroism in a replica glass having similar composition. *J. Cult. Herit.*, **51**, 71–78.

52. Auffan, M., Rose, J., Bottero, J.-Y., Lowry, G.V., Jolivet, J.-P., and Wiesner, M.R. (2009) Towards a definition of inorganic nanoparticles from an environmental, health and safety perspective. *Nat. Nanotechnol.*, **4** (10), 634–641.

53. Peiris, S., McMurtrie, J., and Zhu, H.-Y. (2016) Metal nanoparticle photocatalysts: emerging processes for green organic synthesis. *Catal. Sci. Technol.*, **6** (2), 320–338.

54. Mogensen, K.B., and Kneipp, K. (2014) Size-Dependent Shifts of Plasmon Resonance in Silver Nanoparticle Films Using Controlled Dissolution: Monitoring the Onset of Surface Screening Effects. *J. Phys. Chem. C*, **118** (48), 28075–28083.

55. Fan, X., Zheng, W., and Singh, D.J. (2014) Light scattering and surface plasmons on small spherical particles. *Light Sci. Appl.*, **3** (6), e179–e179.

56. Fernando, I., Qian, T., and Zhou, Y. (2019) Long term impact of surfactants & polymers on the colloidal stability, aggregation and dissolution of silver nanoparticles. *Environ. Res.*, **179**, 108781.

57. Frens, G. (1972) Particle size and sol stability in metal colloids. *Kolloid-Z. Z. Für Polym.*, **250** (7), 736–741.

58. Jakab, A., Rosman, C., Khalavka, Y., Becker, J., Trügler, A., Hohenester, U., and Sönnichsen, C. (2011) Highly Sensitive Plasmonic Silver Nanorods. *ACS Nano*, **5** (9), 6880–6885.

59. Shehla, H., Ishaq, A., Khan, Y., Javed, I., Saira, R., Shahzad, N., and Maaza, M. (2016) Ion beam irradiation-induced nano-welding of Ag nanowires. *Micro Nano Lett.*, **11** (1), 34–37.

60. Qi, X., Balankura, T., Zhou, Y., and Fichthorn, K.A. (2015) How Structure-Directing Agents Control Nanocrystal Shape: Polyvinylpyrrolidone-Mediated Growth of Ag Nanocubes. *Nano Lett.*, **15** (11), 7711–7717.

61. Washio, I., Xiong, Y., Yin, Y., and Xia, Y. (2006) Reduction by the End Groups of Poly(vinyl pyrrolidone): A New and Versatile Route to the Kinetically Controlled Synthesis of Ag Triangular Nanoplates. *Adv. Mater.*, **18** (13), 1745–1749.

62. Syafiuddin, A., Salmiati, Salim, M.R., Beng Hong Kueh, A., Hadibarata, T., and Nur, H. (2017) A Review of Silver Nanoparticles: Research Trends, Global Consumption, Synthesis, Properties, and Future Challenges. *J. Chin. Chem. Soc.*, **64** (7), 732–756.

63. Inshakova, E., and Inshakov, O. (2017) World market for nanomaterials: structure and trends. *MATEC Web Conf.*, **129**, 02013.

64. Kołodziejczak-Radzimska, A., and Jesionowski, T. (2014) Zinc Oxide—From Synthesis to Application: A Review. *Materials*, **7** (4), 2833–2881.

65. Wibowo, A., Marsudi, M.A., Amal, M.I., Ananda, M.B., Stephanie, R., Ardy, H., and Diguna, L.J. (2020) ZnO nanostructured materials for emerging solar cell applications. *RSC Adv.*, **10** (70), 42838–42859.

66. Jagtap, S., Chopade, P., Tadepalli, S., Bhalerao, A., and Gosavi, S. (2019) A review on the progress of ZnSe as inorganic scintillator. *Opto-Electron. Rev.*, **27** (No 1), 90–103.

67. Moyen, E., Kim, J.H., Kim, J., and Jang, J. (2020) ZnO Nanoparticles for Quantum-Dot-Based Light-Emitting Diodes. *ACS Appl. Nano Mater.*, **3** (6), 5203–5211.

68. Bonsak, J., Mayandi, J., Thøgersen, A., Stensrud Marstein, E., and Mahalingam, U. (2011) Chemical synthesis of silver nanoparticles for solar cell applications. *Phys. Status Solidi C*, **8** (3), 924–927.

69. Bai, X.-F., Song, T., Xu, Z., Xia, C.-G., Huang, W.-S., and Xu, L.-W. (2015) Aromatic Amide-Derived Non-Biaryl Atropisomers as Highly Efficient Ligands in Silver-Catalyzed Asymmetric Cycloaddition Reactions. *Angew. Chem. Int. Ed.*, **54** (17), 5255–5259.

70. Kumawat, A., Chattopadhyay, S., Verma, R.K., and Misra, K.P. (2022) Eu doped ZnO nanoparticles with strong potential of thermal sensing and bioimaging. *Mater. Lett.*, **308**, 131221.

71. Nadort, A., Zhao, J., and Goldys, E.M. (2016) Lanthanide upconversion luminescence at the nanoscale: fundamentals and optical properties. *Nanoscale*, **8** (27), 13099–13130.

72. Aldeek, F., Mustin, C., Balan, L., Medjahdi, G., Roques-Carmes, T., Arnoux, P., and Schneider, R. (2011) Enhanced Photostability from CdSe(S)/ZnO Core/Shell Quantum Dots and Their Use in Biolabeling. *Eur. J. Inorg. Chem.*, **2011** (6), 794–801.

73. Xiong, H.-M., Xu, Y., Ren, Q.-G., and Xia, Y.-Y. (2008) Stable Aqueous ZnO@Polymer Core−Shell Nanoparticles with Tunable Photoluminescence and Their Application in Cell Imaging. *J. Am. Chem. Soc.*, **130** (24), 7522–7523.

74. Larguinho, M., and Baptista, P.V. (2012) Gold and silver nanoparticles for clinical diagnostics — From genomics to proteomics. *Proteomics Clin. Link*, **75** (10), 2811–2823.

75. Chernousova, S., and Epple, M. (2013) Silver as Antibacterial Agent: Ion, Nanoparticle, and Metal. *Angew. Chem. Int. Ed.*, **52** (6), 1636–1653.

76. Radetić, M. (2013) Functionalization of textile materials with silver nanoparticles. *J. Mater. Sci.*, **48** (1), 95–107.

77. Dulińska-Litewka, J., Dykas, K., Felkle, D., Karnas, K., Khachatryan, G., and Karewicz, A. (2022) Hyaluronic Acid-Silver Nanocomposites and Their Biomedical Applications: A Review. *Materials*, **15** (1), 234.

78. Yin, I.X., Zhang, J., Zhao, I.S., Mei, M.L., Li, Q., and Chu, C.H. (2020) The Antibacterial Mechanism of Silver Nanoparticles and Its Application in Dentistry. *Int. J. Nanomedicine*, **15**, 2555–2562.

79. Zorov, D.B., Juhaszova, M., and Sollott, S.J. (2014) Mitochondrial Reactive Oxygen Species (ROS) and ROS-Induced ROS Release. *Physiol. Rev.*, **94** (3), 909–950.

80. Abid, N., Khan, A.M., Shujait, S., Chaudhary, K., Ikram, M., Imran, M., Haider, J., Khan, M., Khan, Q., and Maqbool, M. (2022) Synthesis of nanomaterials using various top-down and bottom-up approaches, influencing factors, advantages, and disadvantages: A review. *Adv. Colloid Interface Sci.*, **300**, 102597.

81. Tzounis, L. (2019) Chapter 9 - Synthesis and Processing of Thermoelectric Nanomaterials, Nanocomposites, and Devices, in *Nanomaterials synthesis : design, fabrication and applications* (eds.Beeran Pottathara, Y., Thomas, S., Kalarikkal, N., Grohens, Y., and Kokol, V.), Elsevier, Amsterdam, Netherlands, 295–336.

82. Adil, M., Abdelkareem, M.A., Sayed, E.T., Rodriguez, C., Ramadan, M., and Olabi, A.-G. (2022) Progress of Metal Chalcogenides in Supercapacitors, in *Encyclopedia of Smart Materials* (eds.Olabi, A.-G.), Elsevier, Amsterdam, 424–433.

83. LaMer, V.K., and Dinegar, R.H. (1950) Theory, Production and Mechanism of Formation of Monodispersed Hydrosols. *J. Am. Chem. Soc.*, **72** (11), 4847–4854.

84. Sugimoto, T. (1992) The theory of the nucleation of monodisperse particles in open systems and its application to AgBr systems. *J. Colloid Interface Sci.*, **150** (1), 208–225.

85. Einarsrud, M.-A., and Grande, T. (2014) 1D oxide nanostructures from chemical solutions. *Chem. Soc. Rev.*, **43** (7), 2187–2199.

86. Holzapfel, W.B. (1969) Effect of Pressure and Temperature on the Conductivity and Ionic Dissociation of Water up to 100 kbar and 1000°C. *J. Chem. Phys.*, **50** (10), 4424–4428.

87. Uematsu, M., and Franck, E.U. (1980) Static Dielectric Constant of Water and Steam. *J. Phys. Chem. Ref. Data*, **9** (4), 1291–1306.

88. Deguchi, S., Ghosh, S.K., Alargova, R.G., and Tsujii, K. (2006) Viscosity Measurements of Water at High Temperatures and Pressures Using Dynamic Light Scattering. *J. Phys. Chem. B*, **110** (37), 18358–18362.

89. Dembek, M., and Bocian, S. (2020) Pure water as a mobile phase in liquid chromatography techniques. *TrAC Trends Anal. Chem.*, **123**, 115793.

90. Enustun, B.V., and Turkevich, John. (1963) Coagulation of Colloidal Gold. *J. Am. Chem. Soc.*, **85** (21), 3317–3328.

91. Brust, M., Walker, M., Bethell, D., Schiffrin, D.J., and Whyman, R. (1994) Synthesis of thiol-derivatised gold nanoparticles in a two-phase Liquid–Liquid system. *J. Chem. Soc. Chem. Commun.*, (7), 801–802.

92. Kettemann, F., Birnbaum, A., Witte, S., Wuithschick, M., Pinna, N., Kraehnert, R., Rademann, K., and Polte, J. (2016) Missing Piece of the Mechanism of the Turkevich Method: The Critical Role of Citrate Protonation. *Chem. Mater.*, **28** (11), 4072–4081.

93. Singh, P., Kim, Y.-J., Zhang, D., and Yang, D.-C. (2016) Biological Synthesis of Nanoparticles from Plants and Microorganisms. *Trends Biotechnol.*, **34** (7), 588–599.

94. Kundu, D., Hazra, C., Chatterjee, A., Chaudhari, A., and Mishra, S. (2014) Extracellular biosynthesis of zinc oxide nanoparticles using Rhodococcus pyridinivorans NT2: Multifunctional textile finishing, biosafety evaluation and in vitro drug delivery in colon carcinoma. *J. Photochem. Photobiol. B*, **140**, 194–204.

95. El-Rafie, H.M., El-Rafie, M.H., and Zahran, M.K. (2013) Green synthesis of silver nanoparticles using polysaccharides extracted from marine macro algae. *Carbohydr. Polym.*, **96** (2), 403–410.

96. Mokhtari, N., Daneshpajouh, S., Seyedbagheri, S., Atashdehghan, R., Abdi, K., Sarkar, S., Minaian, S., Shahverdi, H.R., and Shahverdi, A.R. (2009) Biological synthesis of very small silver nanoparticles by culture supernatant of Klebsiella pneumonia: The effects of visible-light irradiation and the liquid mixing process. *Mater. Res. Bull.*, **44** (6), 1415–1421.

97. Kannan, R.R.R., Arumugam, R., Ramya, D., Manivannan, K., and Anantharaman, P. (2013) Green synthesis of silver nanoparticles using marine macroalga Chaetomorpha linum. *Appl. Nanosci.*, **3** (3), 229–233.

98. Hietzschold, S., Walter, A., Davis, C., Taylor, A.A., and Sepunaru, L. (2019) Does Nitrate Reductase Play a Role in Silver Nanoparticle Synthesis? Evidence for NADPH as the Sole Reducing Agent. *ACS Sustain. Chem. Eng.*, **7** (9), 8070–8076.

99. Nagarajan, S., and Arumugam Kuppusamy, K. (2013) Extracellular synthesis of zinc oxide nanoparticle using seaweeds of gulf of Mannar, India. *J. Nanobiotechnology*, **11** (1), 39.

100. Joseph, E., and Singhvi, G. (2019) Chapter 4 - Multifunctional nanocrystals for cancer therapy: a potential nanocarrier, in *Nanomaterials for Drug Delivery and Therapy* (eds.Grumezescu, A.M.), Elsevier, Amsterdam, Netherlands, 91–116.

101. Fawcett, D., Verduin, J.J., Shah, M., Sharma, S.B., and Poinern, G.E.J. (2017) A Review of Current Research into the Biogenic Synthesis of Metal and Metal Oxide Nanoparticles via Marine Algae and Seagrasses. *J. Nanosci.*, **2017**, 8013850.

102. Jacob, J.M., Ravindran, R., Narayanan, M., Samuel, S.M., Pugazhendhi, A., and Kumar, G. (2021) Microalgae: A prospective low cost green alternative for nanoparticle synthesis. *Curr. Opin. Environ. Sci. Health*, **20**, 100163.

103. Eltaweil, A.S., Abdelfatah, A.M., Hosny, M., and Fawzy, M. (2022) Novel Biogenic Synthesis of a Ag@Biochar Nanocomposite as an Antimicrobial Agent and Photocatalyst for Methylene Blue Degradation. *ACS Omega*, **7** (9), 8046–8059.

104. Camacho-Rodríguez, J., Cerón-García, M.C., González-López, C.V., Fernández-Sevilla, J.M., Contreras-Gómez, A., and Molina-Grima, E. (2013) A low-cost culture medium for the production of Nannochloropsis gaditana biomass optimized for aquaculture. *Bioresour. Technol.*, **144**, 57–66.

105. Priyadarshani, I., and Rath, B. (2012) Commercial and industrial applications of micro algae–A review. *J. Algal Biomass Util.*, **3** (4), 89–100.

106. Muylaert, K., Bastiaens, L., Vandamme, D., and Gouveia, L. (2017) 5 - Harvesting of microalgae: Overview of process options and their strengths and drawbacks, in *Microalgae-Based Biofuels and Bioproducts: From Feedstock Cultivation to End-Products*, Woodhead Publishing, Sawston, UK, 113–132.

107. Riisberg, I., Orr, R.J.S., Kluge, R., Shalchian-Tabrizi, K., Bowers, H.A., Patil, V., Edvardsen, B., and Jakobsen, K.S. (2009) Seven Gene Phylogeny of Heterokonts. *Protist*, **160** (2), 191–204.

108. Yukesh Kannah, R., Kavitha, S., Parthiba Karthikeyan, O., Rene, E.R., Kumar, G., and Rajesh Banu, J. (2021) A review on anaerobic digestion of energy and cost effective microalgae pretreatment for biogas production. *Bioresour. Technol.*, **332**, 125055.

109. Archibald, J.M., and Keeling, P.J. (2002) Recycled plastids: a 'green movement' in eukaryotic evolution. *Trends Genet.*, **18** (11), 577–584.

110. Macías-Sánchez, M.D., Mantell, C., Rodríguez, M., Martínez de la Ossa, E., Lubián, L.M., and Montero, O. (2005) Supercritical fluid extraction of carotenoids and chlorophyll a from Nannochloropsis gaditana. *J. Food Eng.*, **66** (2), 245–251.

111. Paliwal, C., Mitra, M., Bhayani, K., Bharadwaj, S.V.V., Ghosh, T., Dubey, S., and Mishra, S. (2017) Abiotic stresses as tools for metabolites in microalgae. *SIAlgal Biorefinery*, **244**, 1216–1226.

112. Edwards, B., Jaswal, R., Pathak, A., and Chauhan, A. (2022) Chapter 11 - Current trends in algal biotechnology for the generation of sustainable biobased products, in *Microbial Biodegradation and Bioremediation (Second Edition)* (eds.Das, S., and Dash, H.R.), Elsevier, Amsterdam, Netherlands, 213–239.

113. Abirami, S., Murugesan, S., Sivamurugan, V., and Sivaswamy, S.N. (1970) Screening and optimization of culture conditions of Nannochloropsis gaditana for omega 3 fatty acid production. *J. Appl. Biol. Biotechnol.*, **5** (3), 013–017.

114. Greenwald, R.B. (2001) PEG drugs: an overview. *Proceeding Int. Symp. Tumor Target. Deliv. Syst.*, **74** (1), 159–171.

115. Harris, J.M., Martin, N.E., and Modi, M. (2001) Pegylation. *Clin. Pharmacokinet.*, **40** (7), 539–551.

116. Nemati Mahand, S., Aliakbarzadeh, S., Moghaddam, A., Salehi Moghaddam, A., Kruppke, B., Nasrollahzadeh, M., and Khonakdar, H.A. (2022) Polyoxazoline: A review article from polymerization to smart behaviors and biomedical applications. *Eur. Polym. J.*, **178**, 111484.

117. Tavano, R., Gabrielli, L., Lubian, E., Fedeli, C., Visentin, S., Polverino De Laureto, P., Arrigoni, G., Geffner-Smith, A., Chen, F., Simberg, D., Morgese, G., Benetti, E.M., Wu, L., Moghimi, S.M., Mancin, F., and Papini, E. (2018) C1q-Mediated Complement Activation and C3 Opsonization Trigger Recognition of Stealth Poly(2-methyl-2-oxazoline)-Coated Silica Nanoparticles by Human Phagocytes. *ACS Nano*, **12** (6), 5834–5847.

118. Pinnataip, R., and Lee, B.P. (2021) Oxidation Chemistry of Catechol Utilized in Designing Stimuli-Responsive Adhesives and Antipathogenic Biomaterials. *ACS Omega*, **6** (8), 5113–5118.

119. Wahlberg, L.U. (2014) Chapter 62 - Brain Implants, in *Principles of Tissue Engineering (Fourth Edition)* (eds.Lanza, R., Langer, R., and Vacanti, J.), Elsevier/Academic Press, London, UK, 1329–1342.

120. Morgese, G., Causin, V., Maggini, M., Corrà, S., Gross, S., and Benetti, E.M. (2015) Ultrastable Suspensions of Polyoxazoline-Functionalized ZnO Single Nanocrystals. *Chem. Mater.*, **27** (8), 2957–2964.

121. Amstad, E., Gehring, A.U., Fischer, H., Nagaiyanallur, V.V., Hähner, G., Textor, M., and Reimhult, E. (2011) Influence of Electronegative Substituents on the Binding Affinity of Catechol-Derived Anchors to Fe3O4 Nanoparticles. *J. Phys. Chem. C*, **115** (3), 683–691.

122. Solomon, E.I., Gorelsky, S.I., and Dey, A. (2006) Metal–thiolate bonds in bioinorganic chemistry. *J. Comput. Chem.*, **27** (12), 1415–1428.

123. Inkpen, M.S., Liu, Z., Li, H., Campos, L.M., Neaton, J.B., and Venkataraman, L. (2019) Non-chemisorbed gold–sulfur binding prevails in self-assembled monolayers. *Nat. Chem.*, **11** (4), 351–358.

124. Sahli, R., Fave, C., Raouafi, N., Boujlel, K., Schöllhorn, B., and Limoges, B. (2013) Switching On/Off the Chemisorption of Thioctic-Based Self-Assembled Monolayers on Gold by Applying a Moderate Cathodic/Anodic Potential. *Langmuir*, **29** (17), 5360–5368.

125. Espíndola, K.M., Varela, E.L., de Albuquerque, R.D., Figueiredo, R.A., dos Santos, S.M., Malcher, N.S., da S. Seabra, P.S., Fonseca, A.D., de Azevedo Sousa, K.M., de Oliveira, S.B., Carneiro, A.D., Coleman, M.D., and Monteiro, M.C. (2023) Alpha-Lipoic Acid and Its Enantiomers Prevent Methemoglobin Formation and DNA Damage Induced by Dapsone Hydroxylamine: Molecular Mechanism and Antioxidant Action. *Int. J. Mol. Sci.*, **24** (1), 57.

126. Ruchika, Kumari, S., Dhiman, P., Singh, D., and Saneja, A. (2022) R-α-Lipoic Acid Conjugated to d-α-Tocopherol Polyethylene Glycol 1000

Succinate: Synthesis, Characterization, and Effect on Antiseizure Activity. *J. Agric. Food Chem.*, **70** (25), 7674–7682.

127. Salehi, B., Berkay Yılmaz, Y., Antika, G., Boyunegmez Tumer, T., Fawzi Mahomoodally, M., Lobine, D., Akram, M., Riaz, M., Capanoglu, E., Sharopov, F., Martins, N., Cho, W.C., and Sharifi-Rad, J. (2019) Insights on the Use of α-Lipoic Acid for Therapeutic Purposes. *Biomolecules*, **9** (8), 356.

128. Hajtuch, J., Santos-Martinez, M.J., Wojcik, M., Tomczyk, E., Jaskiewicz, M., Kamysz, W., Narajczyk, M., and Inkielewicz-Stepniak, I. (2022) Lipoic Acid-Coated Silver Nanoparticles: Biosafety Potential on the Vascular Microenvironment and Antibacterial Properties. *Front. Pharmacol.*, **12**, 733743.

129. Metsoviti, M.N., Papapolymerou, G., Karapanagiotidis, I.T., and Katsoulas, N. (2020) Effect of Light Intensity and Quality on Growth Rate and Composition of Chlorella vulgaris. *Plants*, **9** (1), 31.

130. Diodati, S., Hennemann, J., Fresno, F., Gialanella, S., Dolcet, P., Lavrenčič Štangar, U., Smarsly, B.M., and Gross, S. (2019) Easy and green Route towards Nanostructured ZnO as an Active Sensing Material with Unexpected H_2S Dosimeter-Type Behaviour. *Eur. J. Inorg. Chem.*, **2019** (6), 837–846.

131. Gul, N., Ata, S., Bibi, I., Ijaz-ul-Mohsin, Azam, M., Shahid, A., Alwadai, N., Masood, N., and Iqbal, M. (2022) Size controlled synthesis of silver nanoparticles: a comparison of modified Turkevich and BRUST methods. *Z. Für Phys. Chem.*, **236** (9), 1173–1189.

132. Tinello, S. (2022) Optimisation of a green synthesis of zinc oxide nanoparticles exploiting an algae-mediated biogenic approach, Master's Degree Thesis in Industrial biotechnologies, University of Padua, Padua.

133. Dolcet, P., Latini, F., Casarin, M., Speghini, A., Tondello, E., Foss, C., Diodati, S., Verin, L., Motta, A., and Gross, S. (2013) Inorganic Chemistry in a Nanoreactor: Doped ZnO Nanostructures by Miniemulsion. *Eur. J. Inorg. Chem.*, **2013** (13), 2291–2300.

134. Reichle, R.A., McCurdy, K.G., and Hepler, L.G. (1975) Zinc Hydroxide: Solubility Product and Hydroxy-complex Stability Constants from 12.5–75 °C. *Can. J. Chem.*, **53** (24), 3841–3845.

135. Wang, M., Zhou, Y., Zhang, Y., Hahn, S.H., and Kim, E.J. (2011) From Zn(OH)2 to ZnO: a study on the mechanism of phase transformation. *CrystEngComm*, **13** (20), 6024–6026.

136. McBride, R.A., Kelly, J.M., and McCormack, D.E. (2003) Growth of well-defined ZnO microparticles by hydroxide ion hydrolysis of zinc salts. *J. Mater. Chem.*, **13** (5), 1196–1201.

137. Ghorbani, H.R., Mehr, F.P., Pazoki, H., and Rahmani, B.M. (2015) Synthesis of ZnO Nanoparticles by Precipitation Method. *Orient. J. Chem.*, **31** (2), 1219–1221.

138. Musić, S., Dragčević, Đ., Popović, S., and Ivanda, M. (2005) Precipitation of ZnO particles and their properties. *Mater. Lett.*, **59** (19), 2388–2393.

139. Fatehah, M.O., Aziz, H.A., and Stoll, S. (2014) Stability of ZnO nanoparticles in solution. Influence of pH, dissolution, aggregation and disaggregation effects. *J. Colloid Sci. Biotechnol.*, **3** (1), 75–84.

140. Goux, A., Pauporté, T., Chivot, J., and Lincot, D. (2005) Temperature effects on ZnO electrodeposition. *Electrochimica Acta*, **50** (11), 2239–2248.

141. Narendra Kumar, H.K., Chandra Mohana, N., Nuthan, B.R., Ramesha, K.P., Rakshith, D., Geetha, N., and Satish, S. (2019) Phyto-mediated synthesis of zinc oxide nanoparticles using aqueous plant extract of Ocimum americanum and evaluation of its bioactivity. *SN Appl. Sci.*, **1** (6), 651.

142. Ngoepe, N.M., Mbita, Z., Mathipa, M., Mketo, N., Ntsendwana, B., and Hintsho-Mbita, N.C. (2018) Biogenic synthesis of ZnO nanoparticles using Monsonia burkeana for use in photocatalytic, antibacterial and anticancer applications. *Ceram. Int.*, **44** (14), 16999–17006.

143. Ebadi, M., Zolfaghari, M.R., Aghaei, S.S., Zargar, M., Shafiei, M., Zahiri, H.S., and Noghabi, K.A. (2019) A bio-inspired strategy for the synthesis of zinc oxide nanoparticles (ZnO NPs) using the cell extract of cyanobacterium Nostoc sp. EA03: from biological function to toxicity evaluation. *RSC Adv.*, **9** (41), 23508–23525.

144. Rajesh, D., Vara Lakshmi, B., and Sunandana, C.S. (2012) Two-step synthesis and characterization of ZnO nanoparticles. *Phys. B Condens. Matter*, **407** (23), 4537–4539.

145. Scherrer, P. (1912) Bestimmung der inneren Struktur und der Größe von Kolloidteilchen mittels Röntgenstrahlen, in *Kolloidchemie Ein Lehrbuch* (eds.Zsigmondy, R.), Springer, Berlin, Germany, 387–409.

146. Patterson, A.L. (1939) The Scherrer Formula for X-Ray Particle Size Determination. *Phys. Rev.*, **56** (10), 978–982.

147. Esthappan, S.K., Nair, A.B., and Joseph, R. (2015) Effect of crystallite size of zinc oxide on the mechanical, thermal and flow properties of polypropylene/zinc oxide nanocomposites. *Compos. Part B Eng.*, **69**, 145–153.

148. Hamdi, S., Smaoui, H., Guermazi, S., Leroy, G., and Duponchel, B. (2022) Enhancing the structural, optical and electrical conductivity properties of ZnO nanopowders through Dy doping. *Inorg. Chem. Commun.*, **144**, 109819.

149. Bai, S., Hu, J., Li, D., Luo, R., Chen, A., and Liu, C.C. (2011) Quantum-sized ZnO nanoparticles: Synthesis, characterization and sensing properties for NO2. *J. Mater. Chem.*, **21** (33), 12288–12294.

150. Vijayalakshmi, D., Chellappa, M., Anjaneyulu, U., Manivasagam, G., and Sethu, S. (2015) Influence of Coating Parameter and Sintering Atmosphere on the Corrosion Resistance Behavior of Electrophoretically Deposited Composite Coatings. *Mater. Manuf. Process.*, **31**, 95–106.

151. Socrates, G. (2004) Chapter 10 - The Carboxyl Group: C=O, in *Infrared and Raman Characteristic Group Frequencies: Tables and Charts*, Wiley, Chichester, UK, 115–154.

152. Socrates, G. (2004) Chapter 6 - Hydroxyl Group Compounds: O-H Group, in *Infrared and Raman Characteristic Group Frequencies: Tables and Charts*, Wiley, Chichester, UK, 94–99.

153. Lu, G.W., and Gao, P. (2010) Chapter 3 - Emulsions and Microemulsions for Topical and Transdermal Drug Delivery, in *Handbook of Non-Invasive Drug Delivery Systems* (eds.Kulkarni, V.S.), William Andrew Publishing, Boston, MA, 59–94.

154. Kittaka, S., and Morimoto, T. (1980) Isoelectric point of metal oxides and binary metal oxides having spinel structure. *J. Colloid Interface Sci.*, **75** (2), 398–403.

155. Kharisov, B.I., Kharissova, O.V., and Ortiz Méndez, U. (2016) *CRC concise encyclopedia of nanotechnology*, Taylor & Francis, CRC Press, Boca Raton, FL.

156. Liu, Y., Liu, H., Zhang, Q., and Li, T. (2017) Adjusting the proportions of {0001} facets and high-index facets of ZnO hexagonal prisms and their photocatalytic activity. *RSC Adv.*, **7** (6), 3515–3520.

157. Ekthammathat, N., Thongtem, T., Phuruangrat, A., and Thongtem, S. (2013) Characterization of ZnO flowers of hexagonal prisms with planar and hexagonal pyramid tips grown on Zn substrates by a hydrothermal process. *Superlattices Microstruct.*, **53**, 195–203.

158. Barreto, G.P., Morales, G., and Quintanilla, M.L.L. (2013) Microwave Assisted Synthesis of ZnO Nanoparticles: Effect of Precursor Reagents, Temperature, Irradiation Time, and Additives on Nano-ZnO Morphology Development. *J. Mater.*, **2013**, 1–11.

159. Crossey, L.J. (1991) Thermal degradation of aqueous oxalate species. *Geochim. Cosmochim. Acta*, **55** (6), 1515–1527.

160. Diodati, S., Pandolfo, L., Caneschi, A., Gialanella, S., and Gross, S. (2014) Green and low temperature synthesis of nanocrystalline transition metal ferrites by simple wet chemistry routes. *Nano Res.*, **7** (7), 1027–1042.

161. Li, W.-J., Shi, E.-W., Zheng, Y.-Q., and Yin, Z.-W. (2001) Hydrothermal preparation of nanometer ZnO powders. *J. Mater. Sci. Lett.*, **20** (15), 1381–1383.

162. Wang, B.G., Shi, E.W., and Zhong, W.Z. (1997) Understanding and Controlling the Morphology of ZnO Crystallites under Hydrothermal Conditions. *Cryst. Res. Technol.*, **32** (5), 659–667.

163. Tsukahara, T., Nagaoka, K., Morikawa, K., Mawatari, K., and Kitamori, T. (2015) Keto–Enol Tautomeric Equilibrium of Acetylacetone Solution Confined in Extended Nanospaces. *J. Phys. Chem. B*, **119** (46), 14750–14755.

164. Jan, H., Shah, M., Usman, H., Khan, M.A., Zia, M., Hano, C., and Abbasi, B.H. (2020) Biogenic Synthesis and Characterization of Antimicrobial and Antiparasitic Zinc Oxide (ZnO) Nanoparticles Using Aqueous Extracts of the Himalayan Columbine (Aquilegia pubiflora). *Front. Mater.*, **7**, 249.

165. Gad El-Rab, S.M.F., Abo-Amer, A.E., and Asiri, A.M. (2020) Biogenic Synthesis of ZnO Nanoparticles and Its Potential Use as Antimicrobial Agent Against Multidrug-Resistant Pathogens. *Curr. Microbiol.*, **77** (8), 1767–1779.

166. Bravard, J.C., Flora, H.B., and Portal, C. (1972) *Energy Expenditures Associated with the Production and Recycle of Metals*, Oak Ridge National Laboratory, Oak Ridge, TN.

167. Yang, S.-T., Liu, J.-H., Wang, J., Yuan, Y., Cao, A., Wang, H., Liu, Y., and Zhao, Y. (2010) Cytotoxicity of Zinc Oxide Nanoparticles: Importance of Microenvironment. *J. Nanosci. Nanotechnol.*, **10** (12), 8638–8645.

168. Rajput, S., Werezuk, R., Lange, R.M., and McDermott, M.T. (2016) Fungal Isolate Optimized for Biogenesis of Silver Nanoparticles with Enhanced Colloidal Stability. *Langmuir*, **32** (34), 8688–8697.

169. Piacenza, E., Presentato, A., and Turner, R.J. (2018) Stability of biogenic metal(loid) nanomaterials related to the colloidal stabilization theory of chemical nanostructures. *Crit. Rev. Biotechnol.*, **38** (8), 1137–1156.

170. Bao, X., Huang, X., Jin, X., and Hu, Q. (2022) Bactericidal Anti-Adhesion Potential Integrated Polyoxazoline/Silver Nanoparticle Composite Multilayer Film with pH Responsiveness. *Polymers*, **14** (17), 3685.

171. Nvkv Prasad, T., Subba Rao Kambala, V., and Naidu, R. (2011) A critical review on biogenic silver nanoparticles and their antimicrobial activity. *Curr. Nanosci.*, **7** (4), 531–544.

172. Niloy, M.S., Hossain, Md.M., Takikawa, M., Shakil, Md.S., Polash, S.A., Mahmud, K.M., Uddin, Md.F., Alam, M., Shubhra, R.D., Shawan, M.M.A.K., Saha, T., Takeoka, S., Hasan, Md.A., and Ranjan Sarker, S. (2020) Synthesis of Biogenic Silver Nanoparticles Using Caesalpinia digyna and Investigation of Their Antimicrobial Activity and In Vivo Biocompatibility. *ACS Appl. Bio Mater.*, **3** (11), 7722–7733.

173. Sintubin, L., De Gusseme, B., Van der Meeren, P., Pycke, B.F.G., Verstraete, W., and Boon, N. (2011) The antibacterial activity of biogenic silver and its mode of action. *Appl. Microbiol. Biotechnol.*, **91** (1), 153–162.

174. Mahmud, K.M., Hossain, Md.M., Polash, S.A., Takikawa, M., Shakil, M.S., Uddin, M.F., Alam, M., Ali Khan Shawan, M.M., Saha, T., Takeoka, S., Hasan, Md.A., and Sarker, S.R. (2022) Investigation of Antimicrobial Activity and Biocompatibility of Biogenic Silver Nanoparticles Synthesized using Syzigyum cymosum Extract. *ACS Omega*, **7** (31), 27216–27229.

175. Gholami, A., Mousavi, S.M., Shomali, A., Hashemi, S.A., Abootalebi, S.N., Chiang, W.-H., Barzegar, A., Shokripoor, M., and Zadeh, A.M. (2022) One-Put Ferula-Mediated Synthesis of Biogenic Silver Nanoparticles with More Antimicrobial Effect and Promising Human Cell Biocompatibility. *J. Nanomater.*, **2022**, 5938952.

176. Chu, D.B.K., Owen, J.S., and Peters, B. (2017) Nucleation and Growth Kinetics from LaMer Burst Data. *J. Phys. Chem. A*, **121** (40), 7511–7517.

177. Vangijzegem, T., Lecomte, V., Ternad, I., Van Leuven, L., Muller, R.N., Stanicki, D., and Laurent, S. (2023) Superparamagnetic Iron Oxide

Nanoparticles (SPION): From Fundamentals to State-of-the-Art Innovative Applications for Cancer Therapy. *Pharmaceutics*, **15** (1), 236.

178. Alcântara Pessôa Filho, P.A., Medeiros Hirata, G.A., Watanabe, É.O., and Miranda, É.A. (2011) Chapter 2.46 - Precipitation and Crystallization, in *Comprehensive Biotechnology (Second Edition)* (eds.Moo-Young, M.), Pergamon, Amsterdam, Netherlands, 651–663.

179. Jana, N.R., Gearheart, L., and Murphy, C.J. (2001) Seeding Growth for Size Control of 5−40 nm Diameter Gold Nanoparticles. *Langmuir*, **17** (22), 6782–6786.

180. Celikbilek Ersundu, M., Ersundu, A.E., and Aydın, Ş. (2012) Chapter 3 - Crystallization Kinetics of Amorphous Materials, in *Advances in Crystallization Processes*, InTech, Istanbul, Turkey, 127–162.

181. de Freitas Rosa, P., Rodrigues Cirqueira, S.S., Lopes Aguiar, M., and Bernardo, A. (2014) Synthesis and Characterization of Silver Nanoparticles. *Mater. Sci. Forum*, **802**, 135–139.

182. Ojea-Jiménez, I., Bastús, N.G., and Puntes, V. (2011) Influence of the Sequence of the Reagents Addition in the Citrate-Mediated Synthesis of Gold Nanoparticles. *J. Phys. Chem. C*, **115** (32), 15752–15757.

183. Babaei afrapoli, Z., Faridi Majidi, R., Negahdari, B., and Tavoosidana, G. (2018) 'Reversed Turkevich' method for tuning the size of Gold nanoparticles: evaluation the effect of concentration and temperature. *Nanomedicine Res. J.*, **3** (4), 190–196.

184. Mughal, B., Zaidi, S.Z., Zhang, X., and Hassan, S.U. (2021) Biogenic Nanoparticles: Synthesis, Characterisation and Applications. *Appl. Sci.*, **11** (6), 2598.

185. Dong, X., Ji, X., Wu, H., Zhao, L., Li, J., and Yang, W. (2009) Shape Control of Silver Nanoparticles by Stepwise Citrate Reduction. *J. Phys. Chem. C*, **113** (16), 6573–6576.

186. Kelly, K.L., Coronado, E., Zhao, L.L., and Schatz, G.C. (2003) The Optical Properties of Metal Nanoparticles: The Influence of Size, Shape, and Dielectric Environment. *J. Phys. Chem. B*, **107** (3), 668–677.

187. Goharshadi, E.K., and Azizi-Toupkanloo, H. (2013) Silver colloid nanoparticles: Ultrasound-assisted synthesis, electrical and rheological properties. *Powder Technol.*, **237**, 97–101.

188. Pandian, S., Kunjiappan, S., Ravishankar, V., and Sundarapandian, V. (2021) Synthesis of quercetin-functionalized silver nanoparticles by rapid one-pot approach. *BioTechnologia*, **102** (1), 75–84.

189. Rérat, C., Papadokonstantakis, S., and Hungerbühler, K. (2012) Estimation and Analysis of Energy Utilities Consumption in Batch Chemical Industry through Thermal Losses Modeling. *Ind. Eng. Chem. Res.*, **51** (31), 10416–10432.

190. Denninger, A., Westedt, U., Rosenberg, J., and Wagner, K. (2020) A Rational Design of a Biphasic Dissolution Setup—Modelling of Biorelevant

Kinetics for a Ritonavir Hot-Melt Extruded Amorphous Solid Dispersion. *Pharmaceutics*, **12** (3), 237.

191. Sirohiwal, A., Berraud-Pache, R., Neese, F., Izsák, R., and Pantazis, D.A. (2020) Accurate Computation of the Absorption Spectrum of Chlorophyll a with Pair Natural Orbital Coupled Cluster Methods. *J. Phys. Chem. B*, **124** (40), 8761–8771.

192. Bitton, R., and Bianco-Peled, H. (2008) Novel Biomimetic Adhesives Based on Algae Glue. *Macromol. Biosci.*, **8** (5), 393–400.

193. Glassner, M., Vergaelen, M., and Hoogenboom, R. (2018) Poly(2-oxazoline)s: A comprehensive overview of polymer structures and their physical properties. *Polym. Int.*, **67** (1), 32–45.

194. Aoi, K., and Okada, M. (1996) Polymerization of oxazolines. *Prog. Polym. Sci.*, **21** (1), 151–208.

195. Grubbs, R.B., and Grubbs, R.H. (2017) 50th Anniversary Perspective: Living Polymerization—Emphasizing the Molecule in Macromolecules. *Macromolecules*, **50** (18), 6979–6997.

196. Boström, J., Brown, D.G., Young, R.J., and Keserü, G.M. (2018) Expanding the medicinal chemistry synthetic toolbox. *Nat. Rev. Drug Discov.*, **17** (10), 709–727.

197. Dalabehera, N.R., Meher, S., Bhusana Palai, B., and Sharma, N.K. (2020) Instability of Amide Bond with Trifluoroacetic Acid (20%): Synthesis, Conformational Analysis, and Mechanistic Insights into Cleavable Amide Bond Comprising β-Troponylhydrazino Acid. *ACS Omega*, **5** (40), 26141–26152.

198. Trachsel, L., Johnbosco, C., Lang, T., Benetti, E.M., and Zenobi-Wong, M. (2019) Double-Network Hydrogels Including Enzymatically Crosslinked Poly-(2-alkyl-2-oxazoline)s for 3D Bioprinting of Cartilage-Engineering Constructs. *Biomacromolecules*, **20** (12), 4502–4511.

199. Pettenuzzo, A., Montagner, D., McArdle, P., and Ronconi, L. (2018) An innovative and efficient route to the synthesis of metal-based glycoconjugates: proof-of-concept and potential applications. *Dalton Trans.*, **47** (31), 10721–10736.

200. Shrivastava, A. (2018) 2 - Polymerization, in *Introduction to Plastics Engineering* (eds.Shrivastava, A.), William Andrew Publishing, Cambridge, MA, 17–48.

201. Rane, S.S., and Choi, P. (2005) Polydispersity Index: How Accurately Does It Measure the Breadth of the Molecular Weight Distribution? *Chem. Mater.*, **17** (4), 926–926.

202. Goto, T., Nitta, R., Nukui, T., Takemoto, M., and Takahashi, T. (2021) Preparation of oxazoline-group-functionalized diamond using poly(2-vinyl-2-oxazoline) based on a model reaction between oxazoline and carboxylic acid. *Diam. Relat. Mater.*, **120**, 108693.

203. Flagel, S.B., Clark, J.J., Robinson, T.E., Mayo, L., Czuj, A., Willuhn, I., Akers, C.A., Clinton, S.M., Phillips, P.E.M., and Akil, H. (2011) A selective role for dopamine in stimulus–reward learning. *Nature*, **469** (7328), 53–57.

204. Patel, S.S., Patel, D.B., and Patel, H.D. (2021) Synthetic Protocols for Aromatic Nitration: A Review. *ChemistrySelect*, **6** (6), 1337–1356.

205. Valeur, E., and Bradley, M. (2009) Amide bond formation: beyond the myth of coupling reagents. *Chem. Soc. Rev.*, **38** (2), 606–631.

206. Jordan, A., Whymark, K.D., Sydenham, J., and Sneddon, H.F. (2021) A solvent-reagent selection guide for Steglich-type esterification of carboxylic acids. *Green Chem.*, **23** (17), 6405–6413.

207. Alice Lee, N., and Kennedy, I.R. (2007) Chapter 5 - Immunoassays, in *Food Toxicants Analysis* (eds.Picó, Y.), Elsevier, Amsterdam, Netherlands, 91–145.

208. Hermanson, G.T. (2013) Chapter 3 - The Reactions of Bioconjugation, in *Bioconjugate Techniques (Third Edition)* (eds.Hermanson, G.T.), Elsevier, Amsterdam, Netherlands, 229–258.

209. Abello, N., Kerstjens, H.A.M., Postma, D.S., and Bischoff, R. (2007) Selective Acylation of Primary Amines in Peptides and Proteins. *J. Proteome Res.*, **6** (12), 4770–4776.

210. Trzciński, J.W., Morillas-Becerril, L., Scarpa, S., Tannorella, M., Muraca, F., Rastrelli, F., Castellani, C., Fedrigo, M., Angelini, A., Tavano, R., Papini, E., and Mancin, F. (2021) Poly(lipoic acid)-Based Nanoparticles as Self-Organized, Biocompatible, and Corona-Free Nanovectors. *Biomacromolecules*, **22** (2), 467–480.

211. El-Faham, A., Funosas, R.S., Prohens, R., and Albericio, F. (2009) COMU: A Safer and More Effective Replacement for Benzotriazole-Based Uronium Coupling Reagents. *Chem. – Eur. J.*, **15** (37), 9404–9416.

212. Manne, S.R., Sharma, A., Sazonovas, A., El-Faham, A., de la Torre, B.G., and Albericio, F. (2022) Understanding OxymaPure as a Peptide Coupling Additive: A Guide to New Oxyma Derivatives. *ACS Omega*, **7** (7), 6007–6023.

213. Marx, D., Wingen, L.M., Schnakenburg, G., Müller, C.E., and Scholz, M.S. (2019) Fast, Efficient, and Versatile Synthesis of 6-amino-5-carboxamidouracils as Precursors for 8-Substituted Xanthines. *Front. Chem.*, **7**, 1–15.

214. Kremsmayr, T., and Muttenthaler, M. (2022) Fmoc Solid Phase Peptide Synthesis of Oxytocin and Analogues, in *Oxytocin : methods and protocols* (eds.Werry, E.L., Reekie, T.A., and Kassiou, M.), Humana Press, New York, NY, 175–199.

215. Zhu, M., and Zhu, L. (2021) Rational Design of Diphenyldiacetylene-Based Fluorescent Materials Enabling a 365-nm Light-Initiated Topochemical Polymerization. *Chem. – Asian J.*, **16** (15), 2048–2054.

216. Socrates, G. (2004) Chapter 11 - Aromatic compounds, in *Infrared and Raman Characteristic Group Frequencies: Tables and Charts*, Wiley, Chichester, UK, 157–167.

217. Socrates, G. (2004) Chapter 9 - Amines, Imines, and Their Hydrohalides, in *Infrared and Raman Characteristic Group Frequencies: Tables and Charts*, Wiley, Chichester, UK, 107–113.

218. Socrates, G. (2004) Chapter 2 - Alkane Group Residues: C-H Group, in *Infrared and Raman Characteristic Group Frequencies: Tables and Charts*, Wiley, Chichester, UK, 50–67.

219. Bragg, W.H., and Bragg, W.L. (1997) The reflection of X-rays by crystals. *Proc. R. Soc. Lond. Ser. Contain. Pap. Math. Phys. Character*, **88** (605), 428–438.

220. Stan, C.V., Beavers, C.M., Kunz, M., and Tamura, N. (2018) X-Ray Diffraction under Extreme Conditions at the Advanced Light Source. *Quantum Beam Sci.*, **2** (1), 4.

221. Mustapha, S., Ndamitso, M.M., Abdulkareem, A.S., Tijani, J.O., Shuaib, D.T., Mohammed, A.K., and Sumaila, A. (2019) Comparative study of crystallite size using Williamson-Hall and Debye-Scherrer plots for ZnO nanoparticles. *Adv. Nat. Sci. Nanosci. Nanotechnol.*, **10** (4), 045013.

222. Schulze, B.M., Watkins, D.L., Zhang, J., Ghiviriga, I., and Castellano, R.K. (2014) Estimating the shape and size of supramolecular assemblies by variable temperature diffusion ordered spectroscopy. *Org. Biomol. Chem.*, **12** (40), 7932–7936.

223. Carvalho, P.M., Felício, M.R., Santos, N.C., Gonçalves, S., and Domingues, M.M. (2018) Application of Light Scattering Techniques to Nanoparticle Characterization and Development. *Front. Chem.*, **6**, 237.

224. Bhattacharjee, S. (2016) DLS and zeta potential – What they are and what they are not? *J. Controlled Release*, **235**, 337–351.

225. Wang, Z.L. (2001) Characterization of Nanophase Materials. *Part. Part. Syst. Charact.*, **18** (3), 142–165.

226. Vernon-Parry, K.D. (2000) Scanning electron microscopy: an introduction. *III-Vs Rev.*, **13** (4), 40–44.

227. Ausili, A., Sánchez, M., and Gómez-Fernández, J. (2015) Attenuated total reflectance infrared spectroscopy: A powerful method for the simultaneous study of structure and spatial orientation of lipids and membrane proteins. *Biomed. Spectrosc. Imaging*, **4**, 159–70.

228. Alshehawy, A.M., Mansour, D.-E.A., Ghali, M., Lehtonen, M., and Darwish, M.M.F. (2021) Photoluminescence Spectroscopy Measurements for Effective Condition Assessment of Transformer Insulating Oil. *Processes*, **9** (5), 732.

229. Wong, K.C. (2014) Review of NMR Spectroscopy: Basic Principles, Concepts and Applications in Chemistry. *J. Chem. Educ.*, **91** (8), 1103–1104.

230. Ho, C., Lam, K.C., Chan, M., Cheung, R., Law, L., Lit, L., Ng, K.F., Suen, M., and Tai, H.L. (2003) Electrospray Ionisation Mass Spectrometry: Principles and Clinical Applications. *Clin. Biochem. Rev. Aust. Assoc. Clin. Biochem.*, **24**, 3–12.